SENSORS AND SYSTEM INTEGRATION FOR MAGNETIC RESONANCE IMAGE (MRI)-GUIDED AND ROBOT-ASSISTED INTERVENTIONS

A Dissertation Presented to

the Faculty of the Department of Computer Science

University of Houston

In Partial Fulfillment

of the Requirements for the Degree

Doctor of Philosophy

By

Junmo An

May 2016

SENSORS AND SYSTEM INTEGRATION

FOR MAGNETIC RESONANCE IMAGE (MRI)-GUIDED

AND ROBOT-ASSISTED INTERVENTIONS

Junmo An

APPROVED:

Dr. Nikolaos V. Tsekos, Chairman
Dept. of Computer Science, University of Houston

Dr. Ernst Leiss
Dept. of Computer Science, University of Houston

Dr. Weidong Shi
Dept. of Computer Science, University of Houston

Dr. Dipan J. Shah
Weill Cornell Medical College, Hospital Methodist

Dr. R. Jason Stafford
Dept. of Imaging Physics, UT MDA Cancer Center

Dean, College of Natural Sciences and Mathematics

DEDICATION

To my wife, Mina, and my family

ACKNOWLEDGMENTS

The completion of this dissertation would not have been possible without the encouragement and support of many people as I have had during my years earning a Ph.D.

First of all, I would like to thank my advisor, Dr. Nikolaos V. Tsekos, for his great feedback and support throughout my research. He was always supportive and provided me with the countless hours of mentorship and the freedom to fully explore the research concepts and ideas during my PhD program.

I would also like to express my gratitude to my committee members, Dr. Ernst Leiss, Dr. Weidong Shi, Dr. Dipan J. Shah, and Dr. R. Jason Stafford. They offered good comments to enhance my dissertation.

I thank my present and past colleagues in the Medical Robotics Laboratory: Dr. Erol Yeniaras, Dr. Ahmet E. Sonmez, Dr. Nikhil V. Navkar, Dr. Nicholas C. von Sternberg, Mr. Daniele Farris, Mr. Habib Zaid, Mr. Mahmut Unan, Mr. Xin Liu, Ms. Pradheebaa Srinivas, Ms. Giulia Toti, and Mr. Mario Rincon Nigro. We had a good time together.

I would like to extend particular thanks to Dr. Andrew G. Webb, Dr. Eftychios G. Christoforou, Dr. Ioannis Seimenis, Ms. Karen Chin, Mr. Kyle Autry, Mr. Jeremy Hinojosa, Mr. Rahul Korpu, Mr. Daniel Biediger, and Dr. Tayfun Tuna. Especially, I thank Mr. Daniel Lee for your devoted assistance.

I owed a great debt to Dr. Moon Hae Kim who was a professor at Konkuk University and passed away unexpectedly in 2006.

Lastly, I wholeheartedly thank my wife for her love and sacrifice.

SENSORS AND SYSTEM INTEGRATION FOR MAGNETIC RESONANCE IMAGE (MRI)-GUIDED AND ROBOT-ASSISTED INTERVENTIONS

An Abstract of a Dissertation

Presented to

the Faculty of the Department of Computer Science

University of Houston

In Partial Fulfillment

of the Requirements for the Degree

Doctor of Philosophy

By

Junmo An

May 2016

ABSTRACT

Demand for magnetic resonance image (MRI)-guided interventions and robot-assisted surgeries continues to increase in the field of medical robotics. MRI-guided interventions provide pre-/intra-operative MR images and intraoperative manipulations. Robot-assisted surgeries guarantee higher safety and greater dexterity inside the patient's body. Integration of MRI-guided and robot-assisted intervention techniques bring better precision, increased dexterity, and improved 3D visualization for surgery planning and real-time MR guidance. Despite the significant benefits of these techniques, potential challenges still remain: (i) for localization and tracking of MR-compatible manipulators using MR-visible markers, (ii) for 3D visualization of catheters and blood vessels in planning and guidance of interventional devices, (iii) for complementary characterization of human tissues and organs using multimodality imaging approaches, (iv) for higher flexibility and accessibility to overcome lack of navigation and limited workspace inside the human body and the MRI scanner.

This dissertation describes the development of several enabling technologies for the MRI-guided and robot-assisted interventions. The specific technologies encompassed are: (i) an inductively coupled radio frequency (ICRF) coils that are optically tuned and detuned by the control of an MR-compatible manipulator for accurate localization and fast tracking, (ii) a novel method for 3D reconstruction of tubular structures such as catheters and blood vessels from three orthogonal MR projection images, (iii) an MR-compatible

optical encoder for position feedback of the MR-compatible manipulators, (iv) a manipulator-mounted magnetic resonance spectroscopy (MRS) / light induced fluorescence (LIF) probe for multimodality bioimaging and biosensing applications, (v) an MR-compatible dexterous robotic manipulator for providing higher flexibility and accessibility, (vi) and the integration of the above mentioned techniques for the MRI-guided and robot-assisted interventions.

Contents

List of Figures

List of Tables

Chapter 1

1 Introduction

1.1 Overview

This dissertation tries to study the motivation and related works in the fields of minimally invasive surgery (MIS), magnetic resonance image (MRI), MRI-guided interventions and robot-assisted surgeries in Chapter 1.2. Challenges of MRI compatibility, tracking of MR-compatible manipulators, and patient accessibility for the limited workspace inside MR scanner are described in Chapter 1.3. Finally, Chapter 1.4 presents a discussion on the contributions of this author.

Chapter 2 demonstrates our technique for localization and tracking of MR-compatible manipulator using optically detunable MR visible markers.

Chapter 3 describes the triplanar MR projection imaging (TPI) scheme for 3D reconstruction of contrast enhanced tubular object with simultaneous acquisition of the TPI set and 3D reconstruction of its tubular structure from the TPI set.

Chapter 4 demonstrates the development of MR-compatible sensors i.e., MR-compatible optical encoder, magnetic resonance spectroscopy (MRS) / light induced fluorescence (LIF) dual-modality biosensor, MR-compatible dexterous manipulator robot and system integration.

Chapter 5 concludes and summarizes the highlights of this dissertation, and describes our future perspective.

1.2 Motivation

More recently, technical advances in the field of medical robotics have led to the development of image-guided and robotic surgical systems for diagnostic and therapeutic interventional procedures. Rapid evolution of robot-assisted surgeries provides substantial benefits by greatly enhancing a surgeon's technical capability and by overcoming the risks associated with surgery thereby improving the patient's safety. The technological advance of real-time MR images for MRI-guided surgery enables preoperative planning, intraoperative guidance, and postoperative outcome evaluation of surgical patients to surgeons.

1.2.1 Minimally Invasive Surgery (MIS)

Minimally invasive surgery (MIS), also known as minimal access surgery or keyhole surgery, has rapidly emerged as a complex surgical procedure for the treatment of patients and is being extensively used in a variety of surgeries. MIS is a practical technique in surgery which inserts small surgical tools into the patient body through small incisions and orifices to access the area of surgery efficiently. During MIS, it not only gives excellent surgical outcomes to the patients, it also reduces recovery time, intraoperative blood loss, perioperative anxiety, postoperative pain/trauma, risk of infection, and other postoperative complications when compared to traditional open surgery [1].

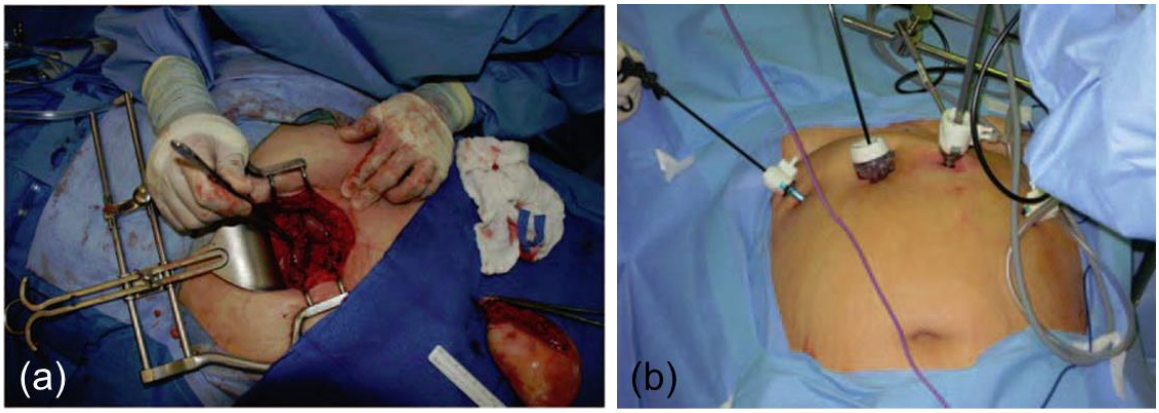

Figure 1.1 (a) Traditional open surgery and (b) minimally invasive surgery [2].

However, MIS requires technically demanding challenges of compactness, visibility, and dexterity [3]. So, the surgeon may also need minimally invasive surgical (MIS) tools, a small endoscopic camera and video monitors to display the internal organs and tissues during the MIS. Many different kinds of MIS tools are being created and used

for particular surgeries including: laparoscopic cholecystectomy, fundoplication, groin hernia, ventral hernia, splenectomy, adrenalectomy, nephrectomy, gastrotomy, cystotomy, appendectomy, hyperaldosteronism, a variety of gynecologic laparoscopies and so on [4-10]. In addition, intraoperative image-guided surgeries and interventions by ultrasound [11], fluorescence [12], X-ray [13], computed tomography (CT) [14], magnetic resonance imaging (MRI) [15, 16], positron emission tomography (PET) [17] or other medical imaging modalities [13] have been employed for MIS procedures. Robotic surgical systems, referred to as robotic surgery or robot-assisted surgery, may be employed to deal with the weaknesses in the MIS (i.e., higher robustness, precision, safety, etc.).

1.2.2 Magnetic Resonance Imaging (MRI)

Magnetic resonance imaging (MRI) is an emerging medical imaging modality producing high quality images of organs and tissues inside the human body. MRI provides excellent visualization of soft-tissue contrast mechanisms using optimized pulse sequences. MRI scanner uses an electromagnet with a high strength magnetic field (clinically performed at 1.5 to 7.0 Tesla), rapidly varying magnetic field gradients and radiofrequency waves to create high-quality and high-resolution medical images of the human body. An electromagnetic field generated by a superconducting electromagnet is used to determine the magnetic moment of atomic nuclei aligned parallel to the main magnetic field (B_0) of the scanner. Varying magnetic field gradients are used for spatial encoding during MR imaging procedures. The radiofrequency waves are employed to excite the atomic nuclei

within the human body and to collect re-emitted radiofrequency waves which include nuclear magnetic resonance (NMR) properties depending on biophysical characteristic of human tissues. Compared to other imaging modalities such as X-ray, computed tomography (CT), fluoroscopy, and positron emission tomography (PET) imaging, MRI can avoid exposure to harmful ionizing radiation. MRI enables not only multislice and multiplanar imaging but also provides on-the-fly adjustment through its MRI scanning software controls to the radiologist to allow arbitrary planes of view (i.e., oblique planes).

1.2.3 MRI-guided Interventions

MRI is a medical imaging modality for diagnostic interventional procedures because it provides non-invasive imaging, non-ionizing radiation, superior soft-tissue contrast and multislice/multiplanar/oblique imaging options. Due to these MRI advantages, MRI-guided interventions are rapidly evolving in the field of MIS based on real-time MR images. MRI-guided intervention, by use of continuous real-time MR images, promises image guided surgical procedures for diagnosis and treatment and enables use of appropriately designed guidewires, catheters, and interventional tools for medical or surgical handling of patients. MRI-guided interventions brings high resolution MR images of the human body, organs, and tissues to the physician or surgeon during intraoperative manipulations without the risk of ionizing radiation that often comes with other image-guided interventions. Some MRI-guided interventions were developed for percutaneous biopsy [18, 19], liver cryosurgery [20], interstitial brachytherapy [21], liver tumor ablations

[22], musculoskeletal tumor cryotherapy [23], breast lumpectomy [24], abdominal tumor ablations [25], renal cell carcinoma cryotherapy [26], cardiac surgery [27], gene therapy [28], endovascular procedure [29], and breast biopsy [30, 31].

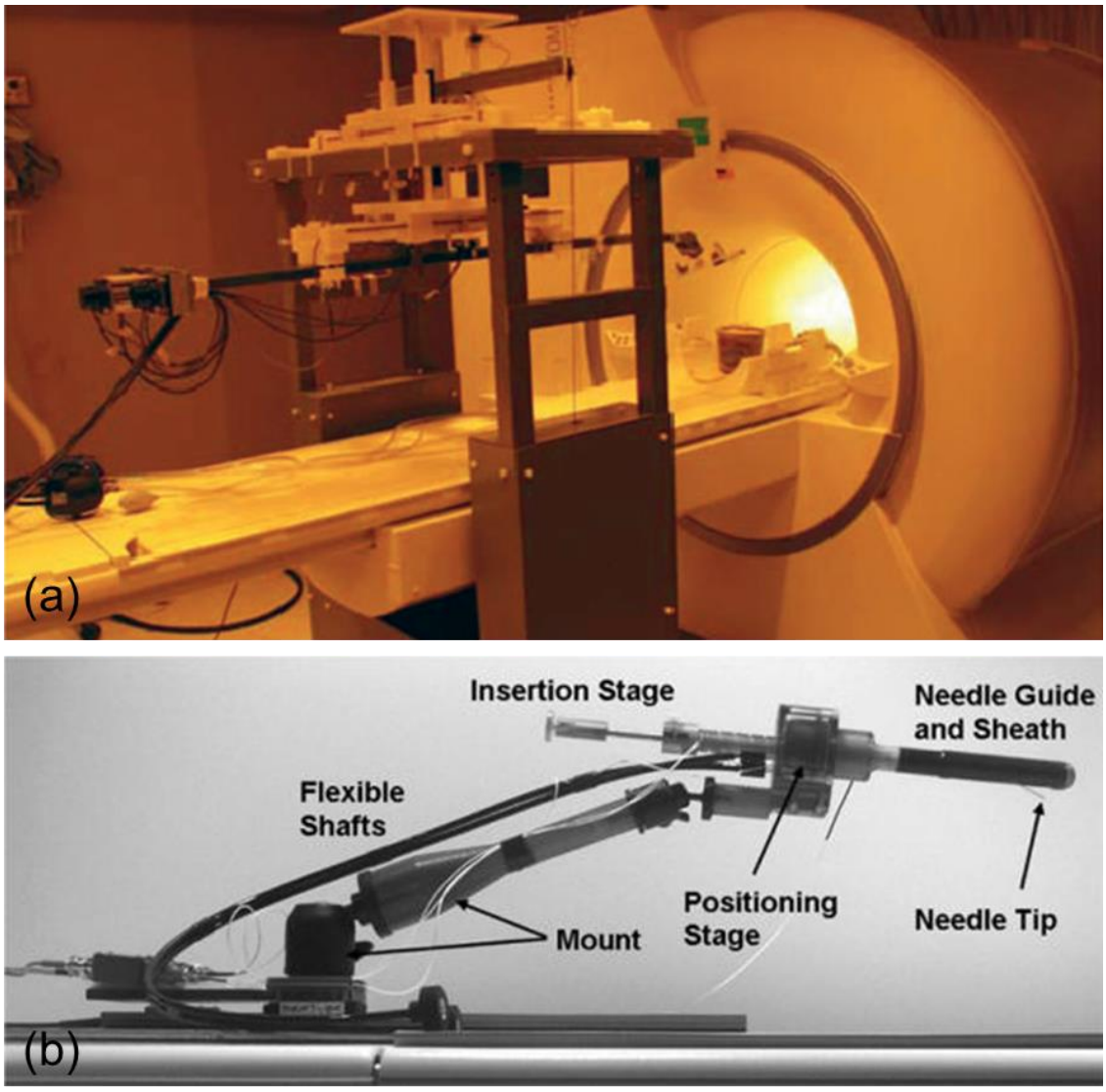

Figure 1.2 The MR-compatible manipulators for MRI-guided procedures (a) in the general-purpose biopsy [32], and (b) in the prostate [33].

1.2.4 Robot-Assisted Surgeries

Robot-assisted surgeries, also known as robotic surgeries, have been adapted to assist in MIS procedures via robotic surgical systems. The advantages offered by robot-assisted surgeries not only give higher precision tolerance and robustness for surgical safety but also provide tirelessness and stability for consistency that in turn reduces rate of unintentional injuries to patient's tissues and organs. Furthermore, robotic surgeries enhance technical and surgical capabilities for surgeons by enabling responsiveness, dexterity and accessibility for use in surgeries [3].

Some commercial robotic surgical systems and several noncommercial systems have been developed to assist surgeons with excellent accuracy and dexterity in the limited workspace that comes with doing procedures inside the human body. The PUMA 560 robotic surgical arm [34] was first employed to perform CT-guided neurosurgical and non-laparoscopic biopsies. The da Vinci telesurgical robot (Intuitive Surgical, Sunnyvale, USA) [35] is the most widely used commercial product for performing hand-assisted laparoscopic surgeries and cardiac interventions at present. Other robotic surgical systems such as AESOP (Computer Motion Inc., Goleta, CA, USA) [36, 37], ZEUS (Computer Motion Inc., Goleta, CA, USA) [38, 39], ROBODOC (Curexo Technology Corp., Fremont, CA, USA) [40], SOCRATES (Computer Motion Inc., Goleta, CA, USA) [41], PAKY (Urobotics Laboratory, JHMI, Baltimore, MD, USA) [42], CASPAR (Orto Maquet GmbH and Co., Rastatt, Germany) [43], and ACROBOT (Acrobot Company Ltd., London, UK) [44] were developed for various types of robot-assisted surgeries.

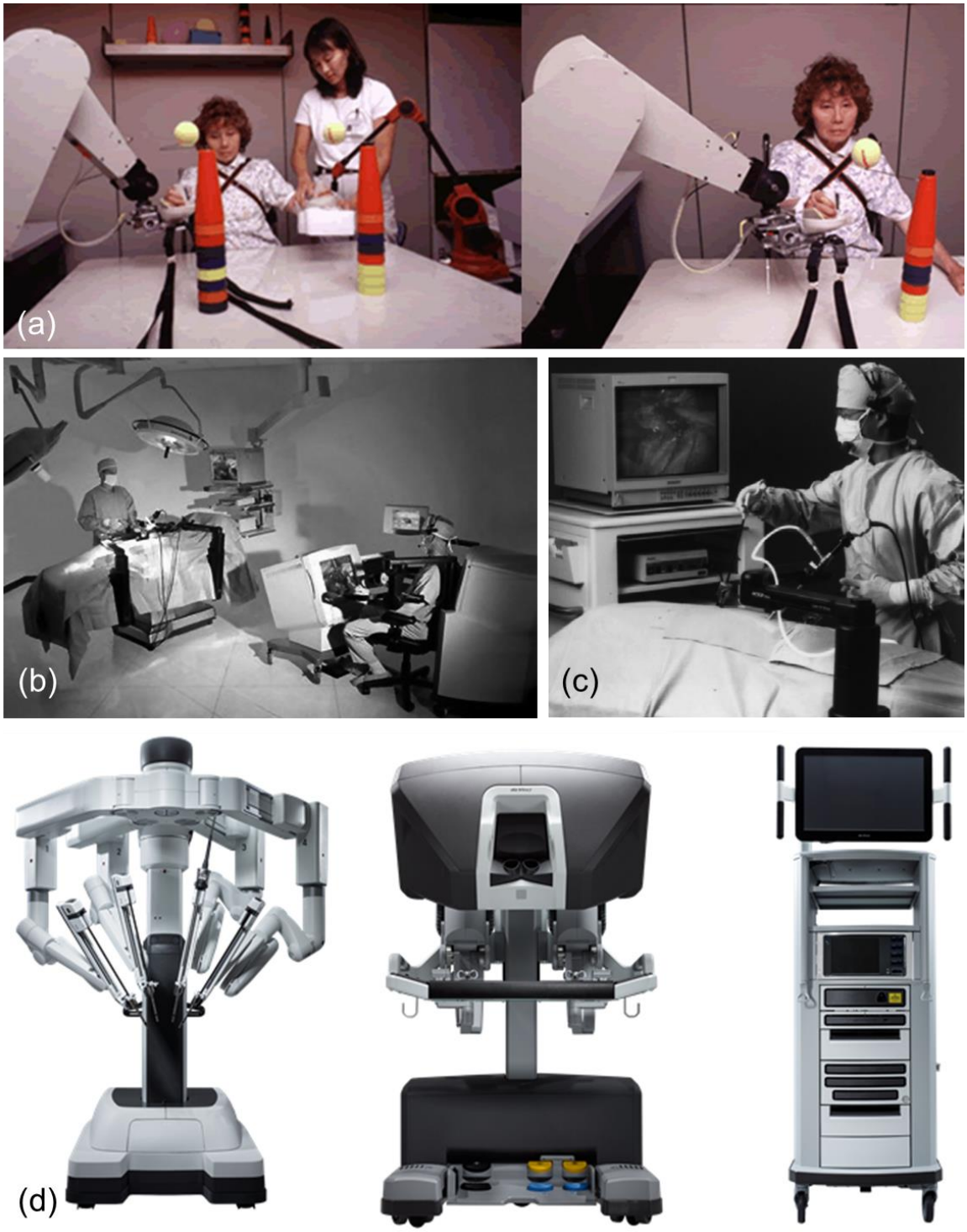

Figure 1.3 Robotic surgical systems: (a) PUMA 560 robotic arm [45], (b) Zeus surgical telemanipulator system [39], (c) AESOP ® system [37], and (d) da Vinci ® surgical system (Copyright © 2016 Intuitive Surgical, Inc.).

1.3 Challenges

MRI is an ideal diagnostic imaging modality for MRI-guided interventions and robot-assisted surgeries with high quality (resolution), real-time, multiplanar, multislice, and 3D volumetric images. However, some significant challenges still remain: MRI compatibility, localization / tracking of MR-compatible surgical robots, and limited patient accessibility inside the MR scanner bore of the MRI scanner. These major challenges for MRI-guided interventions and robot-assisted surgeries are primarily described in this section.

1.3.1 MRI Compatibility

MRI compatibility is a critical factor for MRI-guided stereotactic surgeries and robot-assisted interventions. Although MRI uses non-ionizing radiation during MR imaging of patient, significant issues of MR safety, MR conditions, and image distortion still remain. The common terms of “MR safe”, “MR conditional”, and “MR unsafe” are defined in the American Society for Testing and Materials (ASTM) Standard F2053 - 13 [46]. According to the ASTM Standard, MR safe is defined as the elimination of the hazardous risks to the patient resulting from exposure of ionizing radiation. MR conditional specifies that an object as safe to use in the MR environment with the conditions of the high strength magnetic, gradient magnetic, and radiofrequency fields. MR conditions of

high-strength magnetic fields, gradient magnetic fields, and radiofrequency waves are of significant concern for MR safety, and avoidance of signal noise and artifacts on the MR image. MR unsafe is used to describe objects that affect undesirable hazard risks to the patients and radiologists in and around the MRI scanner.

The instruments for MRI-based surgeries such as surgical robots, needles, catheters, interventional tools, laryngoscope or endoscopes are typically constructed of metallic materials that create distortions and signal voids in MR images. In order to preserve MR safety within the MR environment, these interventional and surgical devices should be made of electrically nonconductive (as MR environment requires), nonferrous, nonmagnetic, and MR-compatible (as commonly called) materials such as copper, aluminum, stainless steel, titanium, wood, glass, plastic, ceramics, phynox, vitallium, nickel alloys, MP35N alloy, and so on [47-49].

MRI artifacts and distortion may affect the diagnostic image quality of human tissues and organs. Radiofrequency waves employed to excite the atomic nuclei and to collect re-emitted MR signal are very sensitive to the undesired noise called electromagnetic interference (EMI) generated when peripheral electronic devices are in the vicinity of the MRI scanner. Eddy currents [50-55] induced conductive materials may decrease the efficiency of varying magnetic field gradients, disrupt the magnetic field homogeneity, and lead to a variety of different image artifacts such as spatial misregistration, blurring, zipper, zebra stripes, central point, RF overflow, inhomogeneity, shading, moire fringes, etc. Eddy currents may also induce physiological side effects to patient associated with peripheral nerve stimulation or unwanted hazardous heating of tissues within the rapidly changing magnetic field of the MRI scanner.

1.3.2 Tracking of MR-Compatible Manipulators

Accurate localization and fast tracking of MR-compatible interventional tools such as catheters, have become an indispensable factor in MRI-guided and robot-assisted interventions [56]. Multiple MR-visible markers, also known as fiducial markers, are required to measure geometric position and orientation of the MR-compatible tools or the interventional tools within the MR image. For example, single MR-visible marker can be used for single-point motion tracking of the end portion of the interventional device. The use of two markers can measure the position and orientation of a portion of the MR-compatible manipulator and a straight interventional devices such as ablation probes or biopsy needles. By using large numbers of markers, tracking can be done on more articulated manipulators such as snake-like robotic devices or a large portion of an interventional tool such as a bendable catheter; however, the speed of post-image processing time will be slower for marker detection, and position and orientation calculations. There is the correlation between numbers of markers and post-image processing time. Numbers of markers are directly proportional to post-image processing time. Accordingly, during MRI-guided interventions, the suitable number of markers and the correct position of the marker on their articulated manipulators must be determined to provide adequate monitoring and tracking of markers [56-59].

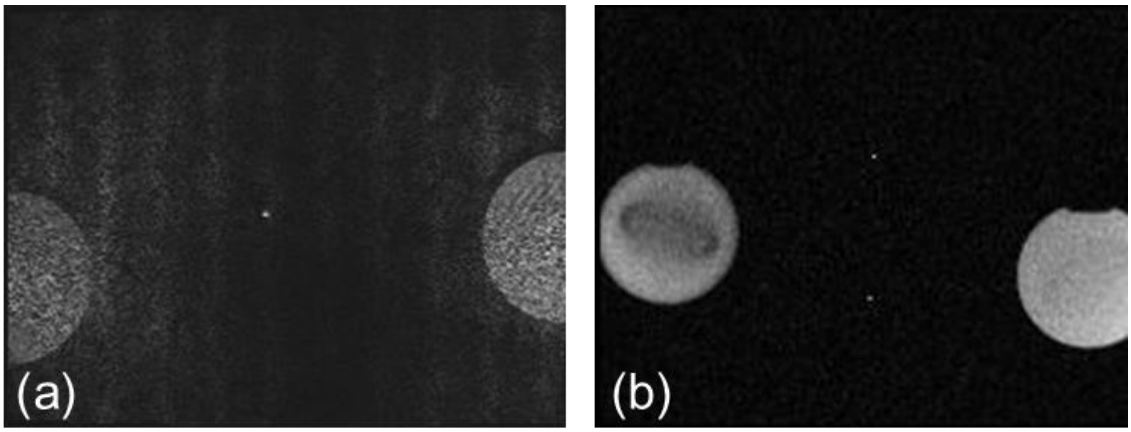

Figure 1.4 (a) Single marker is visible for tracking of the end portion of the manipulator and (b) two markers are used for tracking of a straight biopsy needle [59].

1.3.3 Patient Accessibility

Against the significant benefits of MR imaging, patient accessibility is considerably limited inside the MR scanner bore for MRI-guided interventions [60, 61]. The magnet bore diameter of most closed-bore MRI scanners (i.e., standard-bore, wide-bore, and oval-bore) commonly performed at 1.5 T or 3.0 T typically ranges from 55 cm (24 inches) to 74 cm (29 inches). Compared to the traditional closed-bore MRI, open bore MRI scanners provide more space for patient accessibility. The open MRI scanner typically uses two flat magnets and the vertical length between these magnets ranges from 40 cm to 45 cm; however, the horizontal length is in the range of 120 cm to 200 cm. Although the open-type MRI scanner has better patient accessibility and can comparatively alleviate claustrophobia, the open MRI uses a lower-field strength producing relatively lower image clarity than the closed-bore MRI.

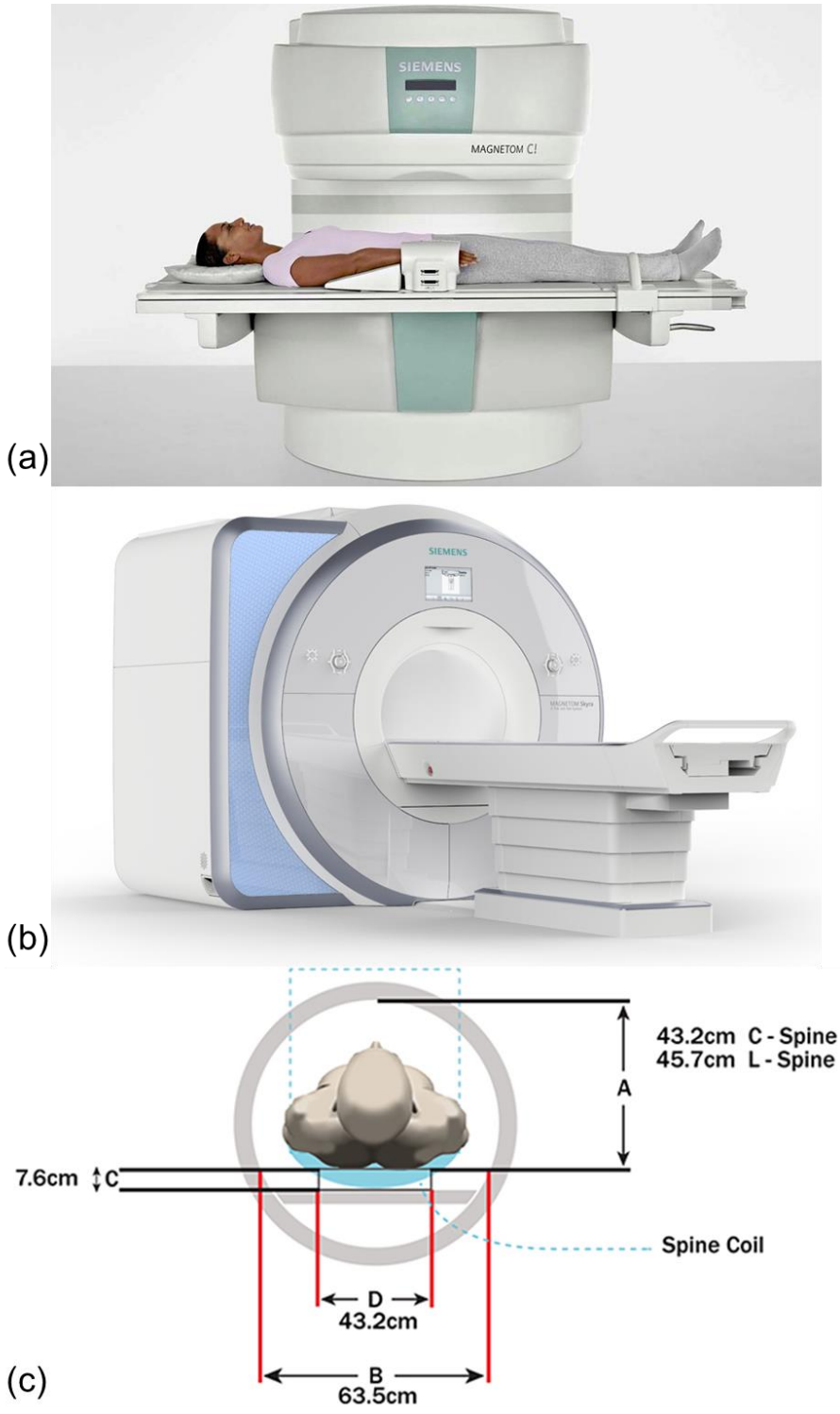

Figure 1.5 Photograph of the (a) open MRI scanner and (b) the closed-bore 3T MRI scanner. (Copyright © 2016 Siemens Medical Solutions USA, Inc.) (c) Illustration of workspace constraints of the closed-bore (Copyright © 2016 Toshiba Corporation).

1.4 Contributions

The purpose of this dissertation is to introduce methodologies of the concomitant technologies for sensors and system integration for the MRI-guided surgeries and robot-assisted interventions. The essential contributions of this dissertation are as follows:

- We have thoroughly developed a technique for fast tracking and accurate localization of the MR-compatible manipulators using optically detunable MR-visible markers that are selectively tuned or detuned determined by the maneuvering portion of an MR-compatible manipulator. We have designed the process flow and algorithms for manipulator-driven marker selection and tracking of the MR-compatible manipulators.
- We have simultaneously studied a multiple MR projection imaging method and fully developed a novel method for segmentation and 3D reconstruction of targeted contrast enhanced tubular structures, such as blood vessels, catheters and interventional tools, from three orthogonal MR projection images.
- We have developed the fully MR-compatible optical encoder for feedback control of general-purpose MR-compatible manipulators. We have studied robot-assisted dual-modality probe that is magnetic resonance spectroscopy (MRS) and light induced fluorescence (LIF). We have also developed an MR-compatible dexterous robotic system to overcome patient accessibility inside the MR scanner bore and space constraints inside the human body. Furthermore, we have designed the system integration of optically detunable MR-visible markers, a dual-modality

probe and an MR-compatible dexterous robotic manipulator for the MRI-guided surgeries and robot-assisted interventions.

Chapter 2

2 Localization and Tracking of MR-Compatible Manipulators

An introduction in the field of MR-visible markers for MRI-guided and robot-assisted interventions have been described in Chapter 2.1. Design of computer-controlled optically detunable markers, manipulator-driven marker selection and tracking methods, and MRI studies have been described in Chapter 2.2. Experimental results have been demonstrated in Chapter 2.3. A discussion of the technique is described in Chapter 2.4.

Chapter 2 is reproduced based primarily upon "Tracking of MRI Interventional Devices with Computer-Controlled Detunable Markers", DOI: 10.1007/978-3-319-32703-7_127 [59], "Localization and tracking with RF coils that are optically detuned by the control of an MR compatible manipulator" [57], "Tracking of a Robotic Device by Controlling the Visibility of Markers from the Robot Control" [58], and "Tracking of MR compatible interventional robots by controlling the MRI visibility of optically detunable MR markers", DOI: 10.1016/j.ejmp.2014.07.155 [56] performed in collaboration with Xin Liu, Mahmut Unan, Eftychios G. Christoforou, Karen Chin, Jeremy Hinojosa, Dipan J. Shah, Andrew G. Webb, and Nikolaos V. Tsekos. Copyright Physica Medica: European Journal of Medical Physics (2014), ISMRM (2014 and 2016) and MEDICON (2016).

2.1 Introduction

Using MR-visible markers is very critical for localization and tracking of MR-compatible manipulator in interventional procedures with real-time MR guidance [62-66]. To identify the markers on MR image, an optical detuning method [67, 68] by the integration of the photoresistors or the PIN photodiodes via optical fiber cables has been proposed to make one marker or all markers together observable per data acquisition cycle. In order to track, visualize and localize the MR-compatible manipulators or interventional tools, several types of tracking markers for contrast enhancement have been proposed previously. They are typically classified as passive, active and semiactive approaches. The purpose of this study is to develop a technique that multiple optically detunable MR-visible markers can be selectively tuned and detuned by the motion of the maneuvering portion of the manipulator. In other words, only one or several markers can be individually active per MR data acquisition to unambiguously identify the markers for tracking manipulator maneuvering. This technique can increase the speed of MR data acquisition and marker identification on MR images.

2.1.1 Passive Approach

Passive method [69-71] commonly employs MR contrast agents like gadolinium (Gd)-based compounds (positive) which shorten the relaxation time of atoms and increase

the MR signal for contrast enhancement on MR images. Paramagnetic contrast agents which induce significant MR signal voids (negative) are also used for the visualization of internal body structures or interventional tools on MR images. The passive method does not create any RF-induced heating and safety hazards to the patient because these have no electrical and conductive components; however, they frequently provide poor contrast between markers and background on MR images.

2.1.2 Active Approach

Active method [72-75], on the other hand, uses locally sensitive resonant coils connected to channels of the scanner for localization and tracking, and these coils collect the high MR signal from their immediate surroundings. In addition, active method provides higher signal-to-noise ratio (SNR) images of the surrounding tissues than passive ones. However, active method is potentially prone to the risk of dangerous tissue heating caused by the RF energy generated from the MRI scanner because of elongated conductors and the use of electrical/conductive wires. In order to completely eliminate the necessity of a physical connection between the catheter and the MRI scanner, the technique of wireless active stents and catheter visualization was proposed [76].

2.1.3 Semiactive Approach

An alternative method is to employ inductively coupled RF (ICRF) coils, commonly called semiactive method [77-79]. Unlike active method, semiactive method does not require connecting conductive wires to a separate receiver channel of the MRI scanner, which makes their application relatively safe from the risk of potential RF induction heating during RF excitation. In addition, semiactive method can provide much higher signal intensity than passive method; this is why it is easier to detect than passive ones on MR images. Optical detuning techniques using a photoresistor and a PIN photodiode via an optical fiber were proposed for tracking of interventional tools [67, 68].

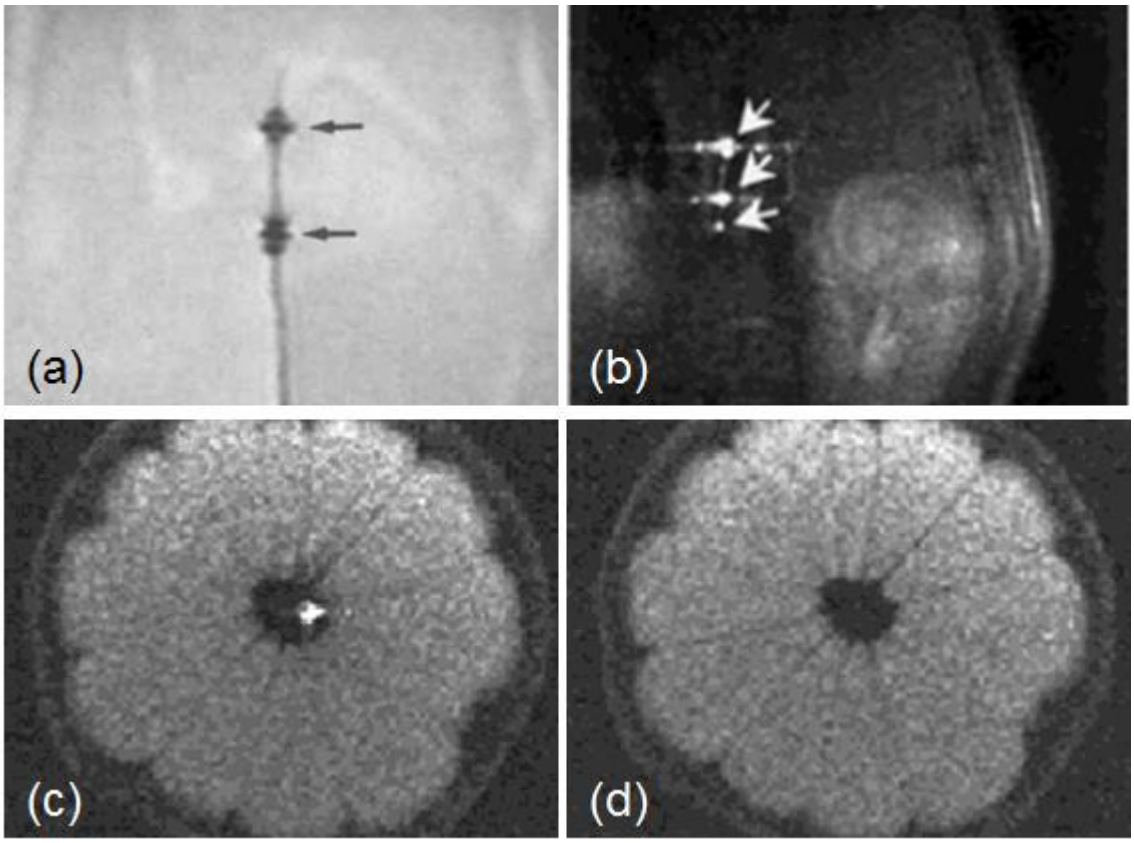

Figure 2.1 Marker appearance on MR image: (a) passive [71], (b) active [75], and optical detuning method (c) and (d) [67].

2.2 Method

2.2.1 Design of Computer-Controlled Optically Detunable Markers

Figure 2.2 illustrates the (a) schematic and (b) photograph of an optically detunable MR-visible marker that can be selectively conspicuous and inconspicuous on the MR image by the control of a MR-compatible robot maneuvering. The marker is based on the parallel RLC resonant circuit. The marker composes of an inductor, represented by the letter 'L', a capacitor, represented by the letter 'C', and a photoresistor, represented by the letter 'R'. An inductor, capacitor and photoresistor are placed in parallel. An inductor is a small sized solenoid coil with seven turns of 26 American Wire Gauge (AWG) (i.e., 0.4049 mm) copper magnet wire (Belden Inc., Richmond, IN) wound around a biocompatible concentric tube (2.0 mm inner diameter (ID) and 3.0 mm outer diameter (OD)) and the tube was filled with hydrogel type internal signal source (MM3005, IZI Medical Products, Baltimore, MD) observed as the passive MR signal; in addition, both holes on the tube were terminated by the biocompatible glue to avoid the disappearance of the MR signal source. The hydrogel type of MR signal source is more sustainable than a Gadolinium (Gd) based contrast agent, and more straightforward to fill it in the tube than solid and liquid type materials. A variable non-magnetic capacitor (8PF - 50PF, Johanson Manufacturing Co., Boonton, NJ) is used to determine the resonant frequency of the RLC resonant circuit

and is connected as close to an inductor for a higher Q factor in parallel. A photoresistor (GL3547-1, Nanyang Senba Optical Electronic Co., Shen Zhen, China), a light-controlled variable resistor, is connected to a solenoid coil and a variable capacitor in parallel and is used to make the marker optically tuned and detuned. In order for optically detuning, the MR-visible marker is connected to the ultrahigh brightness LED (75 0404, white light, 90 mW, Industrial Fiber Optics Inc., Tempe, AZ) controlled by the marker control circuit (i.e., the LED controller) via 15 meter long optical fiber cable (Eska GH4001, Mitsubishi Rayon Co., Japan). The lens cap (51 0450, Industrial Fiber Optics Inc., Tempe, AZ) is placed on the top surface of the photoresistor, and it is used both for allowing reliable mechanical attachment to the optical fiber and for providing higher light visibility. The lens cap and the photoresistor are placed as close as possible to each other, which is used for optically detuning the RLC resonant circuit, are wrapped by a light protective plastic-wrap to avoid the fluctuation of the amount of light by the unwanted light. The RLC resonant circuit, i.e., optically detunable MR-visible marker, can be tuned to both the Larmor frequency (63.7 MHz) of our 1.5 T MR scanner and the frequency (127.71 MHz) of 3.0 T scanner without rebuilding the resonant circuit by manually regulating capacitance of a variable capacitor.

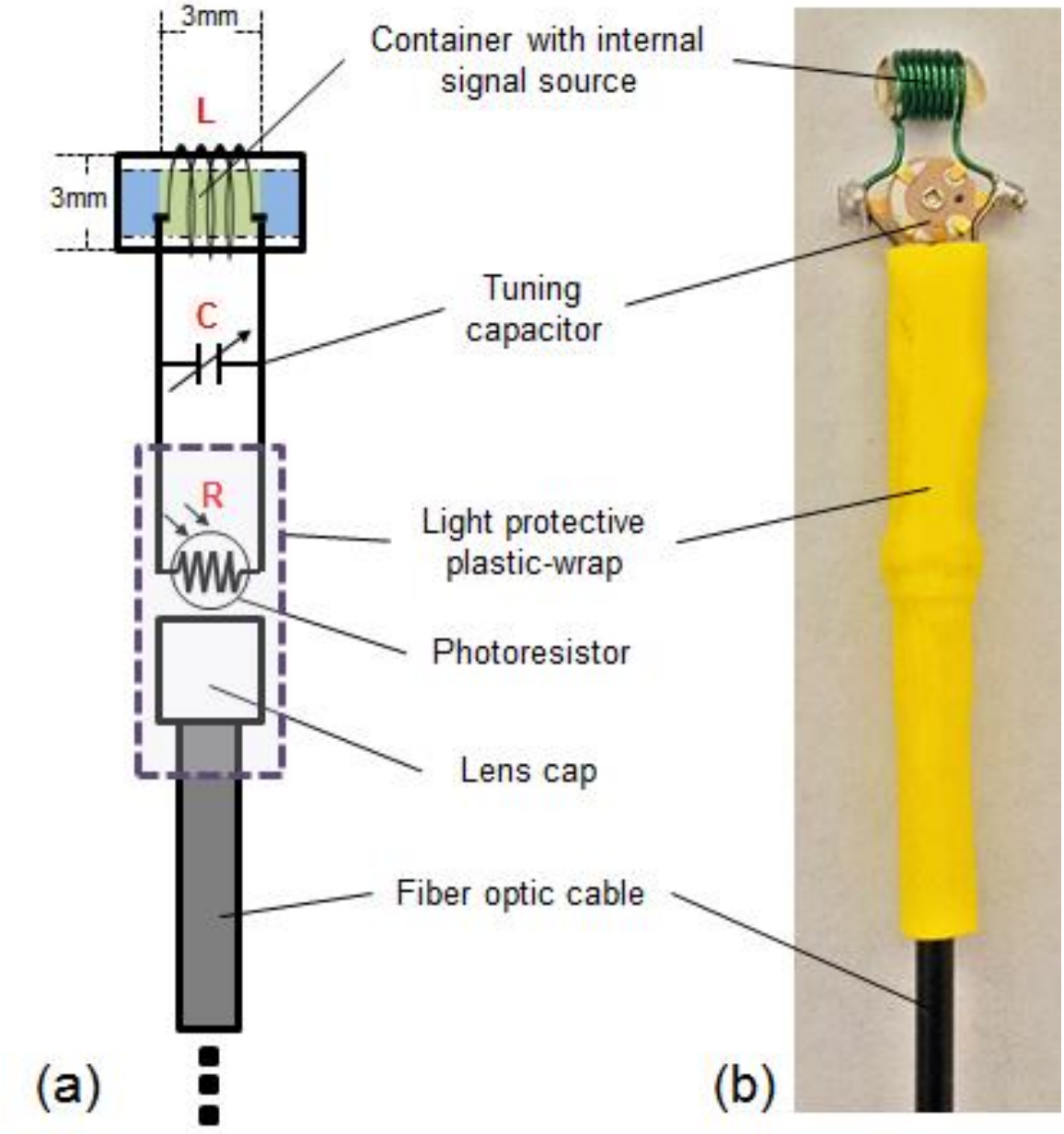

Figure 2.2 (a) Schematic of optically detunable MR-visible marker consisting of an inductor, a capacitor, and a photoresistor, (b) photograph of its marker.

2.2.2 Manipulator-Driven Marker Selection and Tracking

Figure 2.3 shows (a) photograph of the marker control circuit and (b) diagram of process flow that is the integrated control system of the manipulator and marker control. The marker control circuit made of the microcontroller (Arduino UNO, www.arduino.cc) generates a TTL (transistor-transistor logic) pulse which communicates with the MR scanner and turns ON or OFF the LEDs which provide high brightness for optically tuning or detuning the MR-visible marker. Accordingly, the marker control circuit sends a TTL pulse directly to the MR scanner to collect the MR images and receives a return TTL pulse to trigger turning on or off the next marker after finishing the MR image acquisition. For manually detuning of a resonant circuit, pushbutton switches are employed to turn the LEDs ON and OFF. The integrated control system of the manipulator and marker control modules is located outside the MR scanner room. In addition, the MR-compatible manipulator attached to four MR-visible markers are placed inside the scanner room, and optical fiber cables pass through a penetration panel that contains RF shielded waveguides on the wall of the scanner room. The integrated control system of the manipulator and marker control modules controls the MR-compatible manipulator, communicates with the MR scanner, and determines for tracking a combination of markers that correspond to the maneuvering portion of the manipulator.

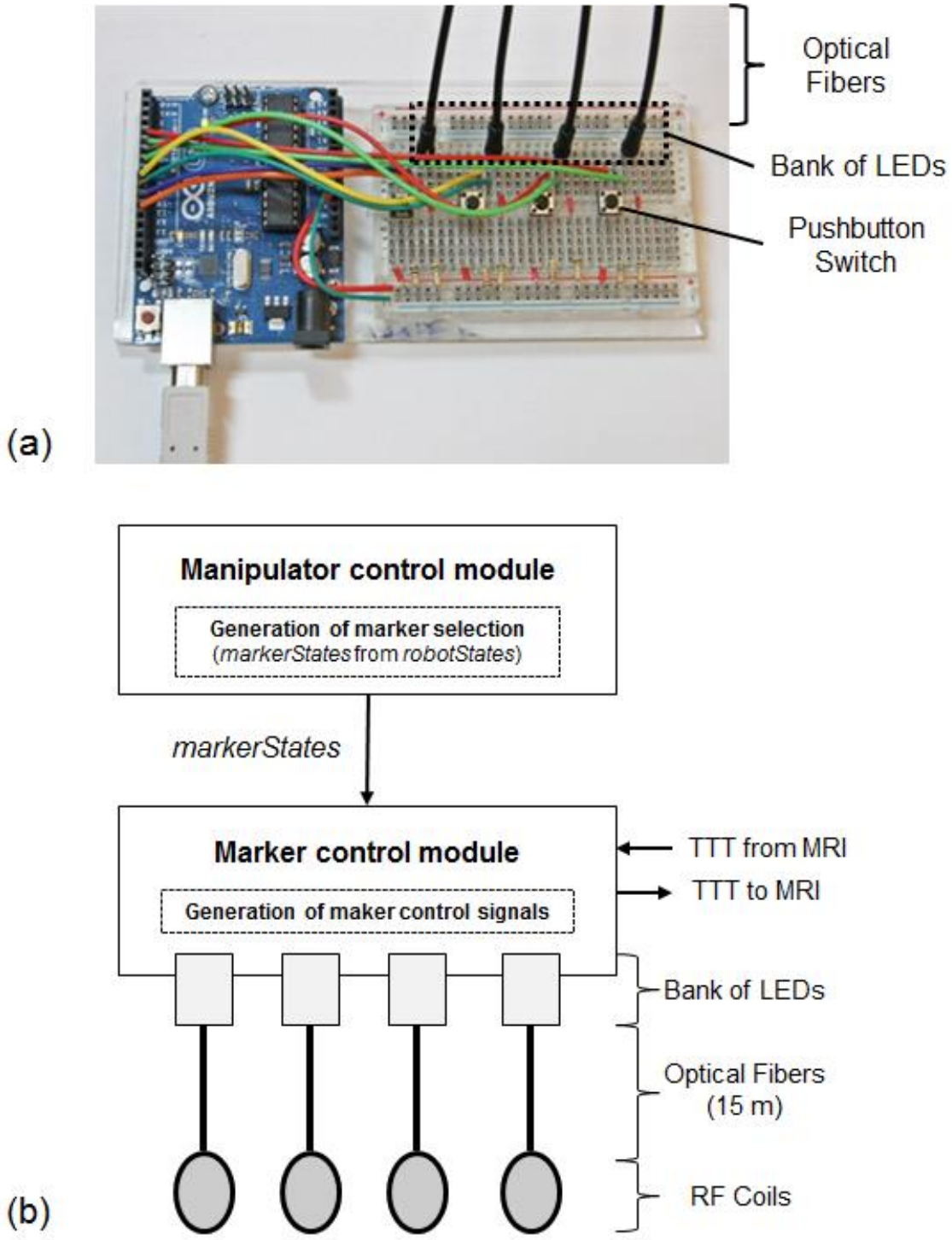

Figure 2.3 (a) Photograph of the marker control circuit by the robot control and (b) diagram of the process flow that links the robot control and marker control.

Figure 2.4 shows the algorithms of manipulator-driven marker selection that run on the manipulator and marker control module. The selective observation of one or multiple markers, i.e., manipulator-driven marker selection and tracking, is determined by the maneuvering degrees-of-freedom (DoF) of the manipulator. The manipulator control module selects which markers are needed to be visible or invisible on the MR image to track the maneuvering portion of the manipulator, generates the N-bit numbers markerStates(J+1) to send them to the marker control module for optically detuning each marker. When the marker control module receives markerStates(J+1), it runs the second algorithm shown in Fig. 2.4 (b), which enables individual marker state (X_M) to '1' when marker X_M is visible (i.e., LED_M is OFF) or enable to '0' when marker X_M is invisible (i.e., LED_M is ON) on the MR images, then triggers the MR scanner for collecting MR images, waits to receive a return TTL pulse from the scanner after MR image acquisition, and finally initializes all markers to put default for the next manipulator maneuver. The algorithm for the manipulator-driven tracking was implemented using only the arm of an MR-compatible manipulator described previously [60, 80].

Figure 2.5 (top) shows a custom-made program written in Microsoft Visual C# that has been developed to switch each LED on or off for optically detuning experiment. A program can communicate with the LED controller through serial communication over the USB cable. When the user manipulates the MR-compatible manipulator using a custom-made software with graphic user interface (GUI) shown in Figure 2.5 (bottom), the software, written in Visual C++ with Insight Segmentation and Registration Toolkit (ITK), Open Graphics Library (OpenGL), Fast Light Toolkit (FLTK), and Visualization ToolKit (VTK) libraries, simultaneously generates the robotStates stream and sends the stream to

the manipulator control module. The manipulator control module maneuvers the manipulator and simultaneously determines, which markers are required to be visible or invisible on the MR images, and generates the markerStates stream from the robotStates stream, finally sends markerStates to the marker control module. The marker control module turns the LEDs ON or OFF for selecting the marker visibility on the MR image and sends a TTL pulse to acquire the MR images and then receives a TTL pulse from the MR scanner when the data acquisition is completed.

(a)

```
input: robotStates(J+1)
output: markerStates(J+1)
Assignments:
joint k is associated with M specific markers
Structure of markerStates = X1X2X3..XN
where XM = 1 when coil is tuned and 0 when detuned
if robotStates(J+1) == robotStates(J)
  set markerStates(J+1) = markerStates(J)
else
  generate new markerStates(J+1)
end if
< send markerStates(J+1) >
```

(b)

```
input: markerStates(J+1)
for each XM
  if XM = 1
    set coil M to tuned
    set rest N-1 coils to detuned (turn on LEDs)
    sent TTL to MRI (iMRI collection starts)
    receive TTL from MRI (iMRI collection finished)
  end if
end for
Set ALL coils to default
```

Figure 2.4 The algorithm of manipulator-driven marker selection that runs on (a) the manipulator control module and (b) the marker control module.

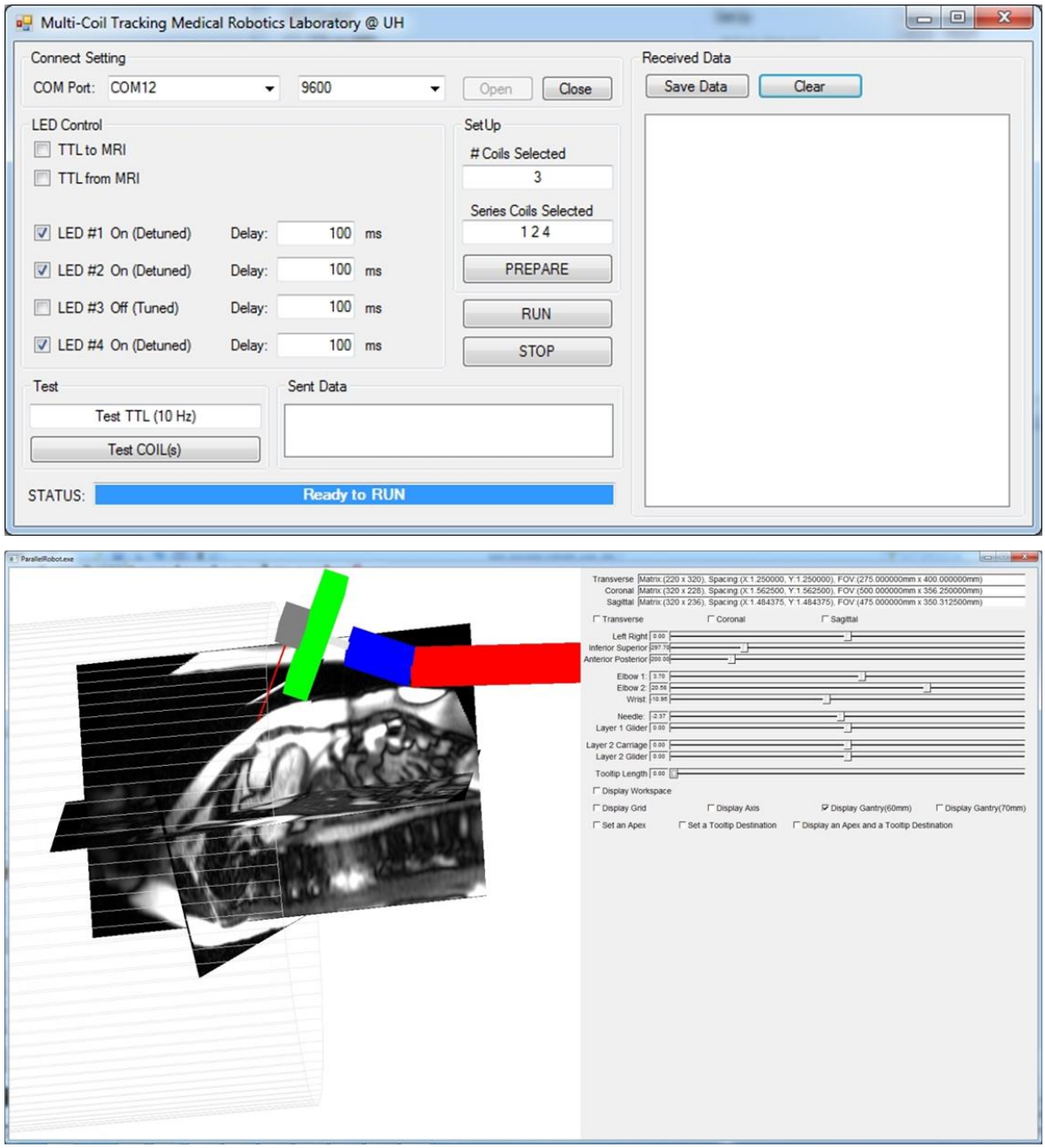

Figure 2.5 Custom-made software for the LED controller (top) and the robot control (bottom).

Figure 2.6 shows our three DoFs robotic arm attached to four MR-visible markers. If rotational DoF-1 (i.e., rotating by an angle ϕ around the X axis) is actuated then markers #1 and #2 are sufficient to calculate its link and the angle of rotation (ϕ). If rotational DoF-

2 (i.e., rotating the end-effector by an angle ψ around the oblique axis that is orthogonal to X) or prismatic DoF-3 (i.e., translating the interventional tool Δ) are actuated then only two marker #3 and #4 are needed to calculate the rotation angle (ψ) or to measure the insertion length (Δ) of the end-effector.

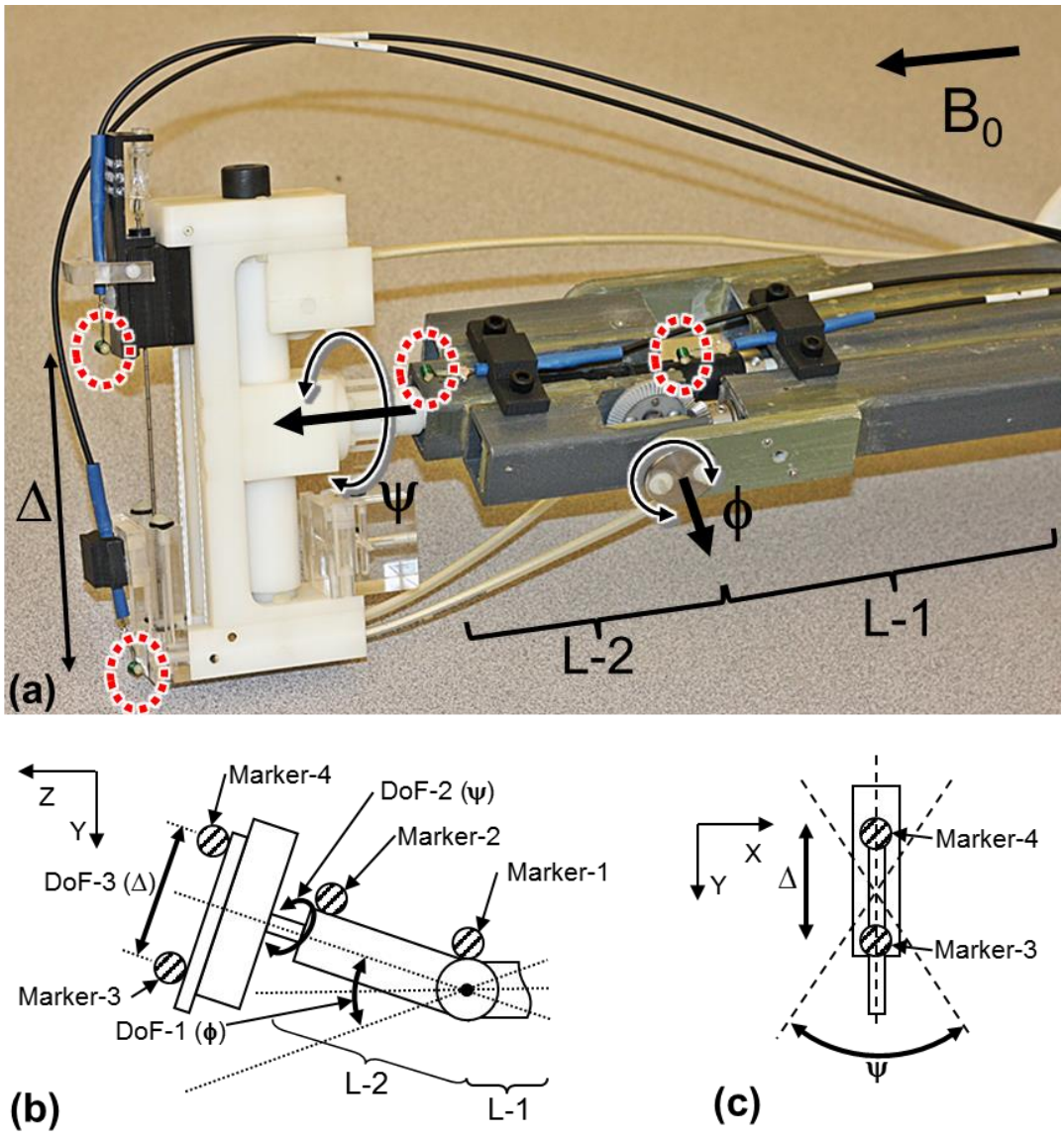

Figure 2.6 (a) Photograph of the robotic arm and 2D representations from (b) the side and (c) front.

2.2.3 MRI Measurements

MR marker imaging was performed with a cylindrical bottle phantom in a 1.5T MRI scanner (MAGNETOM Avanto, Siemens AG, Medical Solutions, Erlangen, Germany). Four MR markers were positioned in a bottle phantom filled with $CuSO_4$ and NaCl doped water which was placed inside the outer volume coil. In order for optimal imaging, all markers were aligned perpendicular to the main magnetic field (B_0) of the scanner because a solenoid coil design does not provide the best signal when aligned parallel to B_0. In addition, all markers were mounted along the X (left-right) direction in a straight line in order to see them together on the MR image. Then, we collected the MR images for tuned and detuned states of MR-visible markers.

For phantom experiments, the marker images were acquired with a TurboFLASH sequence (matrix size = 192 X 140, field of view = 192 X 140 mm^2, slice thickness = 8 mm, TE/TR = 1.75/227.72 ms, flip angle = 1°, bandwidth/pixel = 723 Hz) in the transverse plane. From these MR images, average μ and standard deviation σ of signal intensities were calculated over the markers, background, and bottle phantom.

For the manipulator-driven tracking experiment, we also collected MR images with a TurboFLASH sequence (matrix size = 192 X 152, field of view = 192 X 152 mm^2, slice thickness = 10 mm, TE/TR = 1.41/403.37 ms, flip angle = 3°, bandwidth/pixel = 723 Hz) under different robotStates conditions.

2.3 Results

2.3.1 Q Measurements

The scattering parameter, S_{11} (i.e., the input reflection coefficient of 50Ω terminated output) was measured using inductive coupling of the resonant circuit to a pickup coil (20 AWG, three windings, and 10 mm OD) by the network analyzer (E5061A, Agilent Technologies, Santa Clara, CA) and recorded for the frequency range (10 MHz bandwidth) of interest when the resonant circuit was optically tuned and detuned. When the photoresistor is protected from light, its dark resistance is approximately 11.0 MΩ. When the photoresistor is illuminated by the LED with maximum power, its light resistance drops to approximately 2.6 KΩ and its Q factor, in this case, is extremely decreased. For a parallel RLC resonant circuit, Q factor (Q_p) is proportional to the resistance (R) of the photoresistor by the following formula:

$$\omega_0 = \frac{1}{\sqrt{LC}}, \qquad Q_P = \frac{R}{\omega_0 L} = \omega_0 CR = R\sqrt{\frac{C}{L}} \tag{2.1}$$

Figure 2.7 shows how the resistance influences the Q factor in an RF coil using a photoresistor via an optical fiber. The resistance of a photoresistor was adjusted by light brightness intensity using different amounts of power to the LED. Reduction in the

resistance value is proportional to the reduction of the Q factor in the parallel RLC resonant circuit.

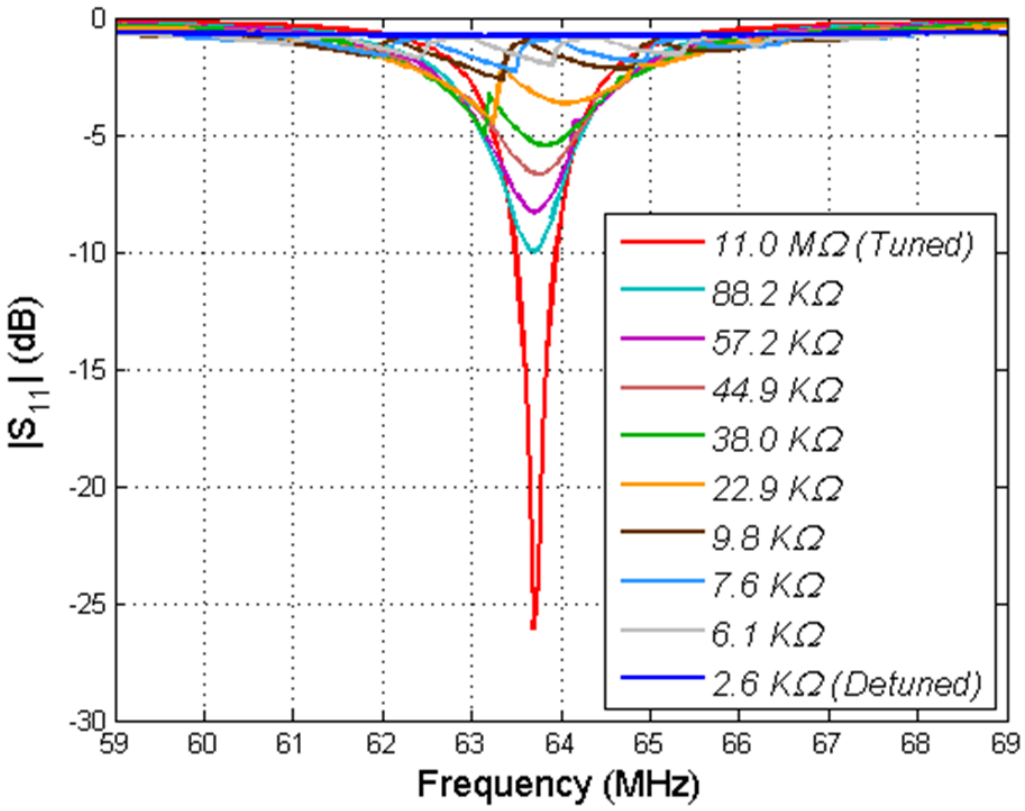

Figure 2.7 Network analyzer plot of S_{11} versus frequency of different photoresistor resistances.

2.3.2 MR Imaging Experiment - 1

The result shown in Figure 2.8 demonstrates the feasibility of the optically detunable MR-visible markers located in the surface of a cylindrical bottle phantom. Four

MR-visible markers are shown as detuned in Fig. 2.8(a) since they have disappeared from the MR image when all LEDs were turned ON. On the other hand, all MR-visible makers are observable as tuned in Fig. 2.8(b) when all LEDs were turned OFF. Each MR marker in Fig. 2.8(e-h) can be turned ON sequentially on the MR image generated sequentially when markerStates = 1111. Fig. 2.8(c) and 2.8(d) show only two markers which are tuned: marker #1 and #4 in Fig. 2.8(c), and marker #2 and #4 in Fig. 2.8(d). The tuned MR markers on the MR image will have much higher intensity than the phantom and the background.

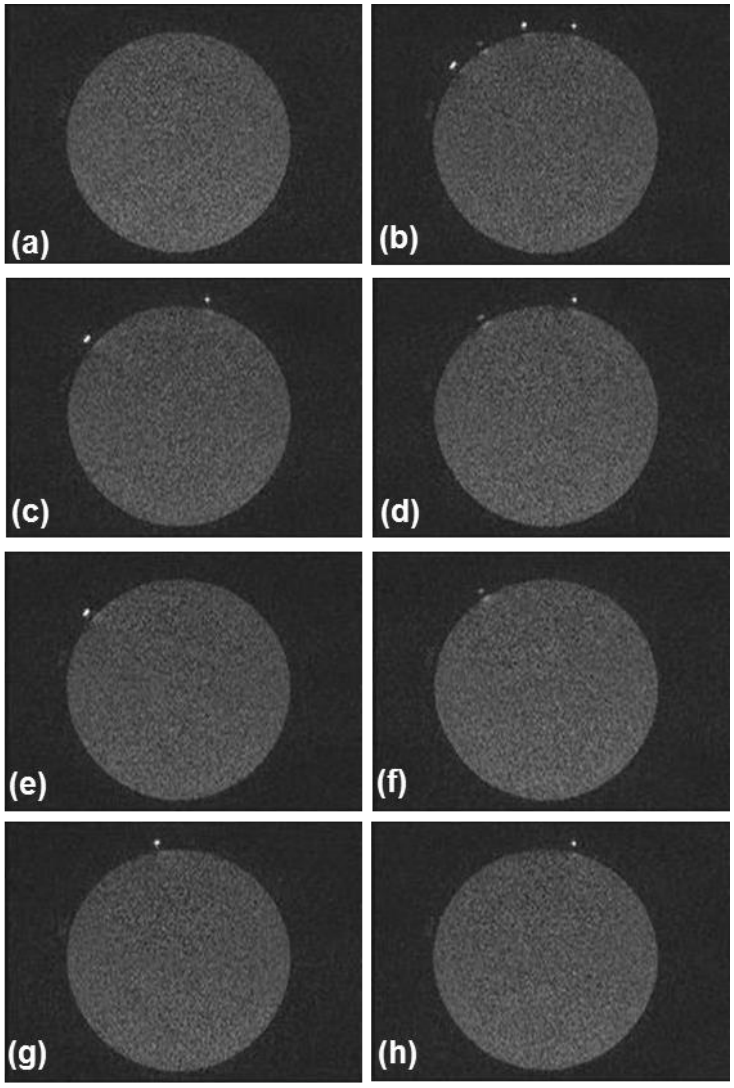

Figure 2.8 Transverse MR images acquired under different markerStates.

Table 2.1 Summary of MR-compatibility studies for the first experiment.

	Marker ($\mu \pm \sigma$)	**Background** ($\mu \pm \sigma$)	**Phantom** ($\mu \pm \sigma$)
Tuned	3263 ± 920	639 ± 55	1227 ± 224
Detuned	689 ± 87	651 ± 60	1371 ± 203

Table 2.1 summarizes the results from the MR-compatibility studies (reporting $\mu \pm \sigma$, n = 4) of MR-visible markers, background, and phantom for tuned and detuned states of markers. More relevantly, the average signal intensity of the MR-visible markers was estimated: marker #1 tuned = 3950 ± 288 and detuned = 725 ± 91, marker #2 tuned = 1759 ± 149 and detuned = 652 ± 69, marker #3 tuned = 3575 ± 612 and detuned = 701 ± 92, and marker #4 tuned = 3013 ± 921 and detuned = 677 ± 78. SI of marker #2 is relatively lower than other markers because a possible explanation for the lack of the SI of marker #2 may be the lack of adequate passive signal source. When the MR markers are tuned, markers are seen as high-intensity objects in the MR image because their average signal intensity differs greatly from the background. However, when they are detuned, the MR markers have a signal intensity similar to the background signal intensity; as such, the MR markers are virtually invisible in the MR image. The background signal intensities were virtually unaffected: 639 ± 55 when all markers were tuned and 651 ± 60 when detuned. In addition, average signal intensity of the bottle phantom was only slightly influenced when all markers tuned (1227 ± 224) and detuned (1371 ± 203).

Figure 2.9 displays 1D profiles for marker #4 along the X and Y axes of the standard DICOM patient-based coordinate system calculated from the corresponding MR images. Solid line is 1D profile signal intensity of detuned marker and the dotted line shows 1D

profile signal intensity of tuned marker. The signal intensity of tuned marker is extremely higher than detuned marker. So, tuned marker can be seen as a white spot on the MR image. There is the big signal intensity gap between tuned marker and detuned marker.

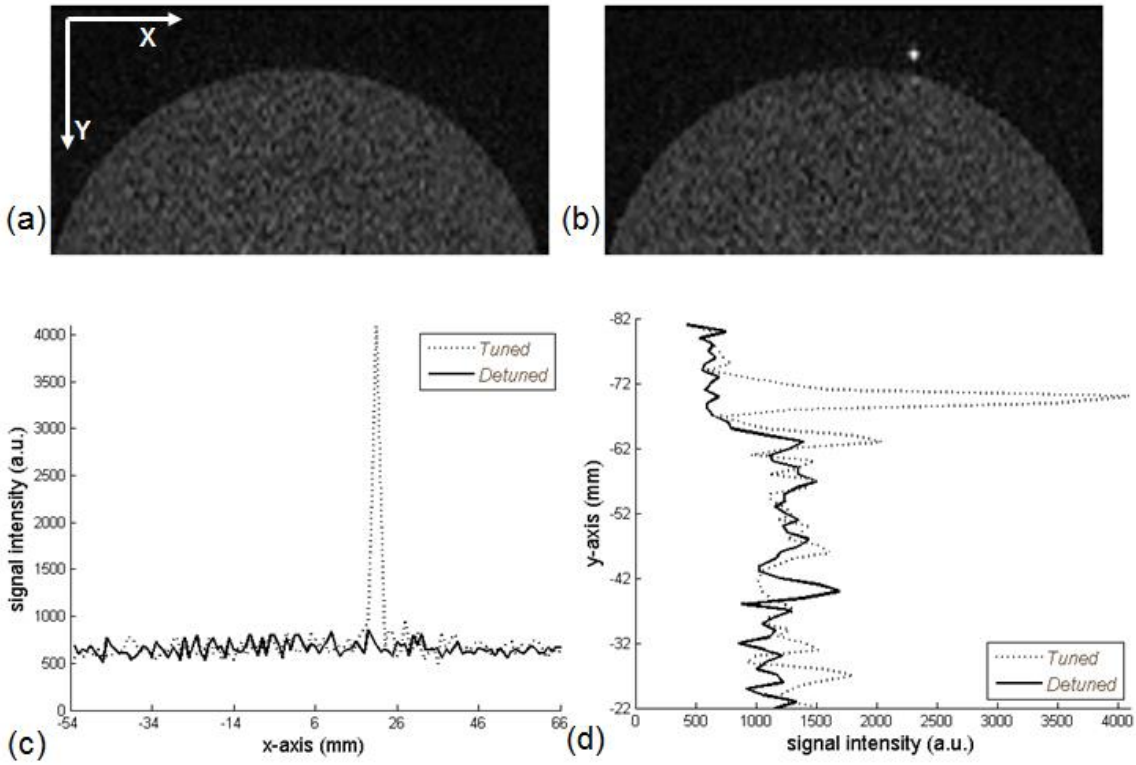

Figure 2.9 MR images with (a) all markers detuned and (b) only marker #4 tuned. 1D projections of signal intensity along the (c) X and (d) Y axes marker #4 when tuned and detuned.

2.3.3 MR Imaging Experiment - 2

Figure 2.10 displays representative transverse MR images collected under different marker conditions. Similar to the first MR imaging experiments, four MR-visible markers are shown as detuned in Fig. 2.10(a); conversely, as tuned in Fig. 2.10(b). Only two markers are tuned: marker #1 and #2 in Fig. 2.10(c), and marker #3 and #4 in Fig. 2.10(d). Figures 2.10(e) to 2.10(h) show result MR images generated sequentially when markerStates = 1111; in consequence, it is sequentially turning ON markers 1, 2, 3 and 4.

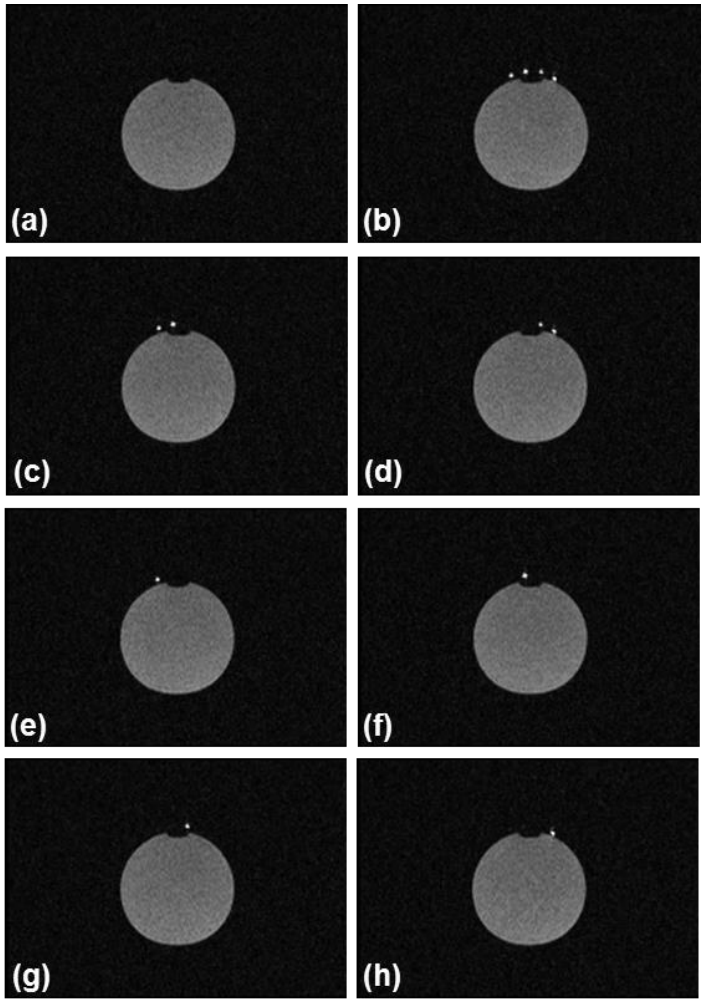

Figure 2.10 MR images collected under different markerStates.

Table 2.2 summarizes the results from the MR-compatibility studies when markers are tuned and detuned. The average of signal intensity of markers, background, and phantom was calculated: markers tuned = 114.21 ± 13.97 and detuned = 6.33 ± 1.59, background tuned = 5.94 ± 1.88 and detuned = 6.13 ± 2.58, and phantom tuned = 42.31 ± 1.74 and detuned = 44.19 ± 3.90. The marker, background and phantom signal intensities were virtually unaffected whether all markers were tuned or detuned.

Table 2.2 Summary of MR-compatibility studies for the second experiment.

	Marker ($\mu \pm \sigma$)	**Background** ($\mu \pm \sigma$)	**Phantom** ($\mu \pm \sigma$)
Tuned	114.21 ± 13.97	5.94 ± 1.88	42.31 ± 1.74
Detuned	6.33 ± 1.59	6.13 ± 2.58	44.19 ± 3.90

Table 2.3 shows the signal intensity results of each marker. The average of signal intensity of each markers is as follows: marker #1 tuned = 107.25 ± 13.15 and detuned = 6.25 ± 2.06, marker #2 tuned = 125.75 ± 13.52 and detuned = 6.50 ± 1.29, marker #3 tuned = 104.67 ± 9.02 and detuned = 6.25 ± 1.71, and marker #4 tuned = 117.67 ± 11.68 and detuned = 6.33 ± 2.08.

Table 2.3 Average of signal intensity of each marker when tuned and detuned.

	Marker #1 ($\mu \pm \sigma$)	**Marker #2** ($\mu \pm \sigma$)	**Marker #3** ($\mu \pm \sigma$)	**Marker #4** ($\mu \pm \sigma$)
Tuned	107.25 ± 13.15	125.75 ± 13.52	104.67 ± 9.02	117.67 ± 11.68
Detuned	6.25 ± 2.06	6.50 ± 1.29	6.25 ± 1.71	6.33 ± 2.08

Figure 2.11 shows MR images of marker #3 when its marker is visible in Fig. 2.11(a) and invisible in Fig. 2.11(b). Also, it displays 1D profiles for marker #3 on the X axis of the DICOM patient-based coordinate system extracted from the equivalent MR images. As shown in Figure 2.11(c), the signal intensity of tuned marker is extremely higher than detuned marker. Therefore, tuned marker can be seen as a white spot on the MR image. There is the big signal intensity gap between tuned marker and detuned marker.

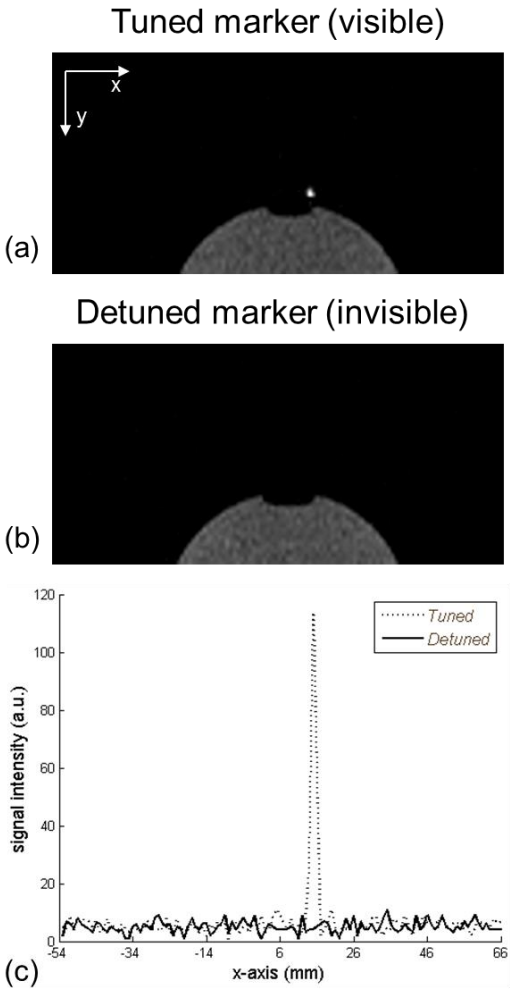

Figure 2.11 MR images with (a) only marker #3 tuned and (b) all markers detuned. 1D projections of signal intensity on the X axis (c) marker #3 when tuned and detuned.

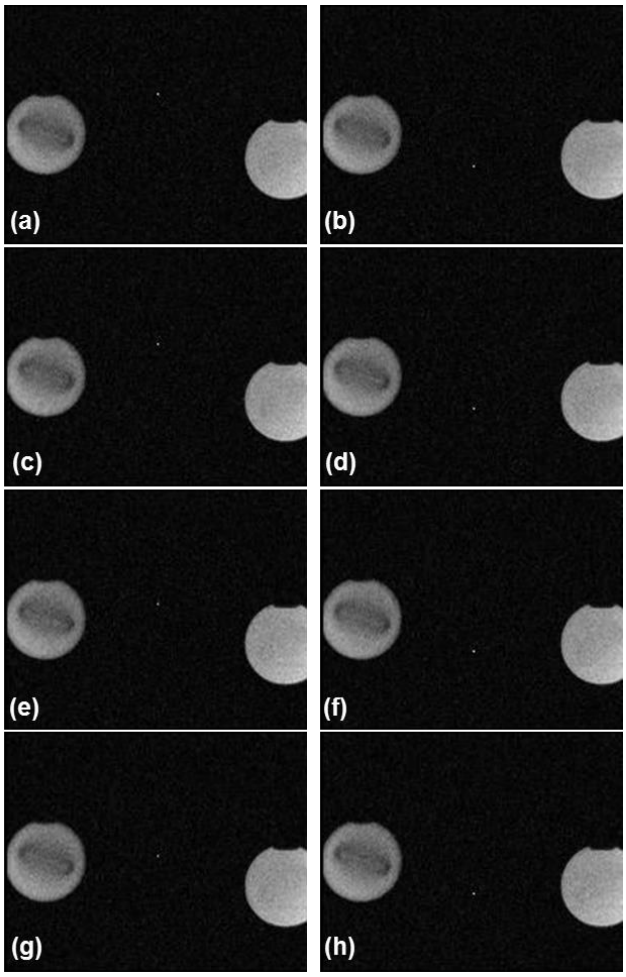

Figure 2.12 Transverse MR images acquired as DoF-3 translates.

Figure 2.12 displays transverse MR images sequentially collected during the actuation of the prismatic DoF-3 (that translates the biopsy needle) detecting the alternative turning ON of markers #3 and #4. When the DoF-3 is actuated, only marker #4 moves down and marker #3 is always in a fixed position. Each marker position is automatically calculated with the nearest neighbor algorithm starting on the voxel of maximum signal intensity in MR image. The Euclidean distances between the two markers during translation of the DoF-3 were automatically calculated to 113.15, 91.02, 66.67, and 51.17 mm, respectively. If only one marker is individually active per MR data acquisition, post-

image processing, e.g., automatic marker detection and automatic position calculation, these kinds of post-image processing times will be faster than detecting many markers per MR image. Post-image processing is faster because only one marker needs to be detected and processed per MR image.

Figure 2.13 shows transverse MR images collected with marker #3 and #4 as ϕ = 0° (i.e., rotational DoF-1 is fixed to 0°) and the rotational DoF-2 rotates the end-effector randomly. The Euclidean distance is automatically calculated based on these two marker positions and its length is 112.51 mm.

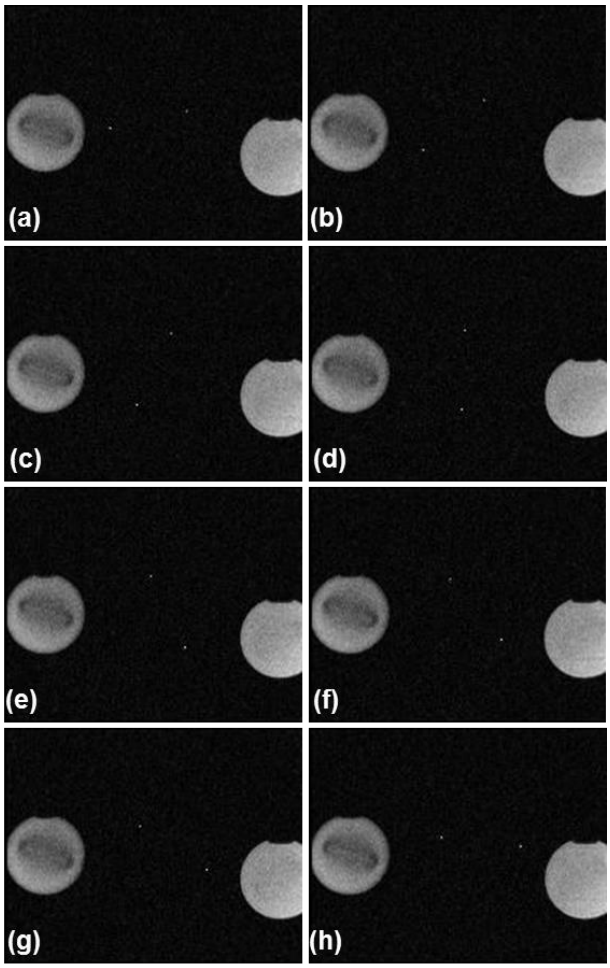

Figure 2.13 Transverse MR images acquired as DoF-2 rotates.

MR imaging experiment was also repeated with solid media transmission (SMT) based robotic system [81, 82] attached to the optically detunable MR-visible marker. Figure 2.14 shows (a) schematic and (b) photograph of the SMT-based robotic system actuated by NEMA 24 stepper motors. The robot, stepper motors inside RF shielded box, and EM1 optical encoders were arranged inside the MR scanner room, and shielded power cables were passed through a penetration panel on the wall of the MR scanner room.

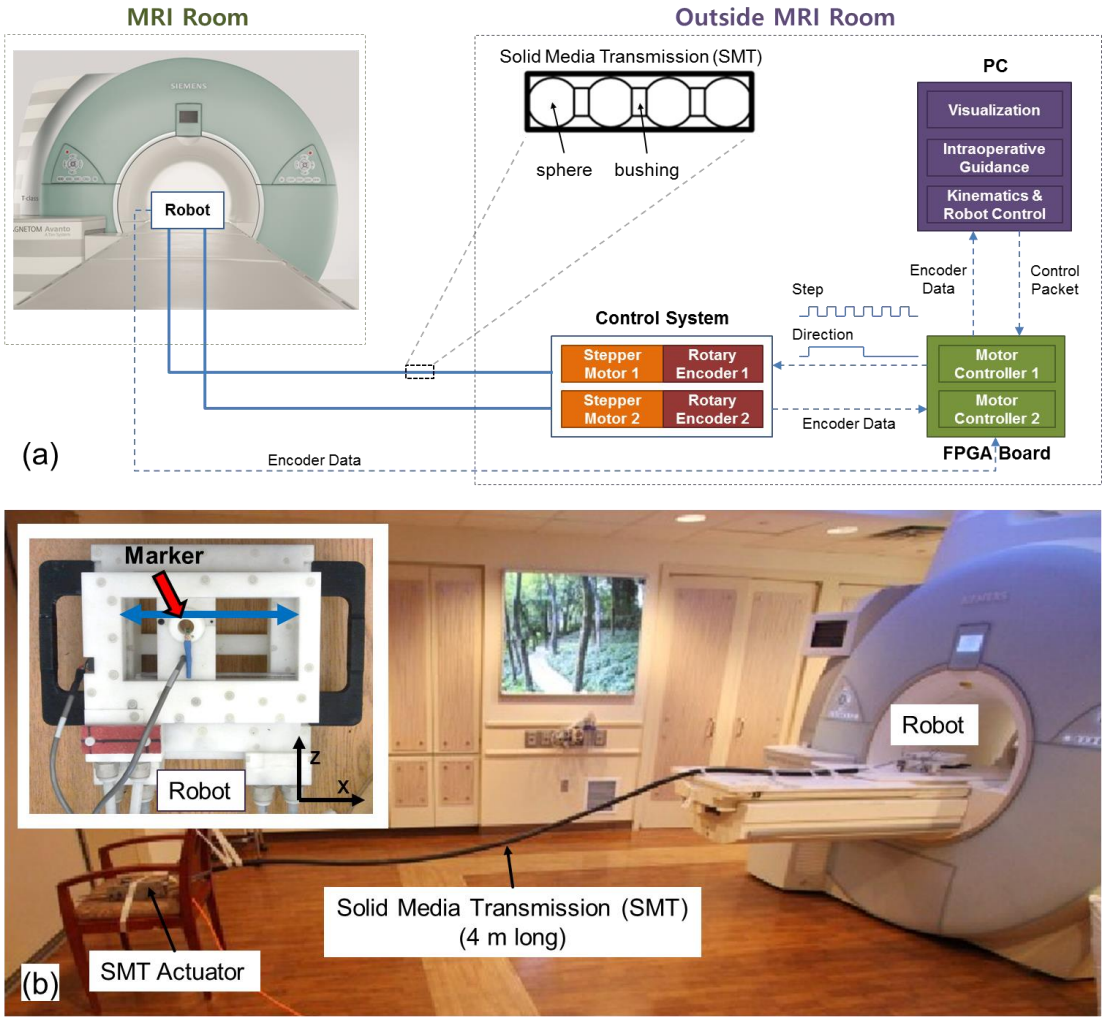

Figure 2.14 (a) Schematic of the SMT based robotic system and (b) photograph of the SMT based robotic system with the MR-visible marker inside the MR scanner room.

Figure 2.15 displays the transverse MR images acquired with a TrueFISP sequence (TE/TR = 1.41/3.22 ms, bandwidth/pixel = 930 Hz, matrix size = 256 X 192, FOV = 380 X 285 mm^2, flip angle = 3°, slice thickness = 3 mm) as the SMT based robot was moving on the x-axis at random. Zipper artifacts induced by stepper motors were shown in Figure 2.15. MR-visible marker occasionally appears blurred and is referred to as a motion blur. A possible explanation for this might be that marker moving speed is faster than MR data acquisition.

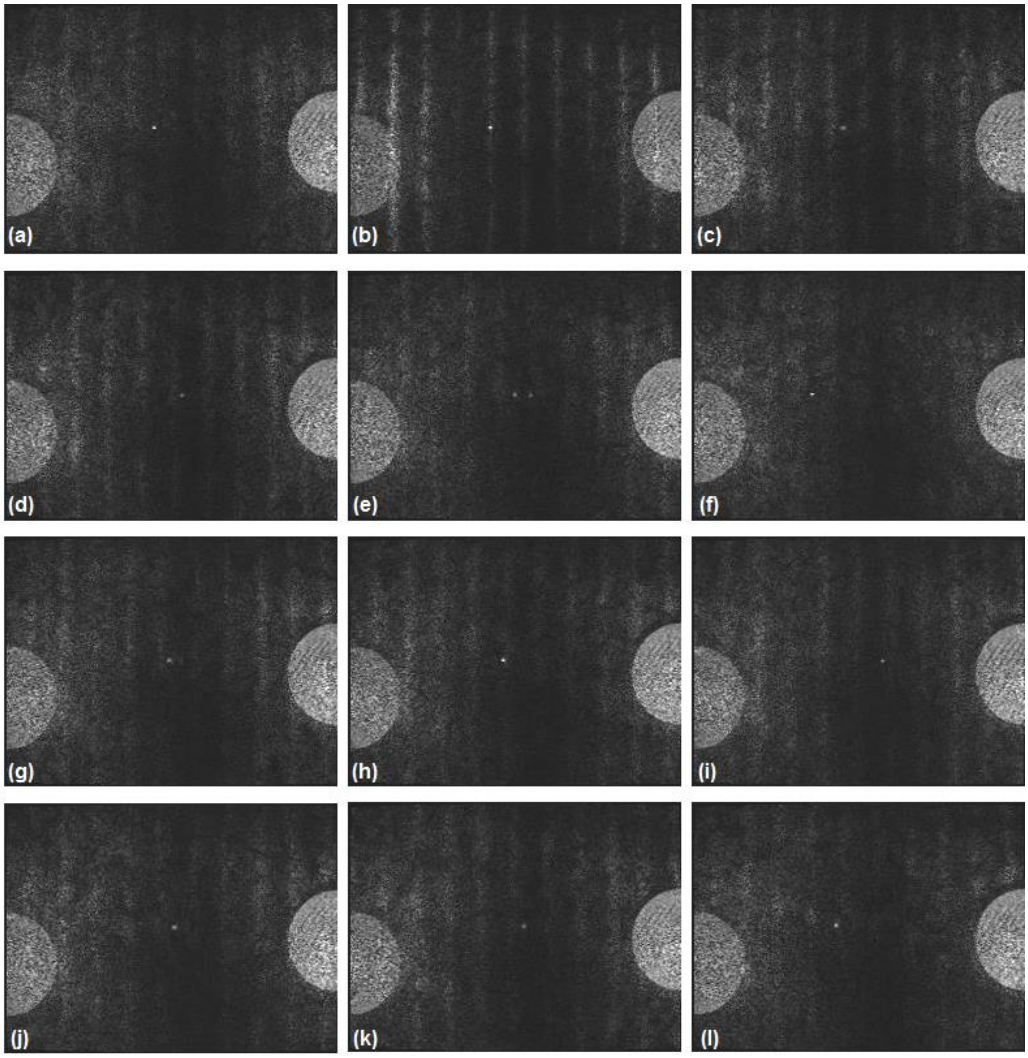

Figure 2.15 (a - l) Transverse MR images as MR-visible marker moves on the x-axis.

2.4 Discussion

Although this study demonstrated linking manipulator and marker control to achieve fast tracking of markers for MR-compatible manipulator, it also has certain limitation which does not affect the described proof-of-concept study. The solenoid coils may not be always optimal when an MR-compatible manipulator maneuvers in 3D because the B_1 rotating magnetic field of the RF coil may not be always perpendicular to B_0. It is calculated using a custom-made MATLAB code that the B_1 axes of marker #1 and #2 are always orthogonal to B_0; otherwise, its B_1 axes of marker #3 and #4 are oblique to B_0 under different robotStates conditions. The rotation matrices of marker #3 and #4 with relation to angles (ω) between B_0 and B_1 is thus obtained as given in the equation below:

$$R_{\phi} = \begin{bmatrix} 1 & 0 & 0 \\ 0 & \cos\phi & -\sin\phi \\ 0 & \sin\phi & \cos\phi \end{bmatrix} \tag{2.2}$$

$$R_{\psi} = \begin{bmatrix} \cos\psi & -\sin\psi & 0 \\ \sin\psi & \cos\psi & 0 \\ 0 & 0 & 1 \end{bmatrix} \tag{2.3}$$

The angles (ω) between B_0 and B_1 is described in Equation 2.4 to 2.7.

$$B_0 = \begin{bmatrix} 0 \\ 0 \\ 1 \end{bmatrix} \tag{2.4}$$

$$B_1 = R_\phi . R_\psi \begin{bmatrix} 1 \\ 0 \\ 0 \end{bmatrix} \tag{2.5}$$

$$\cos \omega = \frac{B_0 . B_1}{||B_0|| ||B_1||} \tag{2.6}$$

$$\omega = \cos^{-1} \left(\frac{B_0 . B_1}{||B_0|| ||B_1||} \right) \tag{2.7}$$

Figure 2.16 displays plot of angles between B_0 and B_1 for marker 3 and 4 when DoF-1 (ϕ) is rotated from 0 to 45 degrees and DoF-2 (ψ) rotates from -90 to 90 degrees. As shown in Figure 2.16(a), when DoF-1 (ϕ) is fixed to 0 degree and DoF-2 (ψ) rotates from -90 to 90 degrees, B_1 is always perpendicular to B_0. However, when DoF-1 (ϕ) is not fixed to 0 degree and DoF-2 (ψ) rotates from -90 to 90 degrees, angles between B_0 and B_1 range 45 to 135 degrees. As also depicted in Figure 2.16(b), when DoF-2 (ψ) is fixed to 0 degree and DoF-1 (ϕ) rotates from -45 to 45 degrees, B_1 is always perpendicular to B_0. However, when DoF-2 (ψ) is not fixed to 0 degree and DoF-1 (ϕ) rotates -45 to 45 degrees, angles between B_0 and B_1 also range 45 to 135 degrees. When DoF-1 (ϕ) is not 0 degree and DoF-2 (ψ) is actuated ranged from -90° to 90°, or DoF-2 (ψ) is not 0 degree and DoF-1 (ϕ) is actuated ranged from -45° to 45°, the B_1 axes of markers #3 and #4 are oblique to B_0. These angles range from 45° to 135° calculated using the above written equations. Because a solenoid coil is not always excellent for tracking manipulator maneuvering, the cross-shaped or figure-8-shaped coil made of two orthogonal coils may be more applicable to track MR-visible markers on articulated manipulators and bendable tools.

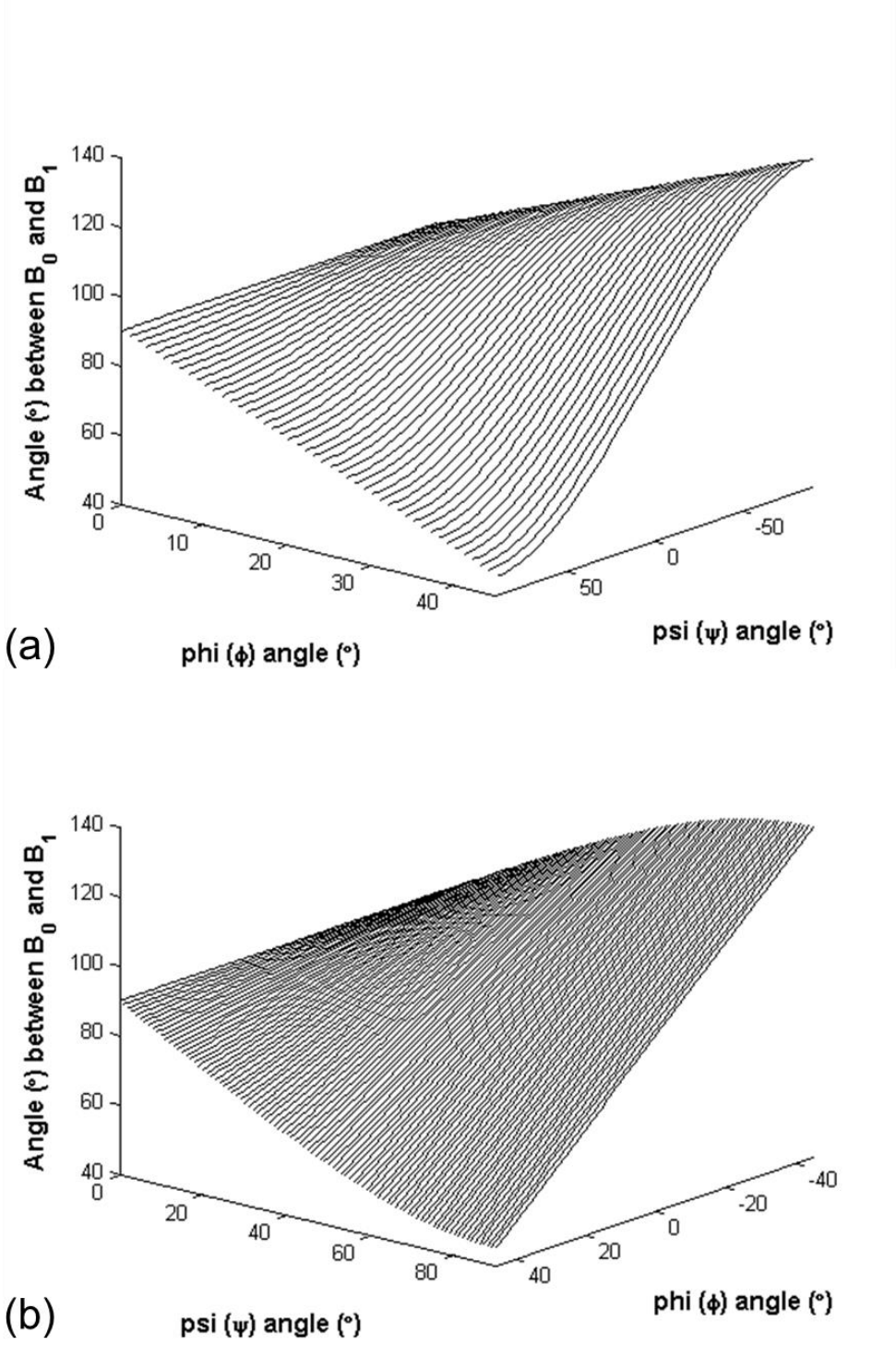

Figure 2.16 (a) Plot of angles between B_0 and B_1 for marker 3 and 4 when DoF-1 (ϕ) is rotated from 0 to 45 degrees and DoF-2 (ψ) moves from -90 to 90 degrees. (b) Plot of angles of B_1 for marker 3 and 4 relative to B_0 when DoF-2 (ψ) is rotated from 0 to 90 degrees and DoF-1 (ϕ) moves from -45 degrees to 45 degrees.

The Denavit-Hartenberg (DH) coordinate frames of the MR-compatible robotic arm are illustrated in Figure 2.17. The robotic arm represents three DoF (RRP: two revolute joints and one prismatic joint) which can be reaching the end-effector in an arbitrary position and orientation in the workspace. The DH parameters of the robotic arm are given in Table 2.4.

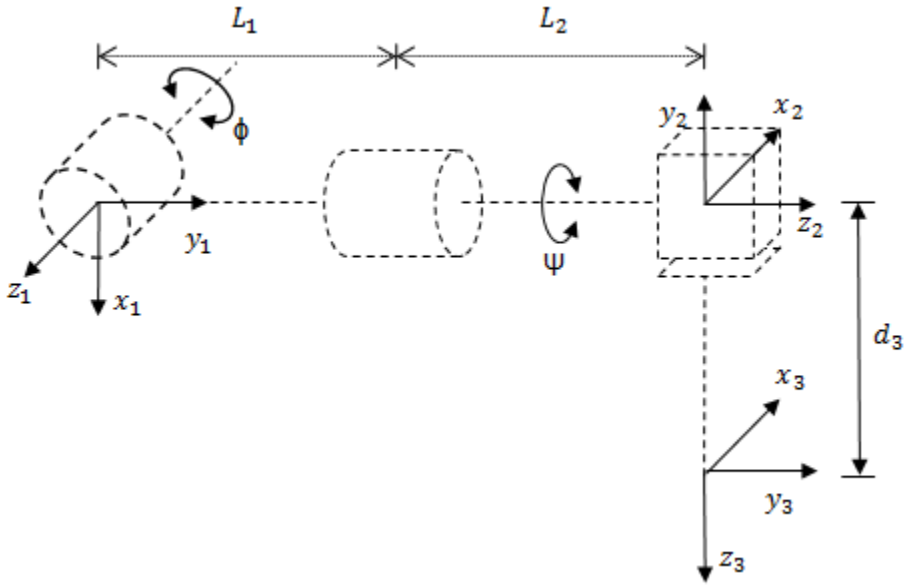

Figure 2.17 DH coordinate frames of the RRP robotic arm.

Table 2.4 DH parameters of the RRP robotic arm.

Link	**a**	**α**	**d**	**θ**
1	0	0	0	ϕ
2	0	$-\pi/2$	$L_1 + L_2$	$\pi/2 + \psi$
3	0	$\pi/2$	d_3*	0

* variable

The response time of the photoresistor may affect significant latency when MR-visible marker is tuned or detuned. In Figure 2.18, we measured approximately the response time of the photoresistor to be a 15 μs for rise time, and 50 ms to 500 ms for fall time using the custom-made circuit and the oscilloscope (TDS2024C, Tektronix, Inc., Beaverton, OR, USA). The rise/fall time of a photoresistor are not equal to the response time, and fall time is largely much slower than rise time.

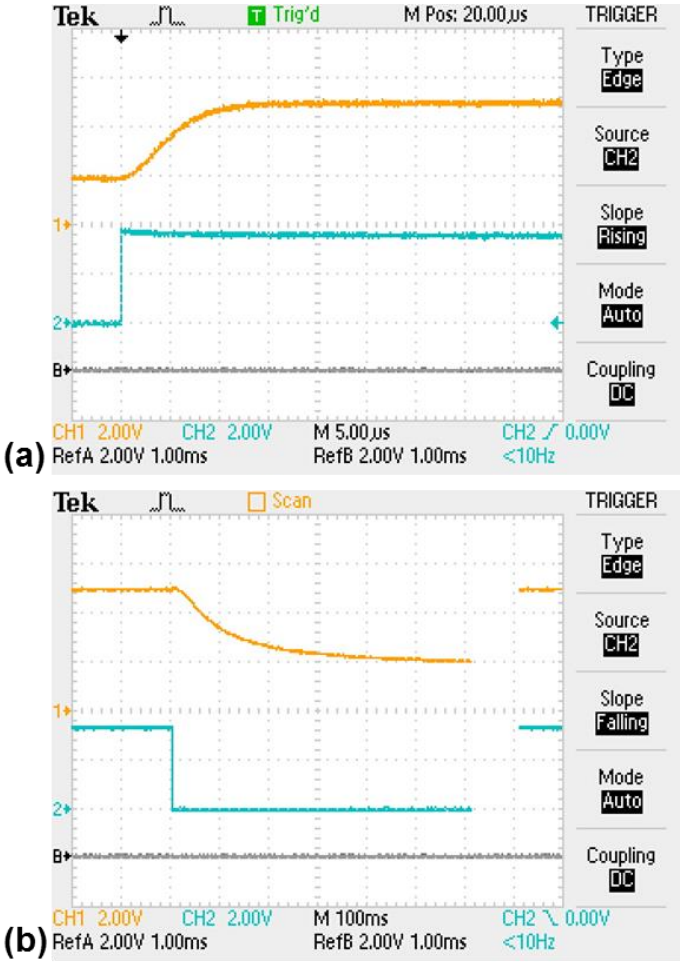

Figure 2.18 Response time result of the photoresistor: rise time (a) and fall time (b).

Accordingly, we have been examining an alternative method to use the PIN photodiode (BPV10NF, Vishay Intertechnology, Malvern, PA) and measured the rise time to 1.2 μs and fall time to 1.75 ms in the same ways as photoresistor.

This study demonstrates the manipulator-driven selection and tracking approach that selectively tuned and detuned by the motion of the maneuvering portion of the manipulator using optically detunable MR-visible markers. This approach can be used to provide rapid data acquisition, advance the unambiguous identification of individual markers, and facilitate MR image post-processing for fast tracking of the markers on MR-compatible manipulators. It can be further employed to track via full two-dimensional imaging or one-dimensional projections in highly articulated robots for or steerable catheters in interventional MRI.

Chapter 3

3 Three-Dimensional Reconstruction of Tubular Structures

The introduction in the field of three-dimensional (3D) reconstruction techniques have been described in Chapter 3.1. Triplanar projection imaging, segmentation and 3D reconstruction, and data processing methods have been described in Chapter 3.2. Experimental results including 3D reconstruction and 3D accuracy analysis have been demonstrated in Chapter 3.3. A brief discussion of the 3D reconstruction of tubular structures from multiple MR projection images is presented in Chapter 3.4.

Chapter 3 is reproduced based primarily upon "3D Reconstruction of Tubular Structures from Three Orthogonal MRI Projections", DOI: 10.1007/978-3-319-32703-7_64 [83] performed in collaboration with Mahmut Unan, Karen Chin, Dipan J. Shah, Andrew G. Webb, Ioannis Seimenis, and Nikolaos V. Tsekos.

3.1 Introduction

Although MRI is a very versatile and powerful diagnostic tool modality, it cannot provide, due to its inherent relatively low sensitivity, instantaneous speed and high spatial resolution afforded with X-ray based modalities such as fluoroscopy and angiography. 3D reconstruction from two projections is well studied in biplane fluoroscopy [84, 85]. However, apart from MR imaging, X-ray and CT scans require exposure to ionizing radiation. In fluoroscopic imaging cases where the two projections that are not orthogonal to each other and the centers of the corresponding field of views (FOVs) are not identical, a series of transformations should be applied to coregister the two projections to a common coordinate system of reference. 3D reconstruction from biplane X-ray images may be limited by the lack of geometric and spatial information for localization, and track the interventional device such as catheter or blood vessels because biplane X-ray images do not provide information about image position and orientation. With MRI, the multiple projections are already inherently coregistered, and the center and size of the FOVs are thoroughly identical. Furthermore, the inherent coregistration and coincidence of the FOV of the multiple projections result in a rather simple geometric processing. When using 2D multislice MR images, however, the speed of imaging and 3D visualization is rather slow. In the field of computer graphics, a visual hull method was proposed by Aldo Laurentini for 3D reconstruction of the object from multiple silhouettes of its object [86]. Also, multiple projection imaging methods were previously described for 3D visualization of active catheters [87-90]. A technique for extracting 3D body and wing kinematics of a

flying insect from three orthogonal shadow images and 3D motion studies have been presented by Ristroph et al. [91]. In this study, in order for planning and guiding interventional devices, we have investigated fast volumetric reconstruction of targeted contrast enhanced (CE) tubular structures, such as catheters and blood vessels, with a simultaneously collecting method - triplanar projection imaging (TPI).

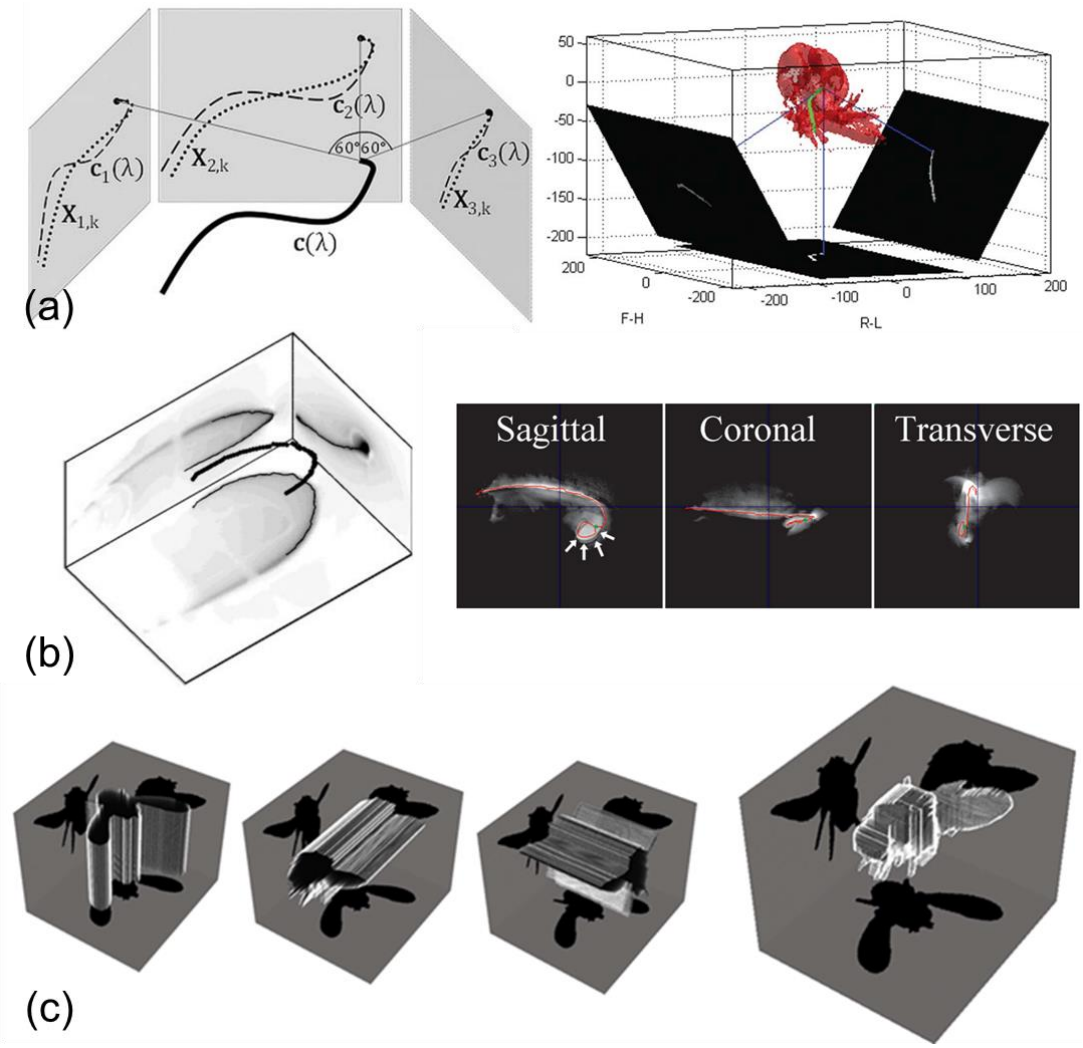

Figure 3.1 (a) 3D reconstruction methods from multiple projection images and shadows: (a) Schirra et al. [90], (b) George et al. [89], (c) Ristroph et al. [91].

3.2 Method

3.2.1 Triplanar Projection Imaging (TPI)

3D reconstruction of an imaged structure entails two independent but interrelated processes. First, the acquisition of the projections and, second, the reconstruction of the structure in the 3D space. Originating from its inherent 'true-3D' capabilities, MRI provides certain benefits in collecting data and facilitating the 3D reconstruction of the imaged structure from its projections: (a) The inherent coregistration of the spatial encoding on the three projections makes axes assignment and matching straightforward. (b) The orientation of the imaged volume can be set to any arbitrary plane relative to the structure which can be used to better resolve it, thus reducing the number of needed projections and computational resources required from the reconstruction algorithm. (c) The angle between the projection planes can be adjusted to any desired value and is not limited to orthogonal. More than two MR projection images can be used to resolve more complex or highly tortuous structures. This proof-of-concept work is focused on an acquisition scheme based on three orthogonal MR projection images. Figure 3.2(a) illustrates the operation of the method that collects three projections by setting the thickness of the slice in each acquisition (Fig. 3.2(b)) equal to the FOV encoded by the phase and readout gradients.

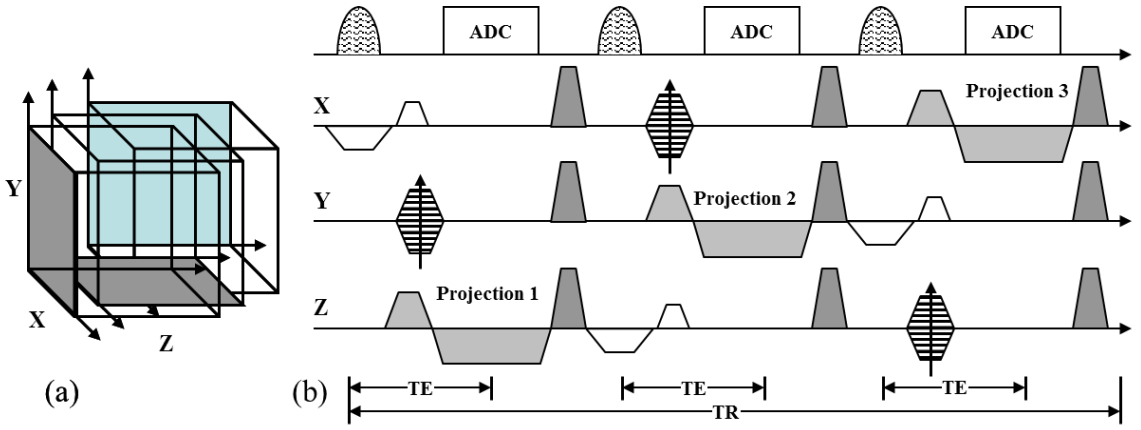

Figure 3.2 Acquisition method of three projection images - repetition time (TR) echo time (TE) and analog-to-digital converter (ADC).

3.2.2 TPI Acquisition

Without loss of generality, we hypothesize that the interest is to visualize the tubular structure of choice without any background signal. This can further simplify the segmentation and the 3D reconstruction of the structure. In the experimental part, therefore, we filled the tubular structure with T1-shortening Gd agent and used magnetization preparation to the implemented sequences to achieve long T1 species background suppression.

The TPI sequence was evaluated on a phantom made of a Gd-filled (3% Gd-doped water) tube (3.0 mm ID and 4.0 mm OD) embedded into a container filled with a fat substance that is 53% vegetable oil. MR projection images were acquired using a 1.5 Tesla whole body MRI scanner (MAGNETOM Avanto, Siemens AG, Medical Solutions, Erlangen, Germany) and the standard built-in body coil was used for transmit (Tx) and

receive (Rx). First, a 2D multislice set of 128 coronal slices was collected as a reference with a standard inversion recovery gradient recalled echo (GRE) sequence (TR/TE = 3.8/1.52 ms, flip angle = 40°, bandwidth/pixel = 592 Hz, matrix size = 384 X 264, FOV = 191 X 131 mm^2, slice thickness = 1.3 mm). Then three MR projections (i.e., a TPI set) were collected along the sagittal, transverse and coronal planes using T1 weighted fast imaging with the steady-state precession (TrueFISP) pulse sequence (TR/TE = 26.07/3.71 ms, flip angle = 75°, bandwidth/pixel = 250 Hz, matrix size = 256 X 256, FOV = 200 X 200 mm^2, slice thickness = 200 mm).

3.2.3 Segmentation and 3D Reconstruction

Figure 3.3 is the flowchart of the process followed to generate the 3D reconstruction of the structures from a TPI set: (a) acquisition of the three orthogonal projections, (b) segmentation of the contrast enhanced tubular structure in the three MR projections, (c) backprojection of segmented objects into the 3D volume, (d) calculation and 3D reconstruction of the intersection volume from the three backprojected objects, and (e) calculation of the centerline curve for 3D accuracy analysis. This processing was performed offline with a custom-made software implemented in MATLAB.

The algorithm for the segmentation of the structure in each 2D MR projection included sharpening, edge detection, and object boundary segmentation. First, to enhance the boundaries of the tubular structure (i.e., versus the background matrix) we applied unsharp masking [92]. Edge detection was then followed that was based on the Sobel

operator [93, 94]. Finally, object boundary segmentation was applied, based on the Legendre Level Set algorithm to detect the boundaries of the tubular structure on each MR projection image [95]. The parameters for each process, such as the region and position of the initialization mask for object boundary segmentation, were manually adjusted on the software GUI.

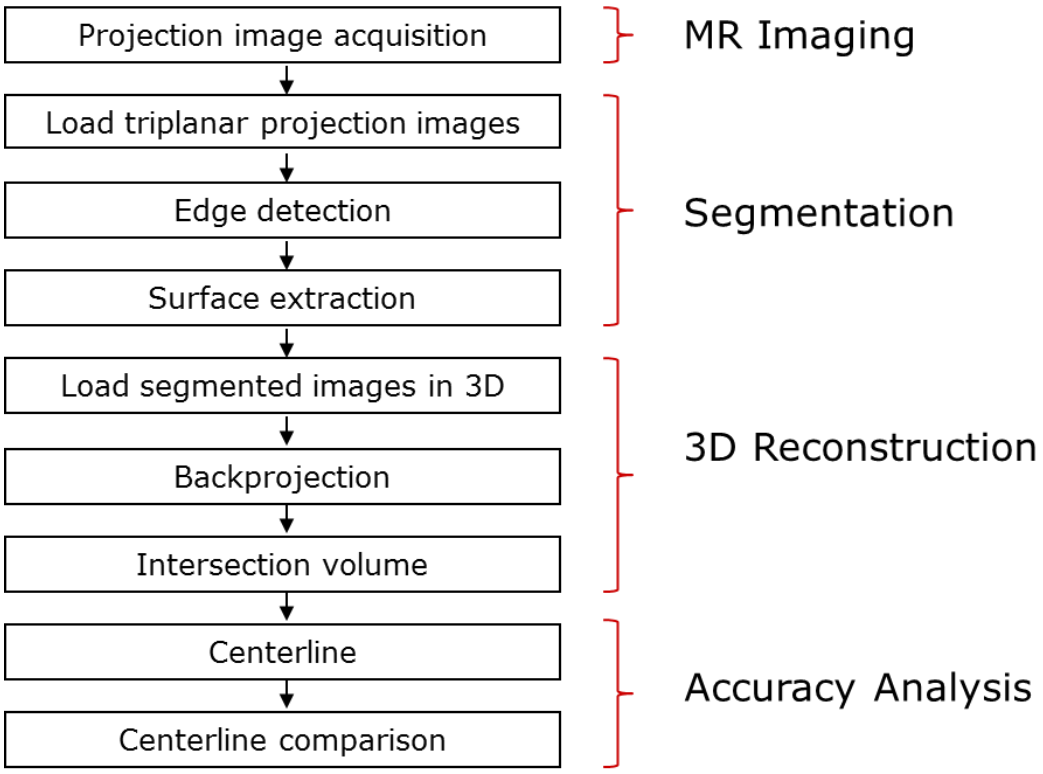

Figure 3.3 Flowchart of the 3D reconstruction process.

The segmented structures on each one of the three MR projections were then backprojected along the X axis for the sagittal (Y and Z scanner axes), the Y axis for the coronal (X and Z scanner axes) and the Z axis for the transverse (X and Y scanner axes) MR projections. The intersection volume of the three backprojections was calculated with

Algorithm 1 in Figure 3.4. With this algorithm, intersection points were calculated from point sets (i.e., $\boldsymbol{p_C}$ of coronal, $\boldsymbol{p_S}$ of sagittal, and $\boldsymbol{p_T}$ of transverse) in set $\boldsymbol{B_C}$ of coronal, $\boldsymbol{B_S}$ of sagittal, and $\boldsymbol{B_T}$ of transverse backprojected volumes with a logical AND operator. 3D volume model of a tubular structure was extracted using the marching cube algorithm [96].

Algorithm 1. Match driven backprojections
input: B_C, B_S, B_T
output: M

```
1: for each point p_S in B_S
2:     for each point p_T in B_T
3:         for each point p_C in B_C
4:             if p_C & p_S & p_T = 1 then
5:                 M ← p_C
6:             end if
7:         end for
8:     end for
9: end for
```

- point set $\boldsymbol{p_C}$ of coronal, $\boldsymbol{p_S}$ of sagittal, and $\boldsymbol{p_T}$ of Transverse
- point set $\boldsymbol{B_C}$ of coronal, $\boldsymbol{B_S}$ of sagittal, and $\boldsymbol{B_T}$ of transverse backprojected volumes
- intersection volume $\boldsymbol{M}$

Figure 3.4 Algorithm of match driven backprojections.

3.2.4 Data Processing

The 3D object reconstructed from the TPI data was compared to the object reconstructed from the multislice (128 coronal multislices), that was also generated with the same segmentation algorithm. The voxel data were stored in 3D array structures to extract the polygonal meshes of the isosurfaces with marching cubes. Skeleton extraction, based on the L1-medial skeleton algorithm [97], was then performed to extract the corresponding centerlines of the two 3D renderings of the tubular structures. The skeleton extraction algorithm also calculates the minimum number of points required to generate the centerline of the structure. In general, this number depends on the 3D shape and size of the structure [97]. For the shapes extracted from the TPI and multislice datasets, the algorithm retuned a minimum of 38 points that was used in all processing. For each point on both skeletons, we calculated the coordinates (X_{3d}, Y_{3d}, Z_{3d}) and (X_{msl}, Y_{msl}, Z_{msl}), where '3d' are the coordinates of the points on the centerline generated from the TPI and 'msl' of the corresponding points on the centerline from the multislice set, their differences along the three axes and their Euclidean distance $\mathrm{sqrt}[(X_{3d}-X_{msl})^2 + (Y_{3d}-Y_{msl})^2 + (Z_{3d}-Z_{msl})^2]$. Those values were then reported as averages and standard deviations (reporting $\mu \pm \sigma$, $n = 38$). Also, spline curves were generated in 3D using the spline interpolation algorithm [98, 99] and their differences on the corresponding X, Y and Z axis coordinates were measured.

3.3 Results

Figure 3.5 displays the original unprocessed 2D MR projections (upper row), the corresponding edge detection (middle row) using the Sobel method [93, 94], and segmentation results (lower row) using the boundary segmentation algorithm [95]. This processing was based on the assumption that the background signal from the fat substance was sufficiently saturated; therefore, it is possible to segment out the tubular structure. While those data were successful in the reconstruction of the 3D structures, there are some notable limitations. The background signal was not fully suppressed. The signal intensity of the contrast enhanced structure was 39.44 ± 11.48 as compared to a matrix signal intensity of 16.06 ± 4.07. Suboptimal suppression of the background matrix signal intensity occurred because of (1) the imperfect inversion of the inversion recovery magnetization preparation module of the pulse sequence used that was employing a non-selective RF pulse, (2) the background signal originates from a total volume of 200 x 200 x 200^3; therefore, any unsuppressed signal adds to a large value. Also, preparation of the blood vessel mimicking phantom was not ideal since air was trapped giving rise to the signal artifacts that resulted to the isolation of other background structures (especially, seen in the transverse slice) that were manually removed before backprojections. Finally, the voxels within the boundary was automatically included as being part of the segmented tubular structure. After segmentation of a tubular structure from each MR projection image, three segmented MR projection images were placed into 3D space based on the standard DICOM patient-based coordinate system.

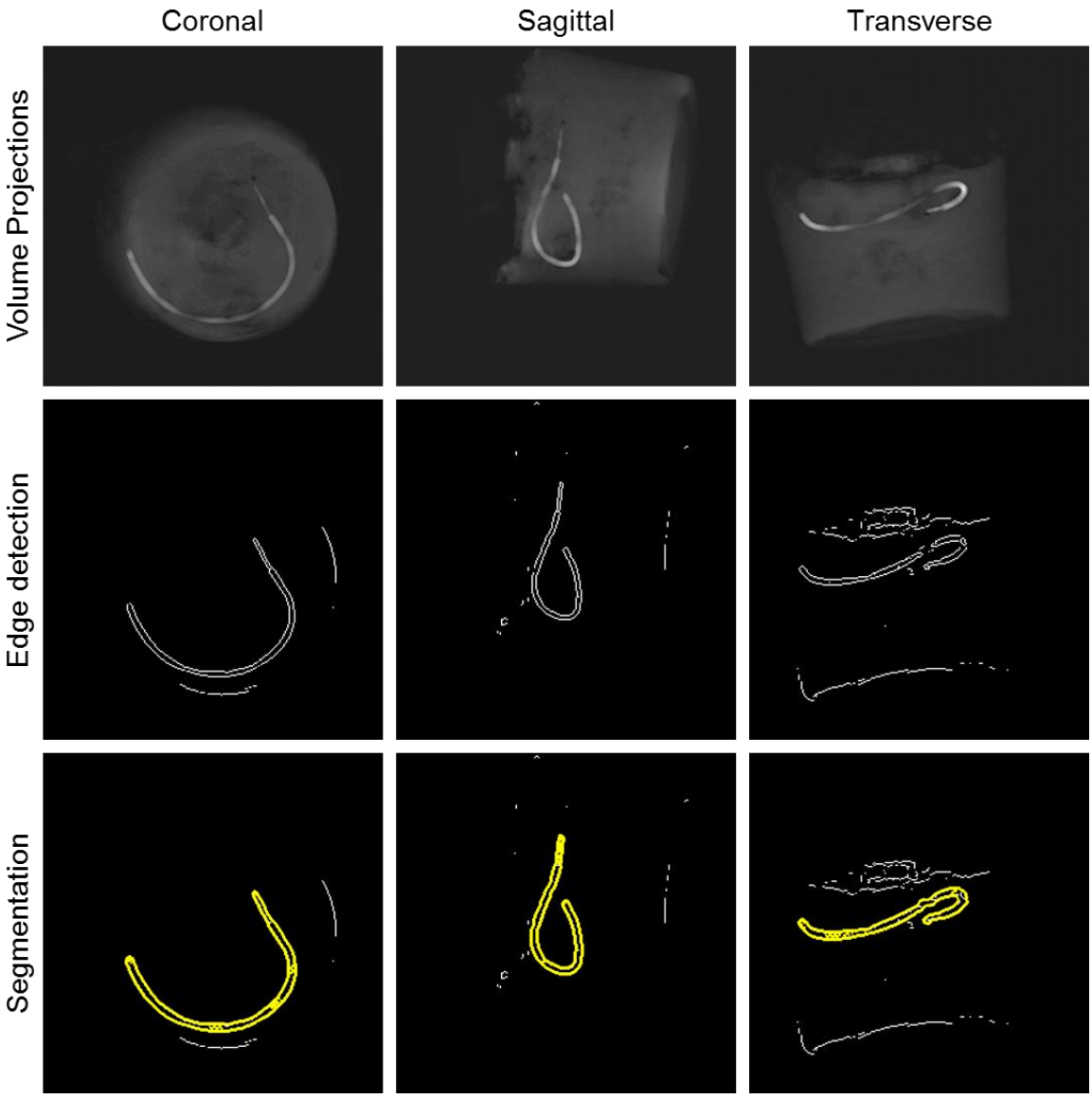

Figure 3.5 The three projection images acquired (upper row), and the result after edge detection (middle row) and segmentation (lower row).

Figure 3.6 displays the 3D rendering of the tubular structure reconstructed from the TPI set using Algorithm 1 in Figure 3.4, together with the three acquired MR projections. The reconstructed structure has the shape of the original object as compared to the arrangement of the tube inside the phantom.

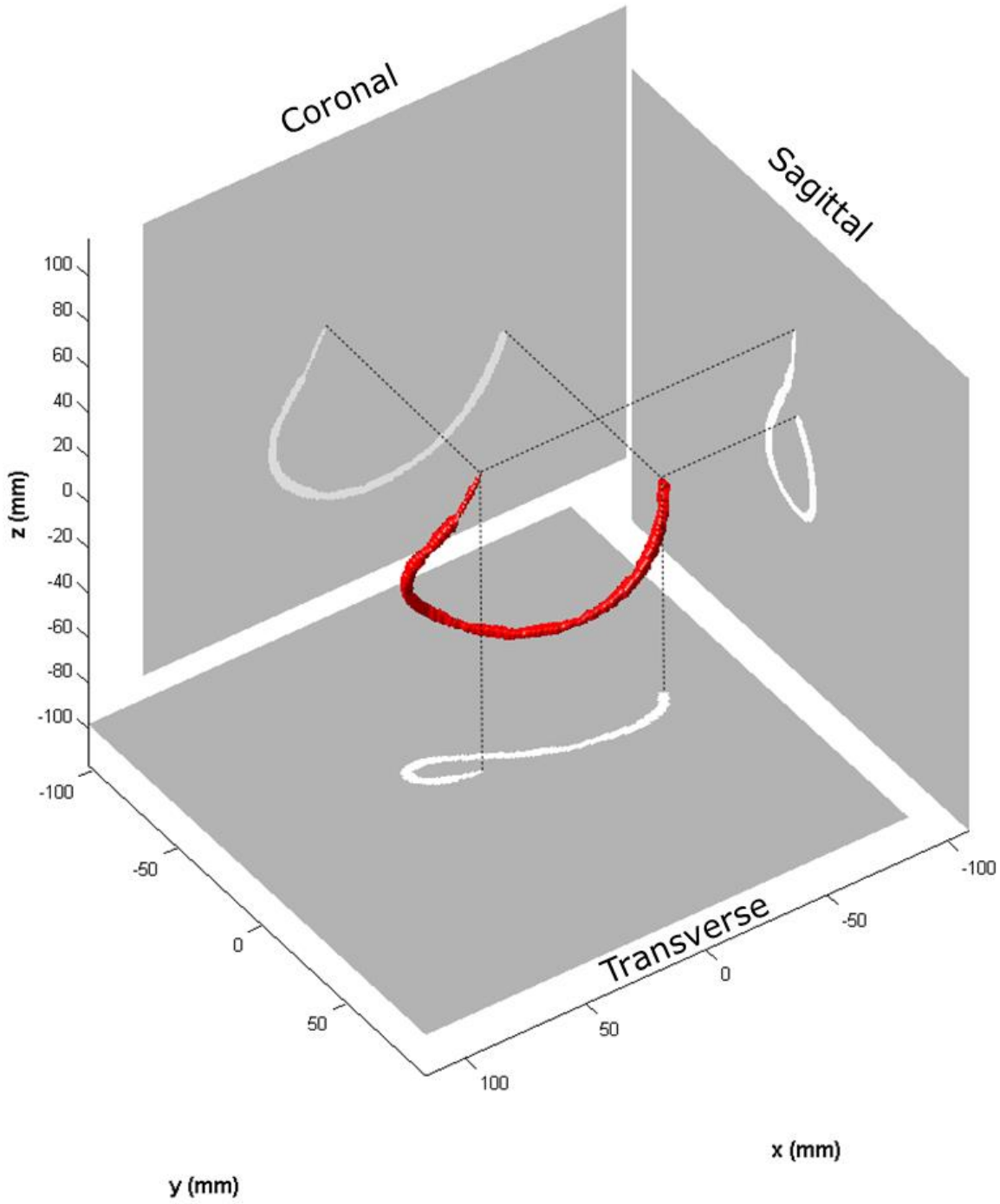

Figure 3.6 TPI-based 3D surface rendering of the tubular structure and the corresponding three orthogonal 2D projections.

Figure 3.7 shows two 3D reconstructed models from three orthogonal MR projection images (a) and 128 coronal multi-slice images (b).

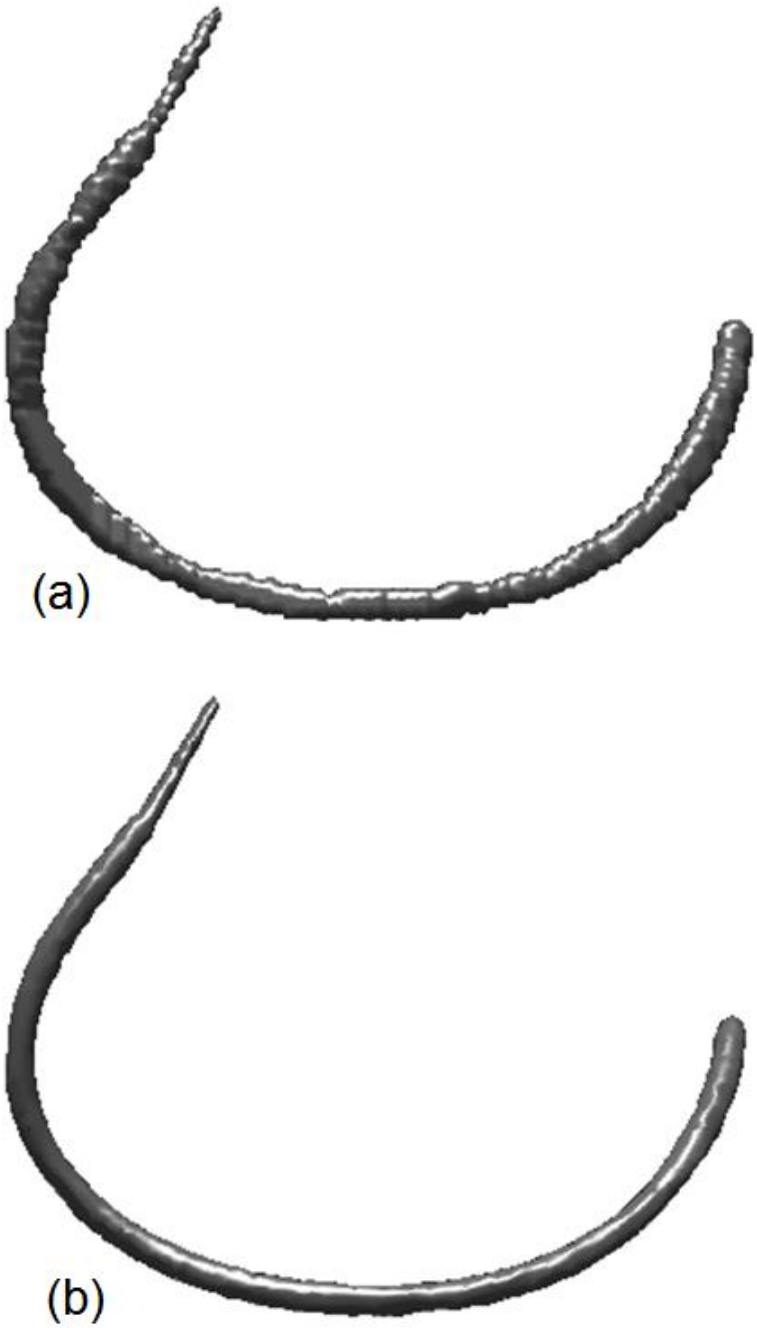

Figure 3.7 3D reconstructed models from the TPI (a) and 128 coronal multi-slice images (b).

Figure 3.8 displays the 3D model reconstructed from three orthogonal MR projection images with the extracted centerline curve.

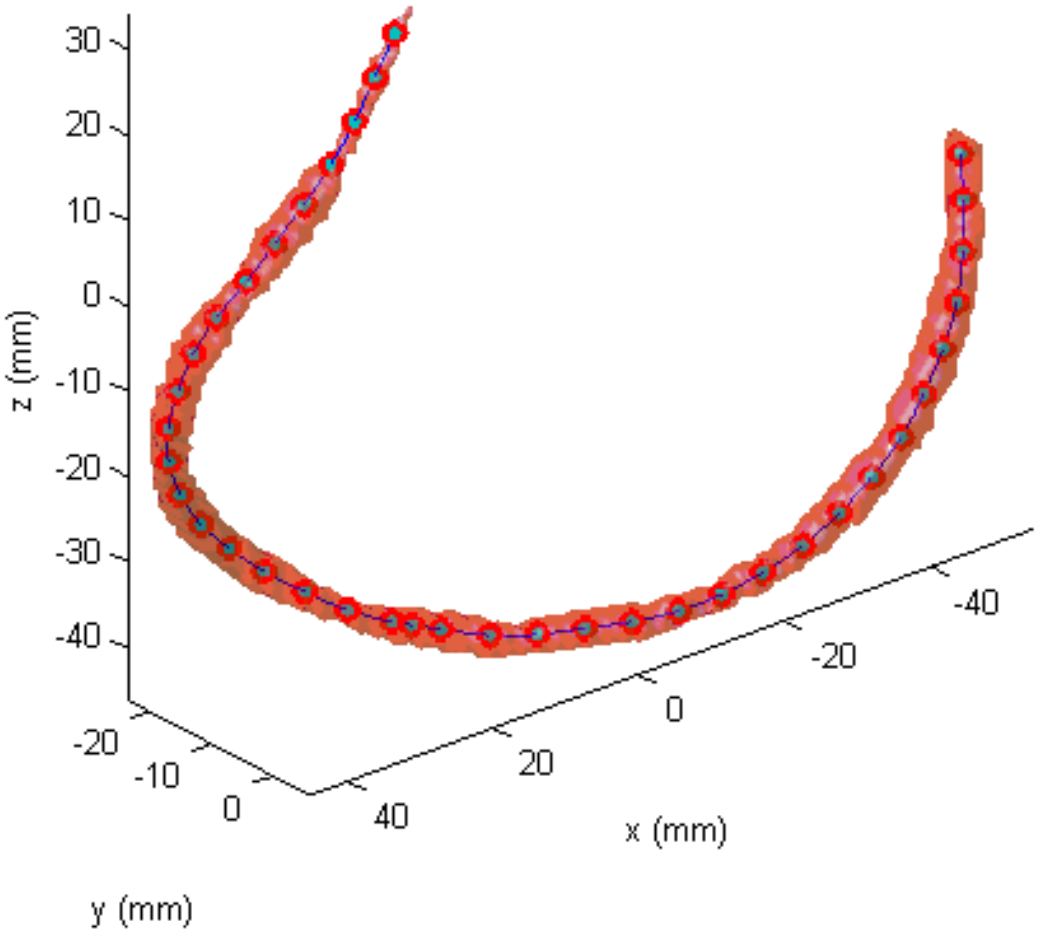

Figure 3.8 3D reconstructed model with extracted centerline curve.

Figures 3.9 and 3.10 show and compare superimposed the two 3D centerlines generated by the TPI and the multislice set demonstrating, in qualitative terms, a good matching of the two curves. Although the two data sets were collected with different resolutions (the pixel size for the multislice set is 0.48 mm and for the TPI is 0.78 mm), some quantitative appreciation of their matching can be calculated. Specifically, the 3D

Euclidean distance between their points was 1.73 ± 0.80 mm. The differences on the corresponding X, Y and Z axis coordinates were 1.21 ± 0.83 mm, 0.56 ± 0.41 mm and 0.84 ± 0.55 mm, respectively. Also, centerline differences from spline curves on the corresponding X, Y and Z axis coordinates were calculated to approximately 0.86 ± 0.69, 0.49 ± 0.32 and 0.76 ± 0.41, respectively. The spline curve's average μ and standard deviation σ were 0.70 ± 0.52 mm (μ ± σ). It appears that the largest difference in the matching of the two centerlines originates from the X axes as can also be appreciated in Figs. 3.9 and 3.10.

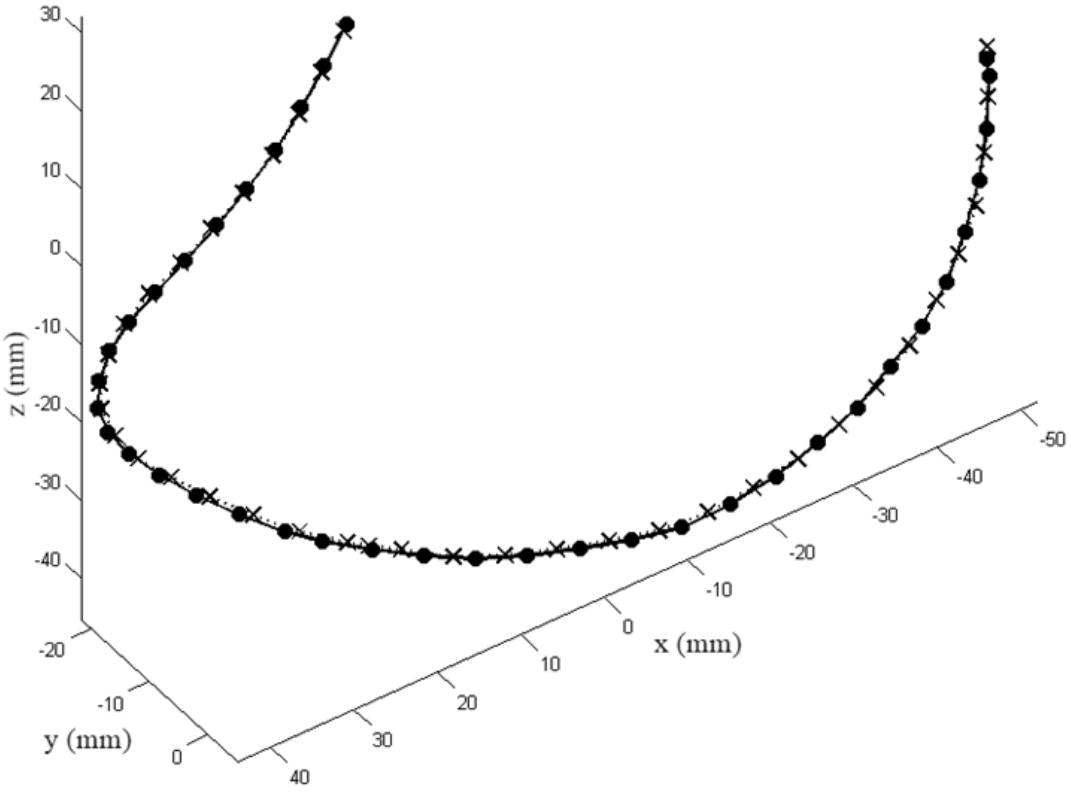

Figure 3.9 Comparison of the centerlines of the 3D renderings generated from the three projection images (solid line with circle markers) and from the multislice MR images (dotted line with cross markers). Each line represents the spline curve and each marker the corresponding data points.

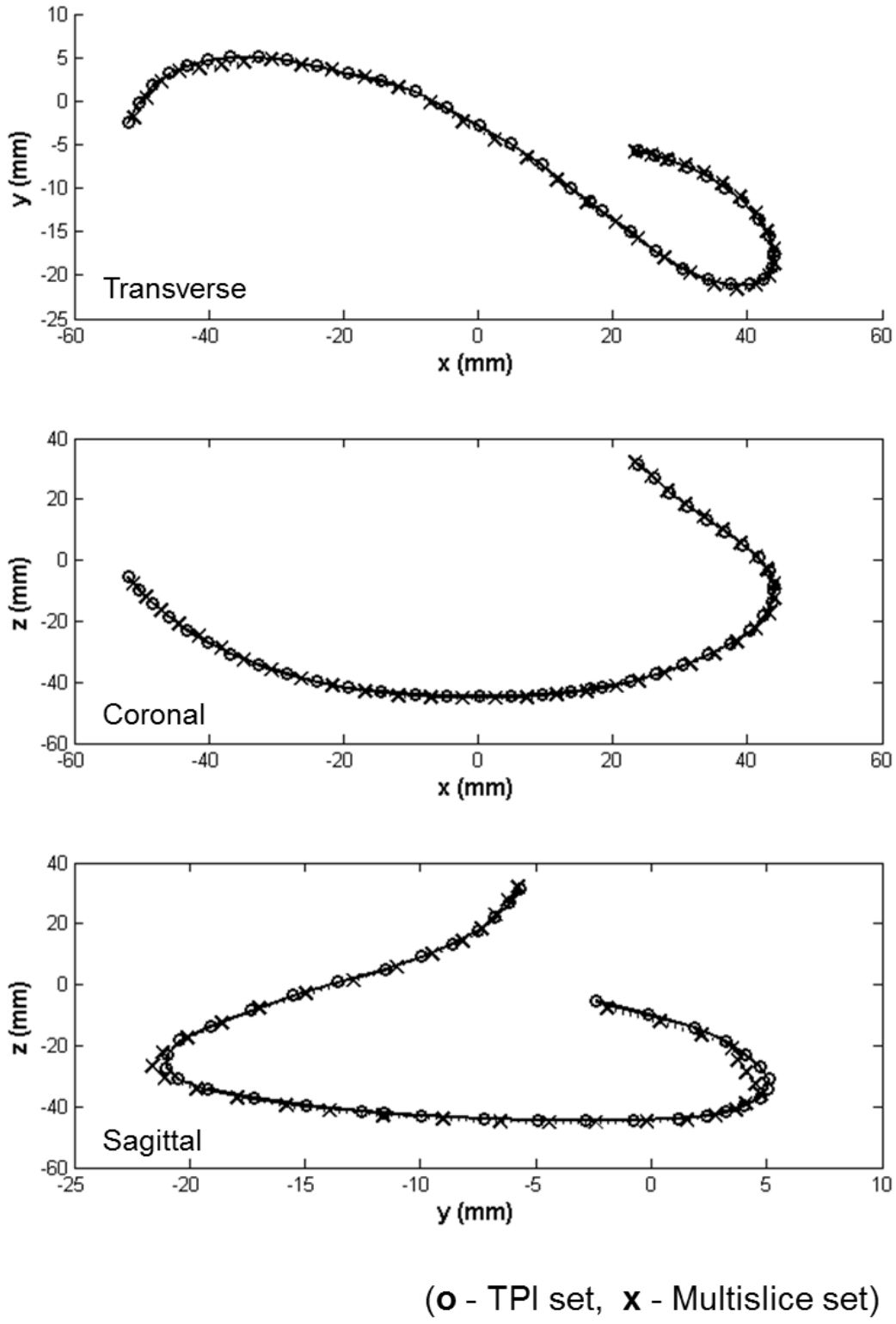

Figure 3.10 Comparison of the centerlines as projected onto the three orthogonal planes.

3.4 Discussion

This work introduces and describes proof-of-concept studies of an MRI method to image tubular structures from a set of three orthogonal 2D projections. The method is similar to biplane x-ray fluoroscopy. However, MRI offers certain benefits originating from the inherence to the modality and direct coregistration of the three projections. This is unlike the x-ray fluoroscopy which requires spatial transformations to correlate the spatial coordinates on the two projections and appropriate adjustment of the size of the structure to account for the different distances of the x-ray sources and detectors.

The feature of MRI for computer-controlled selection of oblique volumes can be used to collect the TPI with any desired orientation in space to better resolve complex structures. With the state-of-the-art scanners, dynamic adjustment of the acquisition parameters, including the gradient axis is possible. Thus, the scanner may be dynamically adjusted on-the-fly by the operator or by an automated scheme in between acquisitions each with different orientations of the TPI planes. An example has been shown before when a robot was controlling on-the-fly the MRI imaging plane [100].

The accuracy of 3D reconstruction of the imaged structures from the TPI depends on the accurate matching of the three MR projections. The reconstruction is determined primarily by the performance of the spatially encoding magnetic field gradients. Potential suboptimal gradient performance may result in mismatching of the encoding axis and the reconstructed object may be mismatched and distorted when compared to the actual structure. Shape distortion will also occur if the readout encoding axes are not perfectly

prescribed or the gradients do not perform as expected. Of course, those are spatial misregistration problems which can be encountered to any pulse sequence and depend on the performance of the hardware. Figure 3.11 shows 3D reconstructed models from two and three MR projection images. However, Fig. 3.11 (a-c) displays ghost structures in the 3D reconstructed images when compared to the 3D reconstructed model from three MR projection images in Fig. 3.11 (d).

Another aspect of the reconstruction is the coincidence of the excited volumes. The TPI pulse sequence can be susceptible to mismatch of the excitation volumes. This requires that the excitation frequency and the excitation bandwidths of the pulses be accurately prescribed to avoid excitation intensity gradients secondary to the pulse profiles. It should be mentioned that this problem can be eliminated by using non-slab selective excitation or if the slab selection gradients are along the same axis, e.g., X axis, so the excitation profiles of all pulses are identical.

A central aspect of the implemented TPI sequence is the suppression of the background signal which originates from all structures but the contrast enhanced one. Suppression is used for two interrelated reasons: to improve contrast and simplify the reconstruction. With non-selective or thick-slab excitation, signal is collected from a large volume and if not suppressed it can be substantial relative to the contrast enhanced structure. The importance of efficient background suppression in dynamic magnetic resonance angiography (MRA) for improved vessel-to-tissue contrast-to-noise ratio (CNR) with projection or thick-slab MRA has been demonstrated before [101, 102]. A direct consequence of the reduced contrast can be the virtual masking of the targeted structure precluding or making challenging its segmentation, and therefore reconstruction. In the

presented work, we used a short duration magnetization preparation to harvest the highest possible signal from the short T1 species (i.e., the contrast enhanced structure) while saturating the long T1 background.

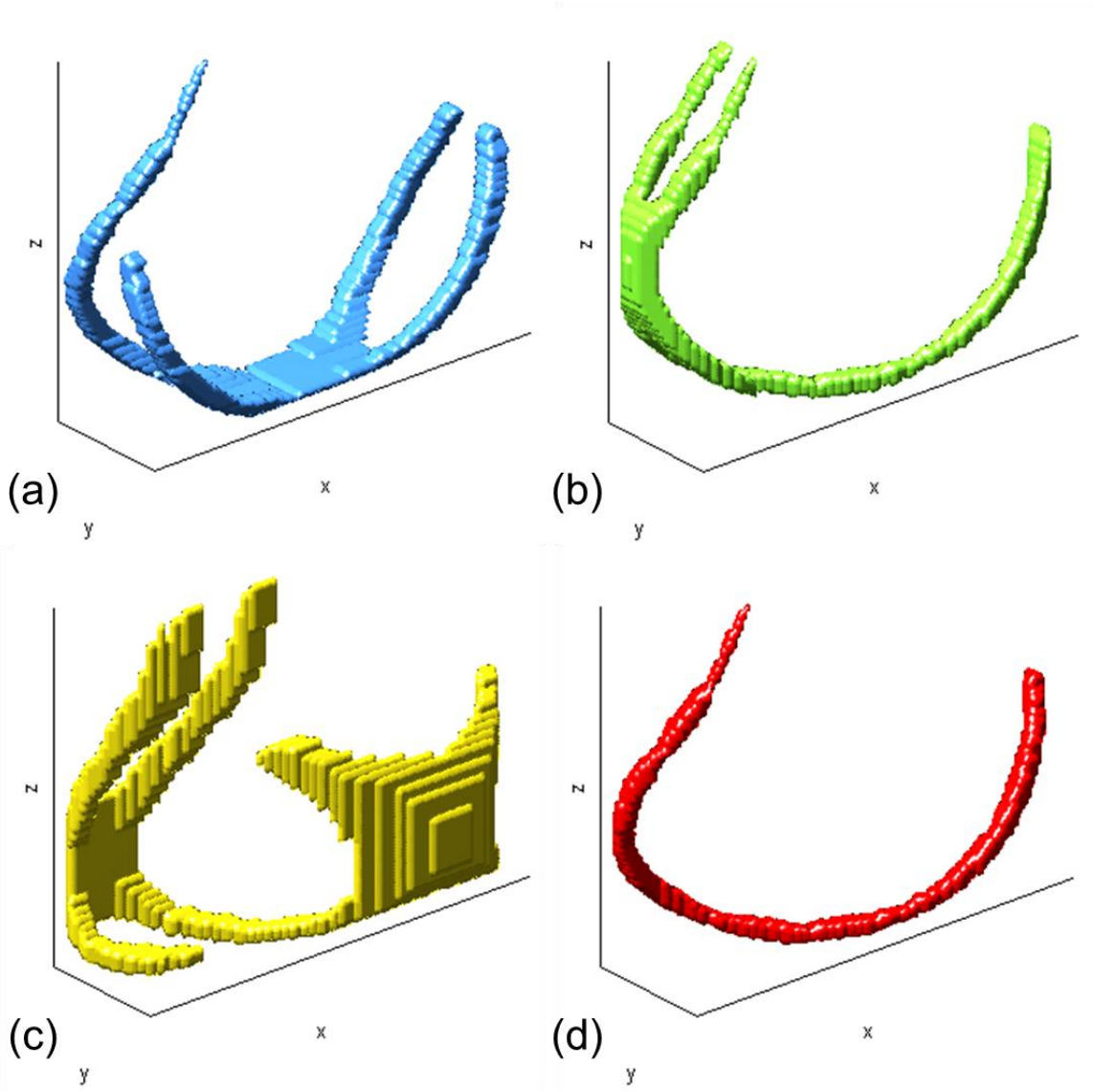

Figure 3.11 3D reconstructed models from: (a) coronal and sagittal, (b) transverse and coronal, (c) sagittal and transverse, and (d) coronal, sagittal and transverse.

Example applications of the TPI are the dynamic imaging of contrast enhanced vessels, and passive tracking and imaging of catheters, and other flexible or rigid interventional devices such as endoscopes equipped with contrast agent filled markers. The primary feature of the TPI acquisition is the volumetric imaging of a structure with the concurrent elimination of the background.

This work demonstrates the implementation of an acquisition scheme for volumetric imaging of contrast enhanced tubular structures with the simultaneous collection of three orthogonal MR projections. The tested TPI sequence provided spatial matching of the structure in the three MR projections, as benchmarked against a conventional multislice technique. A simple algorithm provided accurate 3D reconstruction of the object. Further development and evaluation is underway to implement faster TPI pulse sequences, develop reconstruction code for real-time online reconstruction (in C/C++) and accelerated visualization on a Graphics Processor Unit (GPU) for interactive 3D visualization on-the-fly. In addition, assessment of the method for reconstructing more complex structures followed by in vivo studies are warranted. Among other applications, TPI sequences can be used to visualize contrast enhanced catheters and vessels, as well as tubular MR-visible markers on interventional tools and manipulators.

The 3D tubular structure from the TPI set may have the potential shape limit of the Steinmetz solid [103, 104] which is formed by the intersection of three pairwise orthogonal cylinders/circles.

Figure 3.12 shows the intersection of three cylinders, also called a tricylinder. The volume of intersection from tricylinder can be computed in Equation 3.1.

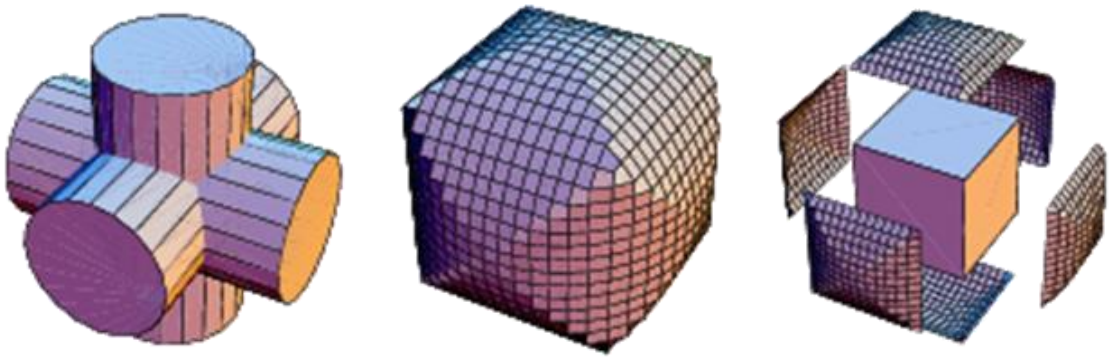

Figure 3.12 Models of tricylinder and its intersection volume [104].

$$V = \left(16 - \sqrt{128}\right) r^2 \tag{3.1}$$

However, centerline comparison of the TPI vs. multislice generated 3D structure shows significant advantages in regard to speed and accuracy. This study demonstrates the TPI acquisition scheme and 3D volumetric reconstruction of tubular structures such as catheters and blood vessels from the TPI set for MRI-guided interventions. In addition, we analyzed the accuracy of the position and orientation estimation of two 3D volume models reconstructed from the TPI set and from the multislice set.

Chapter 4

4 MR-Compatible Sensors and System Integration

4.1 MR-Compatible Optical Encoder

An optical encoder is a transducer or an electromechanical device that is able to measure position and motion for robot maneuvering. Common optical encoders consists of ferromagnetic substances and conductive wires. Commercially-available optical encoder (EM1 or EM2, US Digital, Vancouver, Washington) have been usually used to detect rotary or linear position for the MR-compatible robotic manipulators and the optical encoder is known to be MR-compatible. However, it is the potential which these optical encoders should require the shielded cable to prevent unwanted external signal noise

because the encoders operate with a 5 volt DC power supply and use connector pins to connect electrical or conductive wires. Also, imaging artifacts generated by the optical encoder during MR imaging may be produced at the magnetic isocenter [105, 106]. Fiber optic joystick which are fully passive and non-electrical devices was developed by Ben Krasnow [107]. Accordingly, development in general-purpose optical encoder have heightened the need for MRI comparability. In this section, we demonstrated the MR-compatible optical encoder for the feedback motion control of robotic manipulators.

4.1.1 Design and Implementation of MR-compatible Optical Encoder

Figure 4.1 and 4.2 illustrate the schematics of the MR-compatible optical encoder and the encoder circuit. Each encoder consists of two optical transmitters (HFBR-1414TZ, Avago Technologies, San Jose, California) containing an infrared emitter (820 nm) and two receivers (HFBR-2412TZ, Avago Technologies, San Jose, California) containing a photodetector. Each fiber cable (15 m long, a core size of 62.5 μm and a cladding diameter of 125 μm) terminated with ceramic ferrules (0.125 mm inner and 2.5 mm outer diameter) is connected to each transmitter and receiver. Figure 4.3 shows photograph of a custom-made MR-compatible optical encoder and the encoder circuit. Figure 4.3(b) shows that encoder holder, which is the same size as EM1 optical encoder, was first designed with a 3D modeling software (Solidworks, Computer Aided Technology, Inc., Buffalo Grove,

Illinois) and then manufactured on a rapid prototyping 3D printer (Prodigy Plus, Stratasys, Eden Prairie, Minnesota) using acrylonitrile butadiene styrene (ABS P400, a non-magnetic and non-conductive material) for MRI comparability. Two holes are drilled through an encoder holder to align the ceramic ferrules. Two transmitters are ON all the time, and two output waves (i.e., quadrature) from two receivers are 90 degrees out of phase. Ideally, output pulses from two receivers for each Channel A and Channel B should be on 50% of the time and off 50% of the time; however, the MR-compatible is not always on and off 50% because it depends on the distance of two holes for assembling four ceramic ferrules (i.e., two for Channel A and others for Channel B). These two square waves from two receivers are decoded to measure counts up/down and determine the direction of rotation/progress by the encoder circuit made of the microcontroller (Arduino UNO, www.arduino.cc).

Optical encoder holders are comprised of entirely nonmagnetic, nonmetallic and biocompatible material that are ceramic ferrules accommodating optical fibers and acrylonitrile butadiene styrene for MRI compatibility. Ceramic (zirconia) materials were presented that enables considerably high quality of MR images within the MR environment without any severe susceptibility artifacts and distortions [108-113]. ABS materials and optical fibers we used were also studied as fully MR-compatible substances. During MRI-guided interventional procedures, this MR-compatible optical encoders can be located inside the bore of MR scanner and optical fiber cables should be passed through a penetration panel shielded from RF waves on the wall of the scanner room.

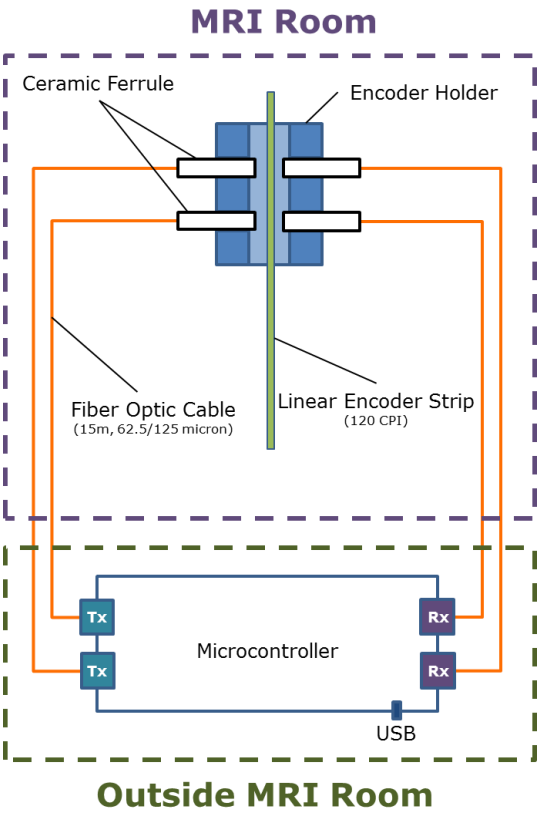

Figure 4.1 Schematics of a custom-made MR-compatible optical encoder and the encoder circuit.

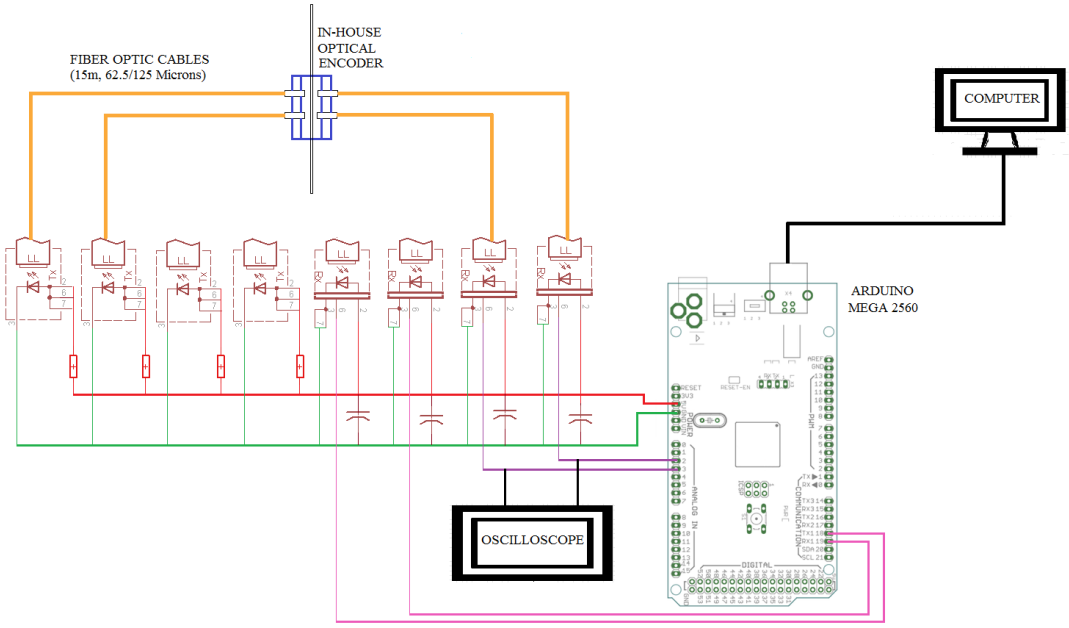

Figure 4.2 Circuit diagram of MR-compatible optical encoder.

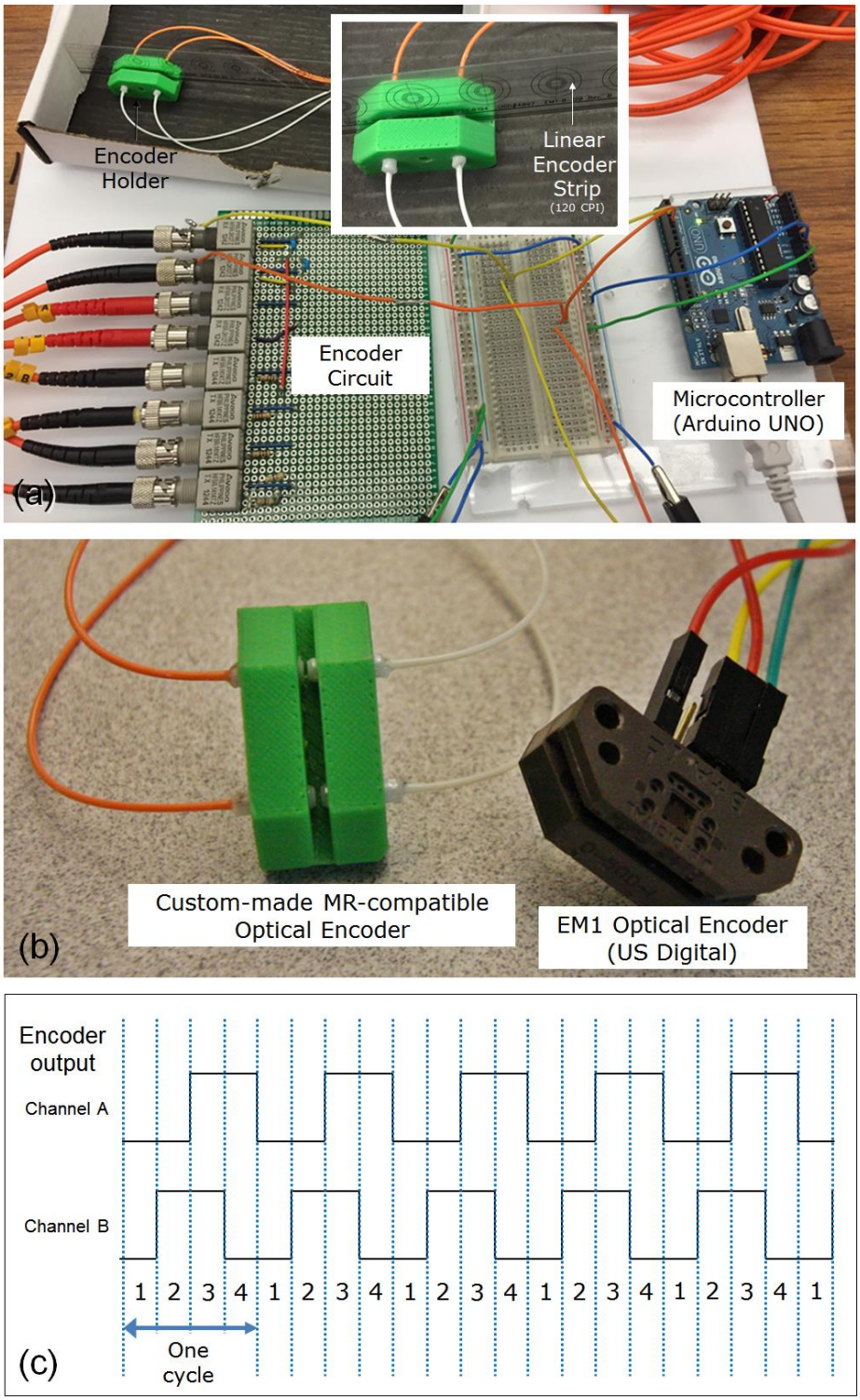

Figure 4.3 (a) Photograph and close-up of a custom-made MR-compatible optical encoder and the encoder circuit. (b) Comparison of a custom-made MR-compatible optical encoder and a commercial optical encoder. (c) Two square waves (channel A and B) for counting cycles.

4.1.2 Accuracy Analysis of MR-compatible Optical Encoder

Accuracy of the MR-compatible optical encoder was analyzed compared to the EM1 optical encoder using our custom-made one DoF linear translation stage shown in Figure 4.4 that moves forward and backward actuated by lead screw driven stepper motor (NEMA 23, Anaheim Automation, Inc., Anaheim, CA, USA) and stepper motor driver (SMCI47-S-2, Nanotec Electronic U.S. Inc., Stoneham, MA, USA). Rotating the lead screw by actuating the stepper motor translates a load that is attached to the anti-backlash lead nut block. The optical encoders were fixed to the bottom of the linear stage and the linear encoder strip was attached to the maneuvering load. The thread pitch of the lead screw, i.e., distance between corresponding points on one thread and the next, is 2 mm and its lead screw OD is 8 mm. For the accuracy analysis, a couple of different resolutions of linear encoder strips, i.e., 120 cycles per inch (CPI), 125 CPI, 127 CPI, 200 CPI, and 500 CPI) were used. The MR-compatible optical encoder was worked thoroughly without any missing ticks. However, it did not work properly with only 500 CPI strip because a core size (62.5 μm) of the optical fiber is larger than the pitch, i.e., the length of light pattern, of the encoder strip (approximately 25.4 μm); therefore, transmitter and receiver were not both transmitted and absorbed infrared light (820 nm) sufficiently for the quadrature decoding.

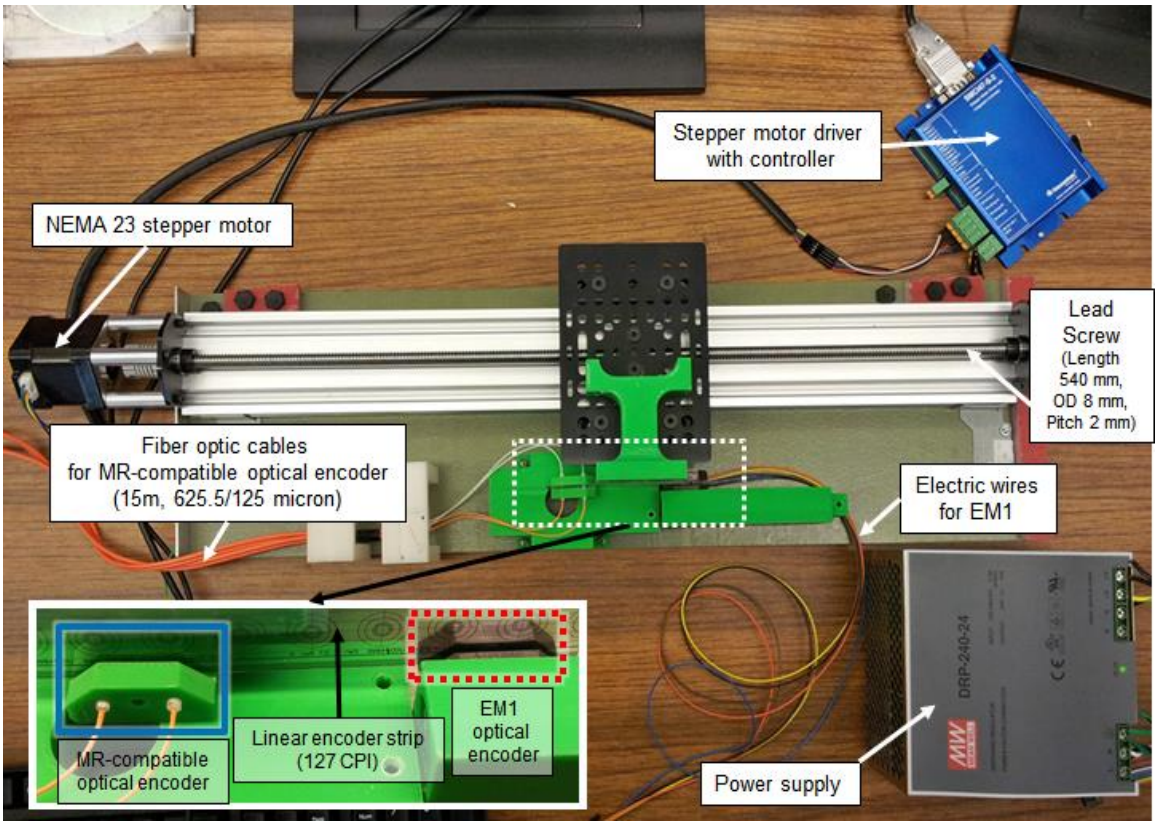

Figure 4.4 Photograph and close-up of the one DoF linear translation stage attached to a custom-made MR-compatible optical encoder (blue sold square) and EM1 optical encoder (red dotted square).

Figure 4.5 shows the quadrature plots generated from two receivers of the MR-compatible optical encoder. All quadrature plots were measured by the oscilloscope (TDS2001C, Tektronix, Inc., Beaverton, OR, USA). The linear translation stage was actuated under a variety of different speed translation maneuvering with 127 CPI encoder strip. The translation speed ranged from 10 Hz to 2000 Hz and missing ticks were not found.

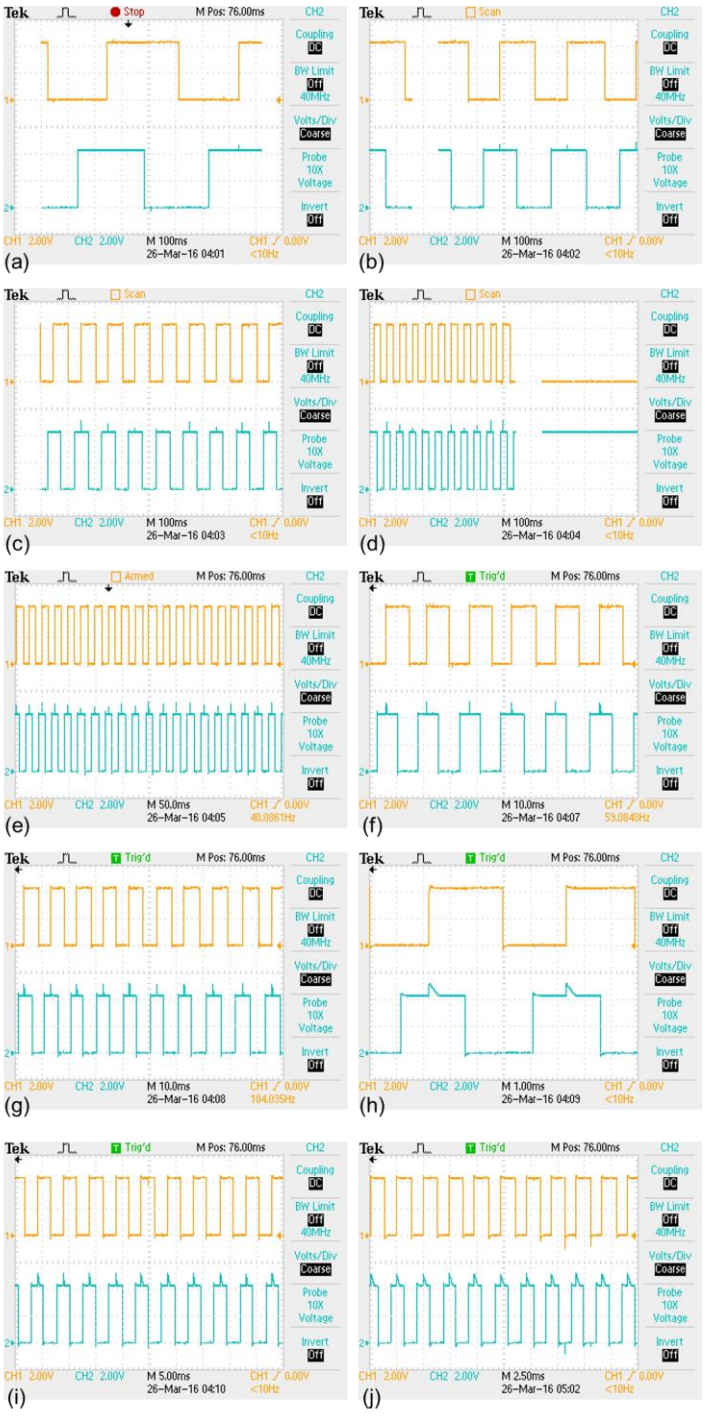

Figure 4.5 Quadrature plots under different speed of translation: (a) 10 Hz, (b) 20 Hz, (c) 50 Hz, (d) 100 Hz, (e) 200 Hz, (f) 300 Hz, (g) 500 Hz, (h, i) 1000 Hz, and (j) 2000 Hz.

4.2 MRS/LIF Dual-Modality Biosensor

4.2.1 Introduction

Multimodality biosensing is emerging as a valuable approach for characterizing the pathophysiology of tissue. Optical fluorescence and MR spectroscopies (MRS) may offer complementary information about endogenous or exogenous fluorophores and metabolites, respectively. While depth penetration is an issue for optical tomography, endoscopic approaches position the probe near the region of interest, therefore reducing this limitation. Recently the combination of light-induced fluorescence (LIF) and MRS was demonstrated [114]. We describe a forward looking optical/NMR probe for loco-regional in situ biosensing for collecting LIF and ^{1}H MRS from the same region. This dual modality probe was mounted on an MR compatible manipulator to (I) co-register MR image, LIF and MR ^{1}H spectra, and (II) mechanically scan to assess the spatial distribution of fluorophores (from LIF) and metabolite (from MRS).

Chapter 4.2 is reproduced based primarily upon "MR compatible endoscope for assessing the spatial distribution of co-registered optical and ^{1}H signals" [115], and "Manipulator-mounted optical NMR dual-modality probe for multimodality scanning in MR guided and robot-assisted interventions", DOI: 10.1016/j.ejmp.2014.07.120 [116] performed in collaboration with Ahmet E. Sonmez, Andrew G. Webb, Mahmut Unan, Robert D. Darrow, Ileana Hancu, R. Jason Stafford, Ioannis Seimenis, Eftychios Christoforou, and Nikolaos V. Tsekos. Copyright Physica Medica: European Journal of Medical Physics (2014) and ISMRM (2014).

4.2.2 Method

Figure 4.6 shows the MRS/LIF dual-modality probe composed of: (a) a 1.0 mm circular RF microcoil and a three-fiber endoscopic sensor [114], and (b) a 1.25 mm OD 7-fiber optical sensor and an RF coil (OD 2.3 mm, length 2.2 mm, five turns 26 AWG) [115]. Six fibers were connected to an LED (filtered at 450 nm) for high power light emission and one fiber was used for reception of light connected to an optical spectrometer (USB 2000+, Ocean Optics, Inc., Dunedin, FL).

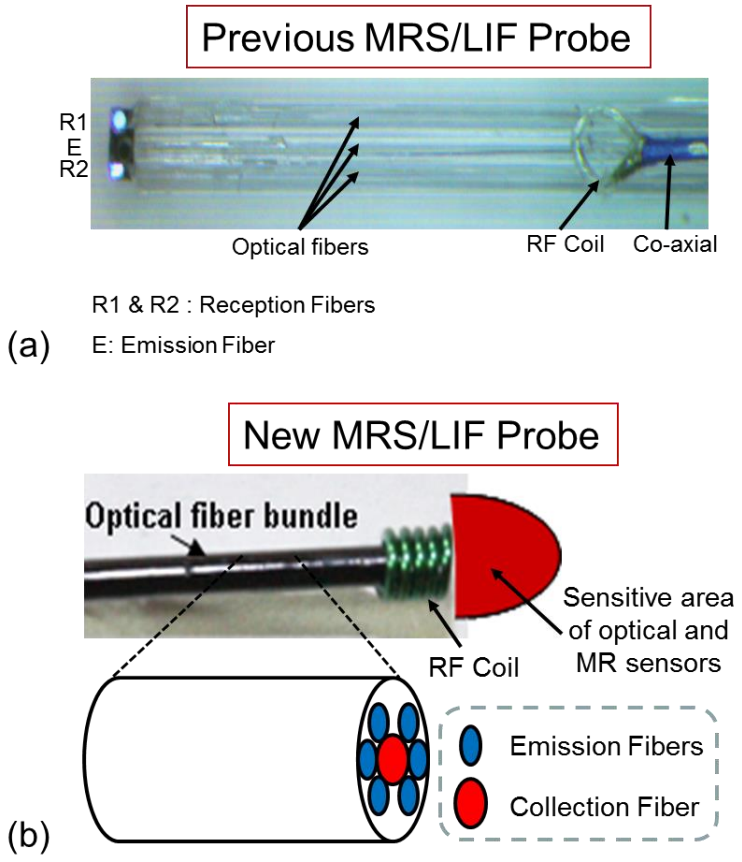

Figure 4.6 Photograph of (a) previous and (b) new MRS/LIF dual-modality probes.

For 1D spatial scanning, the probe was pulsed by an in-house shielded PiezoWalk motor (N-310 NEXACT® OEM Miniature Linear Motor, Physik Instrumente (PI) GmbH & Co. KG., Karlsruhe, Germany). This probe was tested on three-compartment phantoms with characteristic optical and ^{1}H signals: (I) comp-1 water-based gelatin (^{1}H at 4.9 ppm) and fluorescein for LIF, (II) comp-2: oil-based gelatin (^{1}H peak at 1.4 ppm) and no fluorophore, (III) comp-3: water-based gelatin with choline (^{1}H at 3.3 ppm) and fluorescein/ rhodamine-B for LIF. The manipulator, and thus the LIF/MR probe, was first registered to the MR scanner from images collected with the microcoil as a Tx/Rx fiducial marker. Scanning entailed the steps: (1) motion of the sensor to a new position, (2) trigger MR to collect a free induction decay (FID) (flip angle = 20°, 5000 Hz and number of points = 2048), (3) trigger optical spectrometer for LIF spectra (5 s collection). The spectra were then ordered based on the spatial position of the probe from the registration and the optical encoder signals, and presented as contour plots of the spectra with the vertical axis being the axis of scanning (for clarity the water proton signal at 4.9 ppm was omitted). In addition, Figure 4.7 shows that robot-assisted dual-modality probe inserts into the phantom with assistance of a needle. After that, the needle is withdrawn from the phantom. This leaves the dual-modality probe inside the phantom. After that, the simultaneous dual-modality data begins collecting. It is step by step process. First, the probe collects dual-modality data in its current location. Then, the probe is withdrawn 1 mm. And, the probe collects same data from new location. This process is repeated until the probe is removed fully.

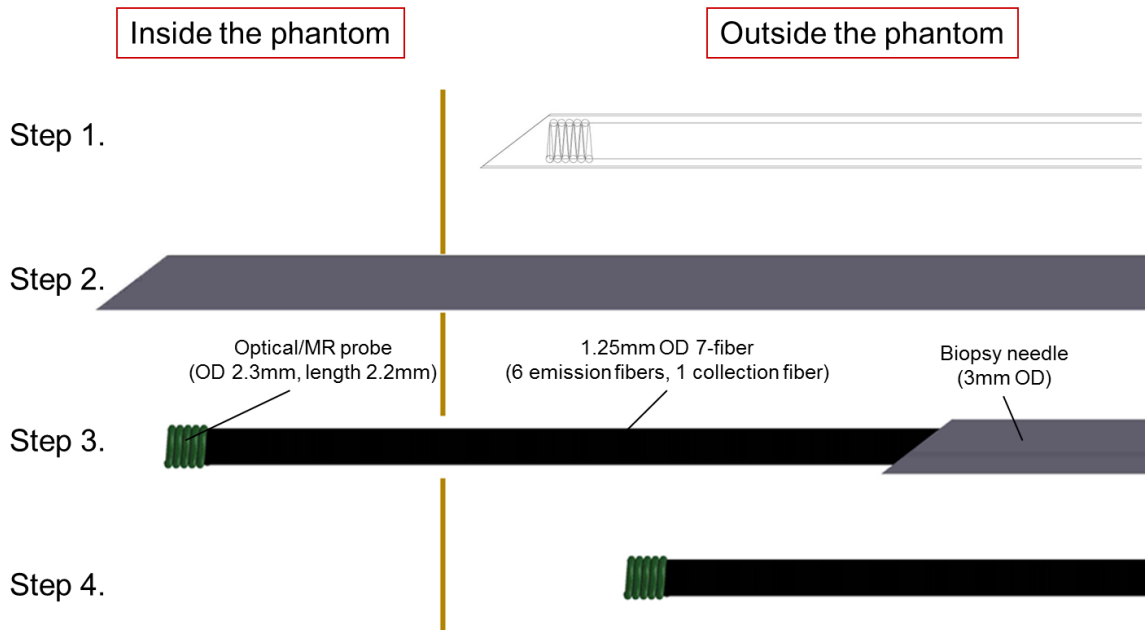

Figure 4.7 Experiment process of robot-assisted dual-modality probe.

4.2.3 Results

Figure 4.8 shows spectro-spatial contour plots for both modalities clearly showing the two boundaries between the three compartments. LIF spectra show fluorescein in comp-1, Rhodamine-B/fluorescein in comp-3, and lack of any signal in comp-2. The MRS exhibits identical patterns: comp-1 has only water signal at (not shown), comp-2 has oil signal (peak at 1.4 ppm), and comp-3 has choline (peak at 3.3 ppm). Spatial matching was within the LIF/MRS mechanical resolution of 0.5 mm: the boundaries from MRI were calculated at -9.2 and +3.3 mm, from LIF spectro-spatial plot at -8.8 and +3.6 mm and from MRS at -8.2 and +3.7 mm.

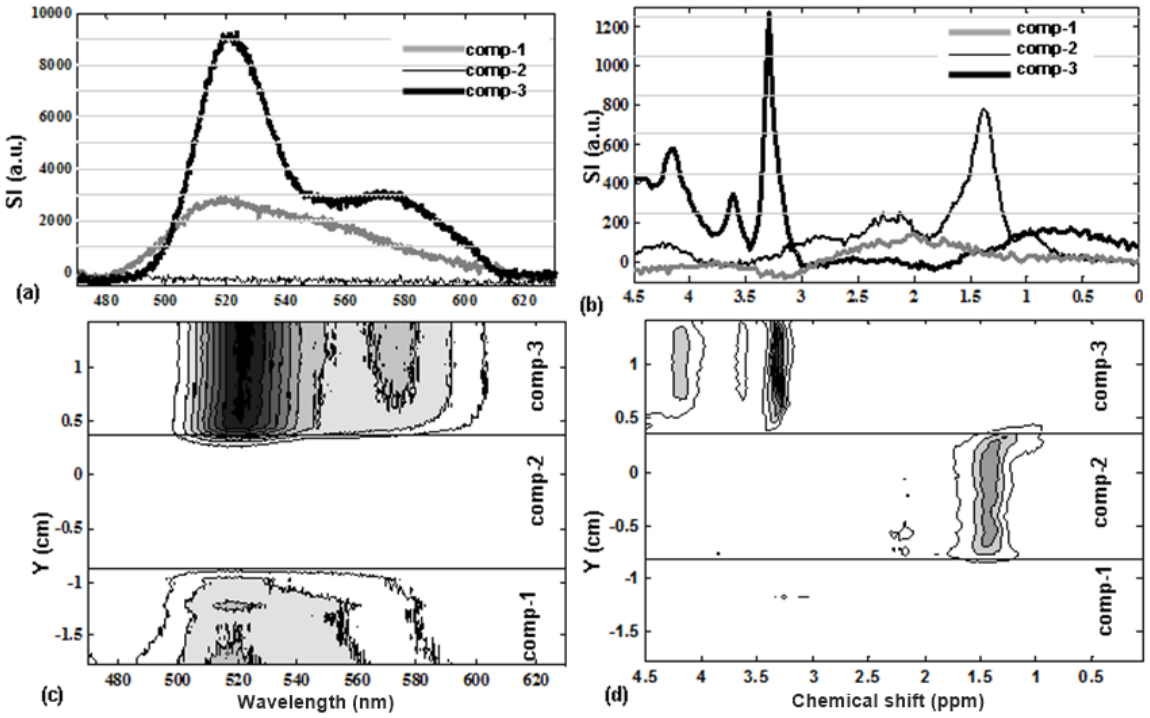

Figure 4.8 (a) LIF and (b) 1H MR spectra from each compartment. (c, d) contour plots of (c) LIF and (d) 1H spectra collected along the Y MR scanner axis. Horizontal lines in (c, d) delineate the boundaries of the compartments.

As reported in the Table 4.1, the presence and operation of the probe and manipulator had no effect on the SNR of GRE images and ^{1}H spectra.

Table 4.1 SNR of MR spectra and images at various motor and encoder statuses.

Motor Status	Spectra	Images
Unpowered	12023 ± 487	72.96 ± 2.79
Unpowered	11956 ± 570	77.68 ± 3.80
Powered (no motion)	12294 ± 530	73.34 ± 2.80
Powered (motion)	12188 ± 648	73.00 ± 2.81

4.2.4 Discussion and Conclusion

The use of MR and optical sensors may have impact in improving diagnosis in situ, as well as in performing basic research in vivo. For instance, it may enhance the detection of tumor margins and even used to guide biopsies [117]. Compared to a prior work that reports LIF/MRS [114] (A) our probe has spatially matched optical and MR profiles (without post-processing [114]) and (B) the side-firing probe scans via an NMR tube that is inappropriate for in vivo and clinical studies [114]. Clinically, the herein described probe can be operated the same way as a standard clinical confocal endoscope (i.e. placed in the scanned area and pulled back [118] or it can be directly mounted on the end-effector distal end.) Currently, we investigate other microcoil shapes. In addition, we study the 3D spatial matching of the LIF and MR sensors with simulations (LIF profile with Monte Carlo and coil with Biot-Savart). This type of sensor can be modified, e.g., for optical conference tomography (OCT) and with coils for phosphorous (^{31}P) or sodium (^{23}Na) MRS.

A forward looking MR compatible optical/MR probe for assessing the spatial distribution of co-registered optical and ^{1}H signal sources using a pull mechanical scan is described and tested. The use of MR and optical sensors can have impact in improving diagnosis in situ, as well as in performing basic research in vivo. For instance, it may enhance the detection of tumor margins and even used to guide biopsies. We describe a forward-looking MR compatible optical/MR probe for assessing the spatial distribution of co-registered optical and ^{1}H signal sources using a pull mechanical scan.

4.3 MR-Compatible Snake-like Surgical Manipulator

In the field of robot-assisted MIS, dexterous manipulation is a crucial methodology to solve the issue of inadequate DoFs of the conventional interventional tools. We have designed and developed the novel MR-compatible snake-like surgical manipulator for the MRI-guided and robot-assisted interventions.

4.3.1 Selected Existing Snake-like Surgical Robots

Some snake-like manipulations for surgeries were developed previously in the research field of robot-assisted MIS. Many snake-like manipulators for surgeries and interventions used wire- or tendon-driven mechanisms for actuating all the joints for enhancing flexibility and surgeon's dexterity.

The steerable arthroscope was developed by Dario et al. [119]. This mechatronic arthroscope is steerable and a rigid cylinder with an OD of 4 mm and a total length of 350 mm. The 25 mm long distal section of the arthroscope can be bent 0 to 110 degrees. This can provide more than 0.1 N.

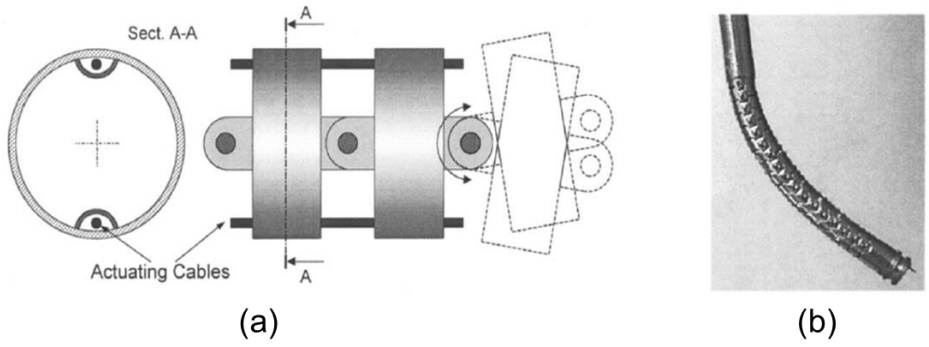

Figure 4.9 (a) Design and (b) prototype of steerable arthroscope [119].

A tendon-based multi-spherical joint design for an endoscopic tool and flexible laparoscopic extenders actuated by tendon wires was developed by Faraz et al. [120, 121]. The multi-spherical joints can be actuated remotely through wires.

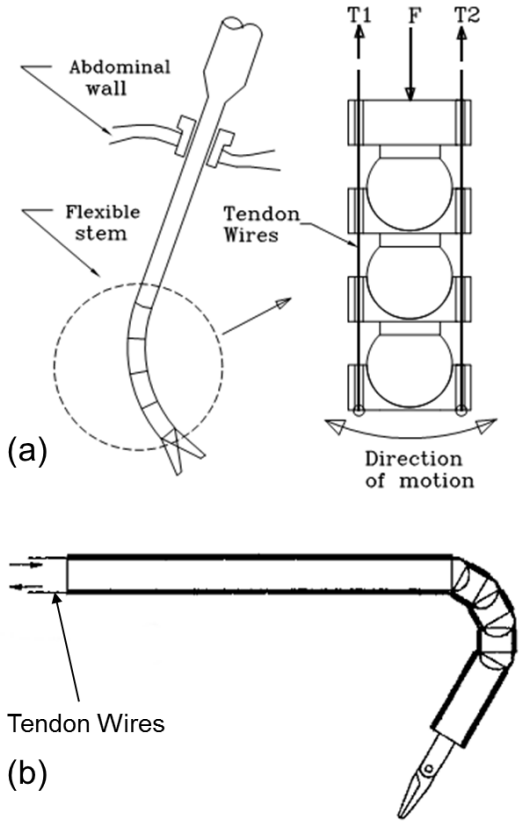

Figure 4.10 (a) An endoscopic tool [121]. (b) A flexible laparoscopic extenders [120].

The Distal Dexterity Units (DDU) approach was described and developed by Simaan et al. [122]. This unit employs a multi-backbone snake-like mechanism. A first built prototype of the snake-like unit of the DDU is shown in Figure 4.11 (b). The length of the DDU is 28 mm and its OD is 4.2 mm. It can be bent ±90 degrees in any direction and provides more than 1 N at its tip.

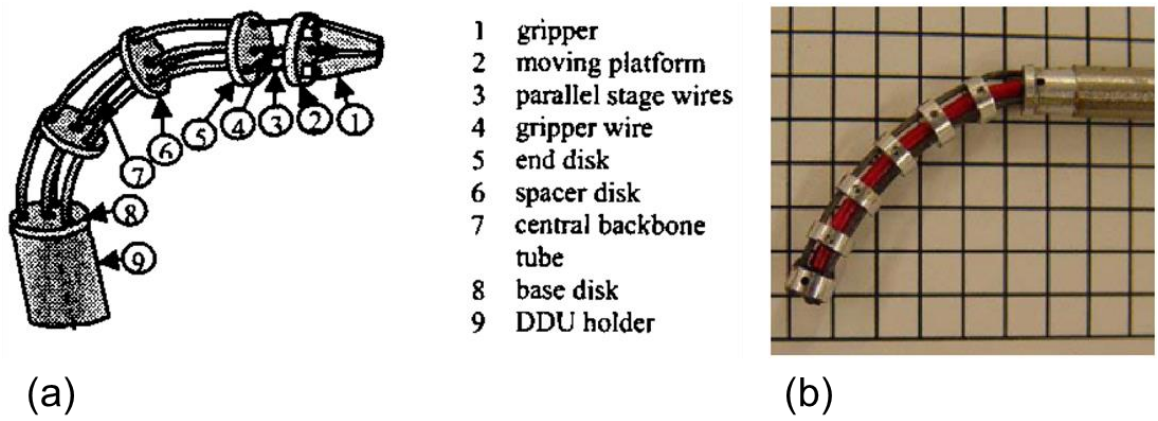

Figure 4.11 (a) The DDU using a multi-backbone snake-like robot. (b) 4.2 mm diameter prototype [122].

Peirs et al. [123] developed two prototypes of flexible endoscopic NiTi bending tubes. A first prototype of the flexible tube is made from a superelastic NiTi tube (OD 4.7 mm and ID 3.9 mm). The first prototype can be bent ±96 degrees. A second prototype is made from a NiTi rod (OD 4.9 mm and a hole of 3.5 mm diameter). Two times twelve pairs of joints for a second prototype are required to bend ±90 degrees.

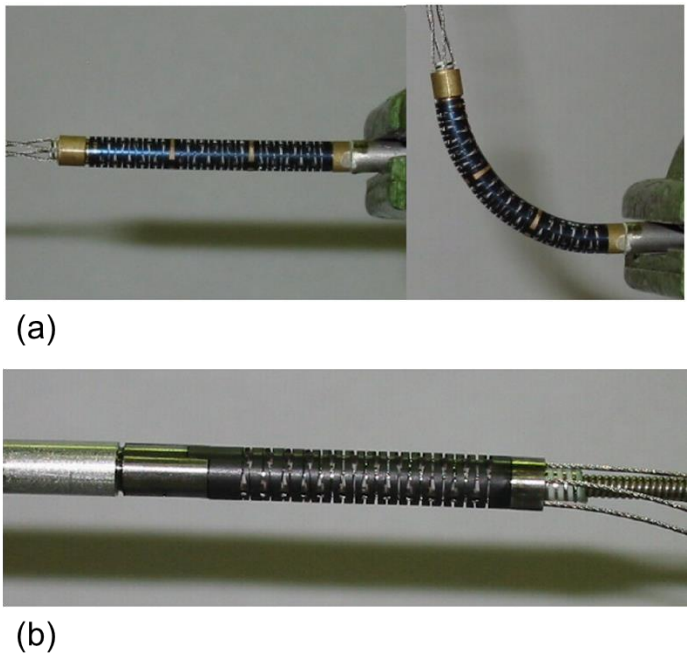

Figure 4.12 (a) A first prototype of a flexible endoscopic NiTi tube and (b) a second prototype [123].

A highly articulated robotic surgical system (CardioARM) was developed by Ota et al. for minimally invasive intrapericardial therapeutic delivery [124-126]. The CardioARM is composed of 50 rigid cylindrical links serially connected by four cables (one concentric cable and three directional cables).

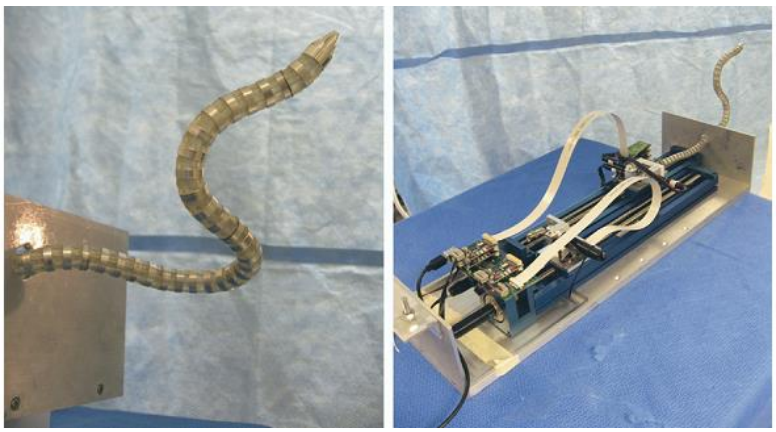

Figure 4.13 Photograph of highly articulated robotic surgical system (CardioARM) [126].

Harada et al. [127] developed a prototype of the micro manipulator actuated by ultrasonic motors for intrauterine fetal surgery in an Open MRI. The bending mechanism is composed of cylindrical parts with four holes for the directional wires and spheres with a central hole. Its OD is 2.4 mm and it can be bent 90 degrees in any direction.

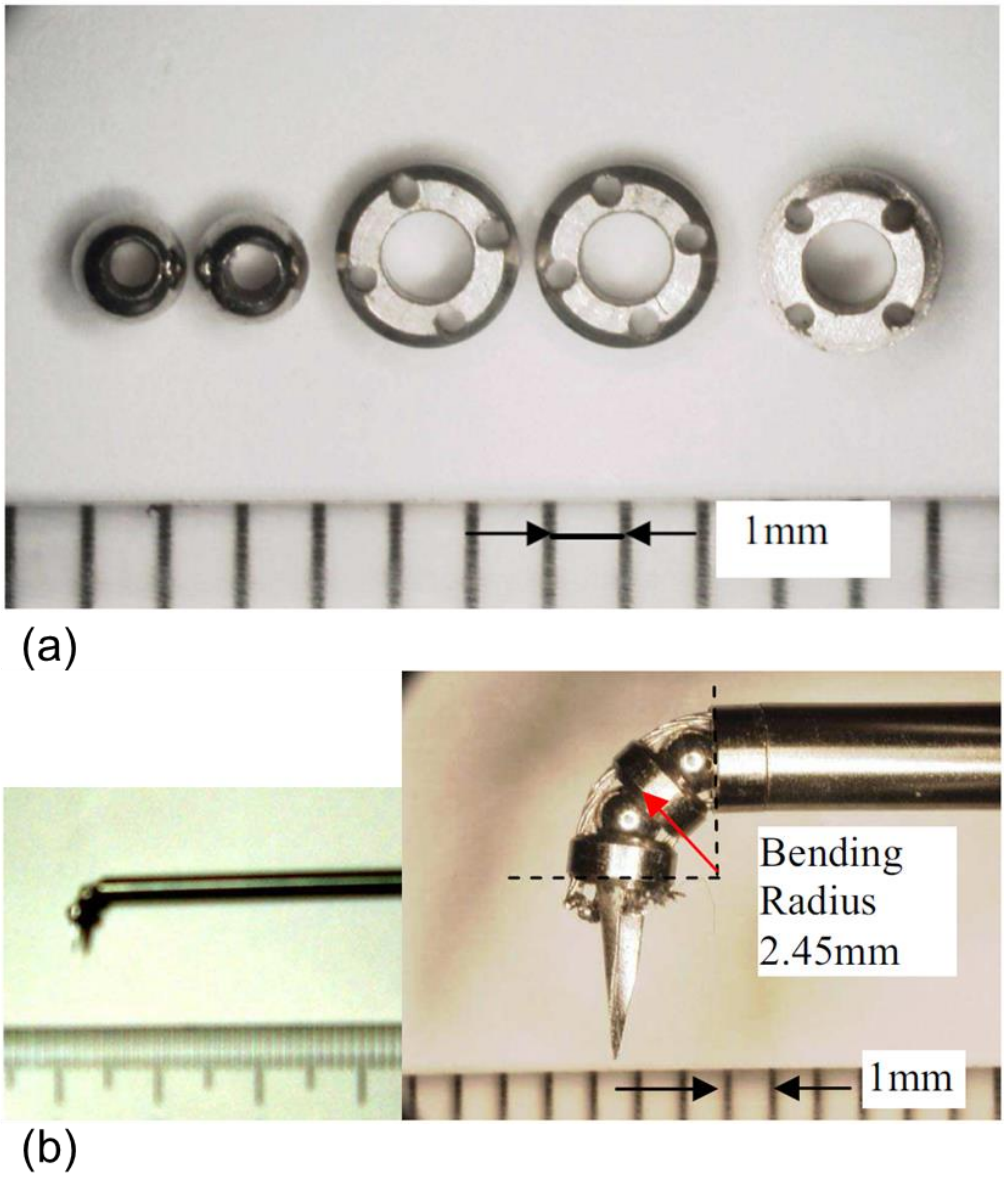

Figure 4.14 (a) Parts of the micro manipulator. (b) Photograph of the manipulator [127]**.**

Haraguchi et al. [128] developed a prototype of pneumatically-driven forceps manipulator using flexible joints for dexterity. Its OD is 10 mm and its bendable length is 22 mm. The overall length including the actuating part is 450 mm. Bending ranged is from -60 to 60 degrees and force estimation error was up to 0.2 N.

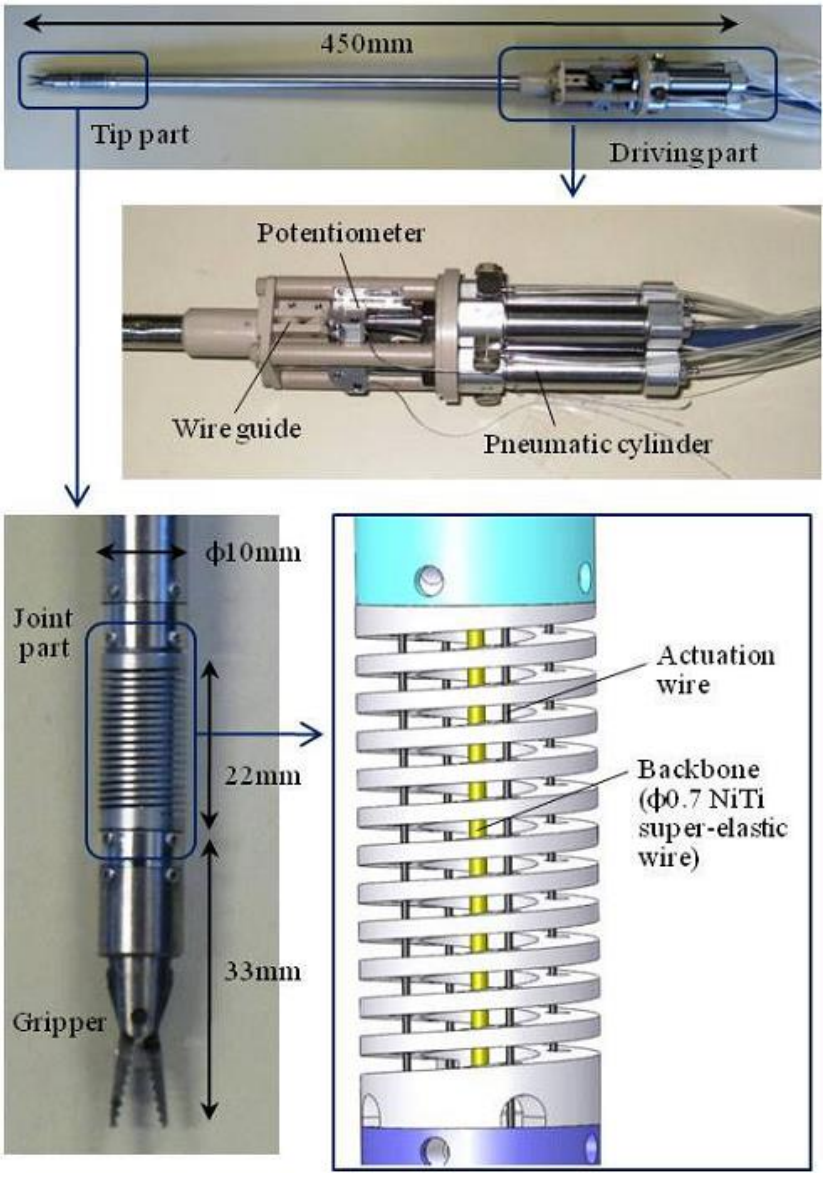

Figure 4.15 Photograph and schematic of the forceps manipulator [128].

Seow et al. [129] developed an articulated manipulator with multiple instruments for natural orifice endoscopic transluminal endoscopic surgery. The OD is 14 mm and the length of a single linkage piece is 32.5 mm.

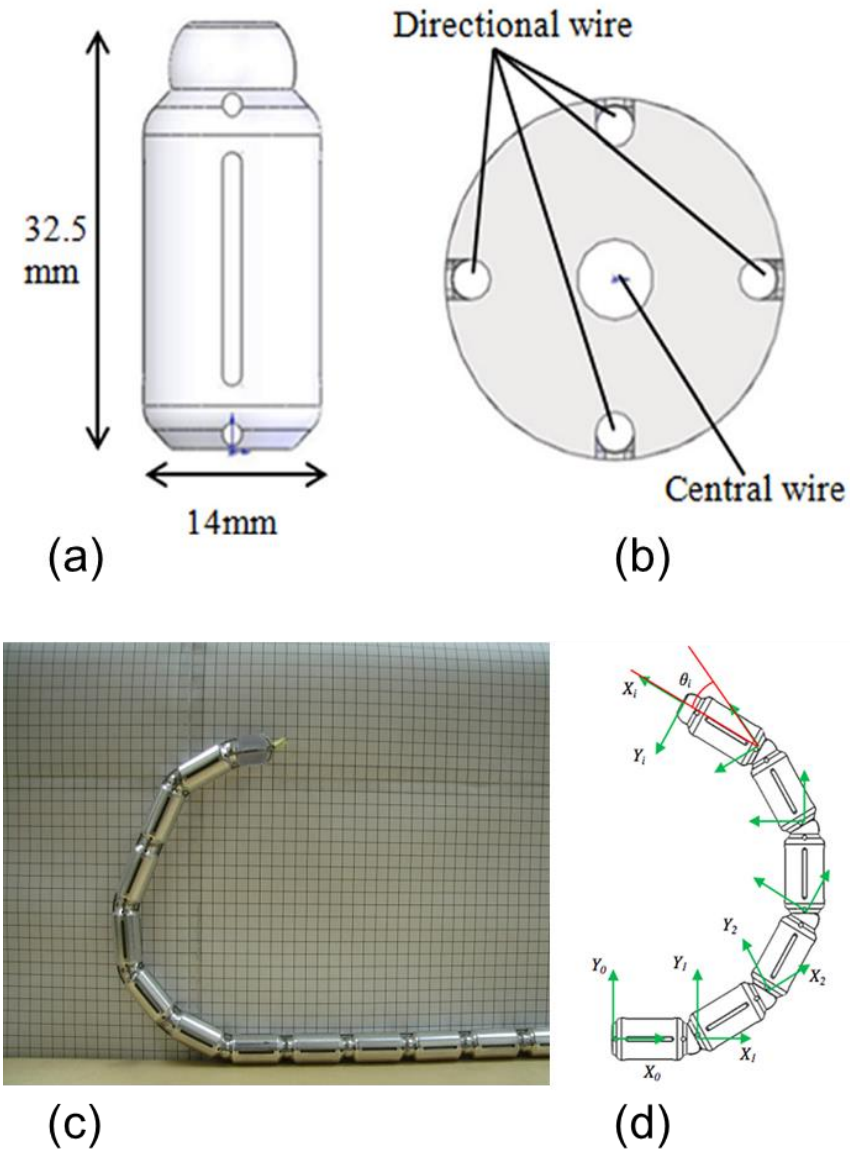

Figure 4.16 A single linkage piece (a) front view, (b) cross section. (c) Photograph of articulated manipulator. (d) Reference frame for Denavit-Hartenberg method [129].

The Endo-Periscope, developed by Breedveld et al. [130], is a bending segment for the steerable endoscope. The first prototype of 15 mm OD can be bent up to 180 degrees. The diameter of the instrument is reduced to 2.5 mm.

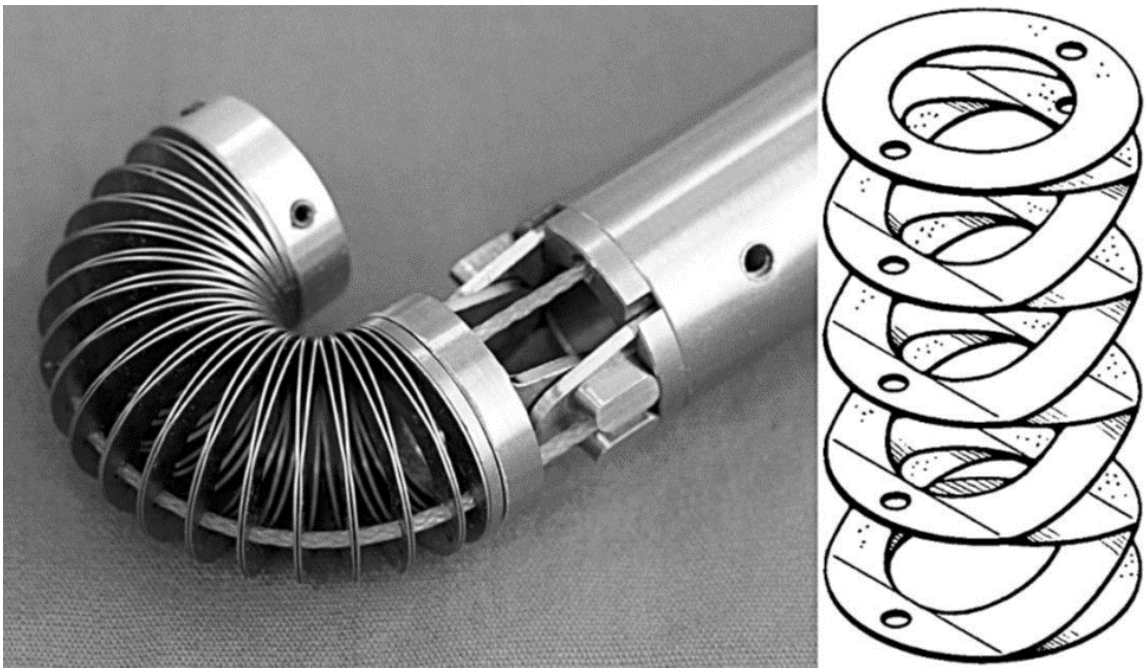

Figure 4.17 Steerable tip and ring-spring of the Endo-Periscope [130].

4.3.2 Design and implementation of MR-compatible dexterous manipulator

The field of dexterous manipulation is rapidly evolving to overcome limited flexibility and restricted workspace inside the human body for the robot-assisted interventions. In order for higher flexibility and accessibility in the patient's body and the MRI scanner, I have designed the MR-compatible dexterous manipulator for the MRI-

guided and robot-assisted interventions. A 3D modeling software (Solidworks) was used for 3D solid modeling to simulate dexterous manipulations and kinematics to figure out the maneuvering details.

Figure 4.18 shows 3D models of a single distal joint and MR-compatible articulated robotic probe. Its OD is 9 mm and the length of single dexterous joint is 12 mm. The length of the bendable part is 60 mm and the overall length of the MR-compatible dexterous manipulator is 270 mm including of the length of the base.

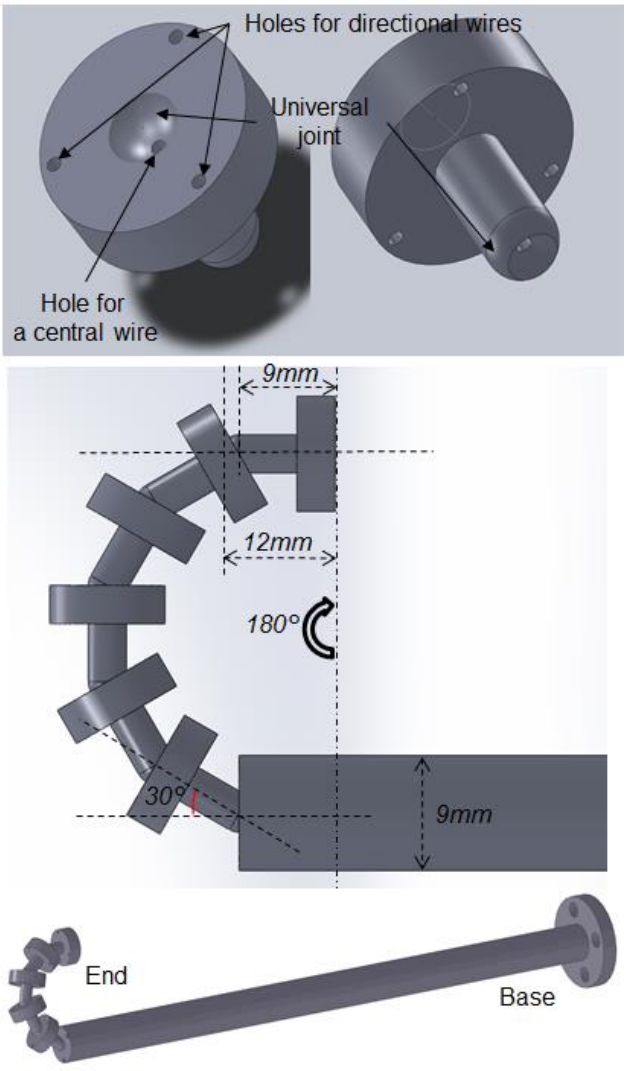

Figure 4.18 3D models of a single distal joint and MR-compatible articulated robotic probe.

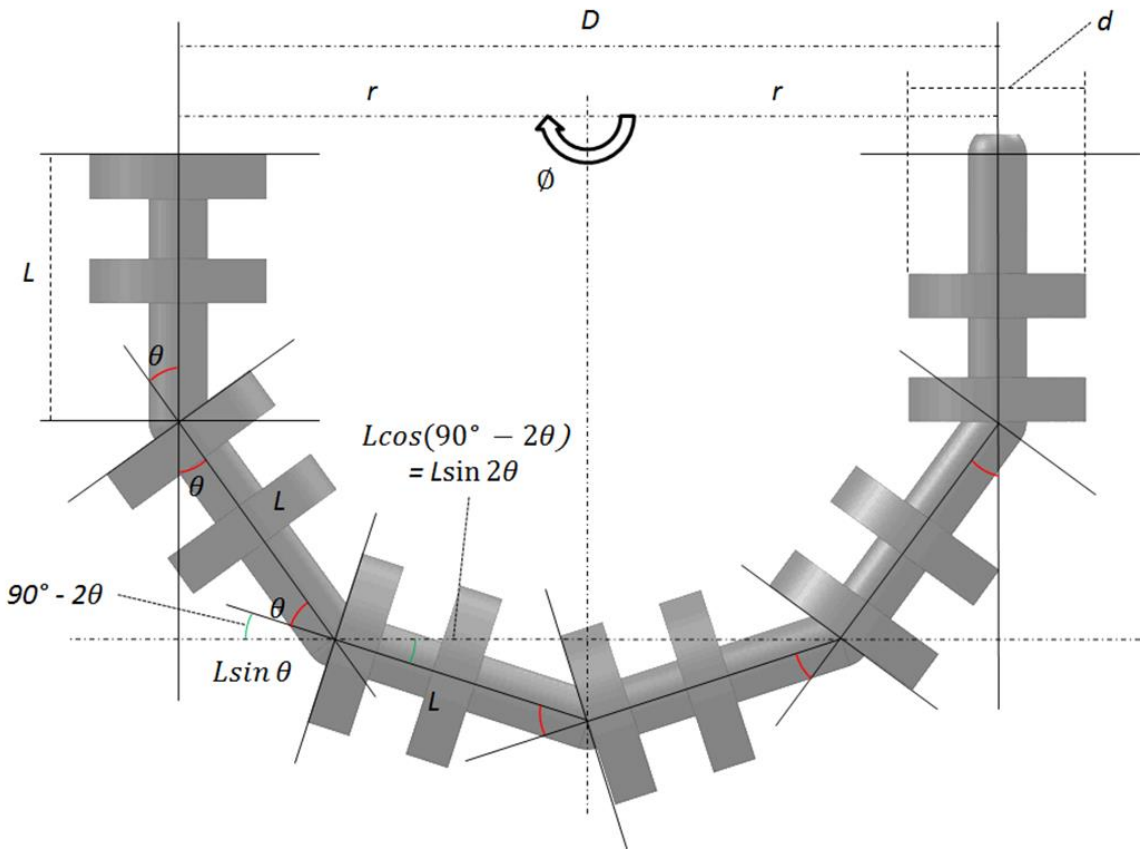

Figure 4.19 Calculation of bending angle and diameter of the MR-compatible dexterous manipulator.

Figure 4.19 demonstrates calculation of bending angle and diameter of the MR-compatible dexterous manipulator when the bendable tip is bent to 180 degree. The bending angle and diameter can be calculated with the following equations.

$$\emptyset = N * \theta \tag{4.1}$$

$$D = 2r, r = L\sin\theta + L\sin 2\theta \tag{4.2}$$

Figure 4.20 displays the prototype of MR-compatible dexterous manipulator, actuator and motor driver. The MR-compatible dexterous manipulator was physically prototyped using a 3D modeling printer (Prodigy Plus model, Stratasys, Eden Prairie, Minnesota) of non-magnetic and non-conductive ABS material. The wire-actuated universal joint mechanism are used for higher flexibility and workspace. In the actuation system presented herein I have used three standard NEMA 11 motors with rotary optical encoders (Anaheim Automation, Anaheim, CA) and stepper motor drivers (G250X, GekoDrive, INC., Tustin, CA). The MR-compatible dexterous manipulator presented herein can be bent ±180 degrees in any directions. All dexterous units are connected via the central wire (a NiTi superelastic cable) and three directional wires (0.45 mm diameter fishing lines) were used for actuating this dexterous manipulator.

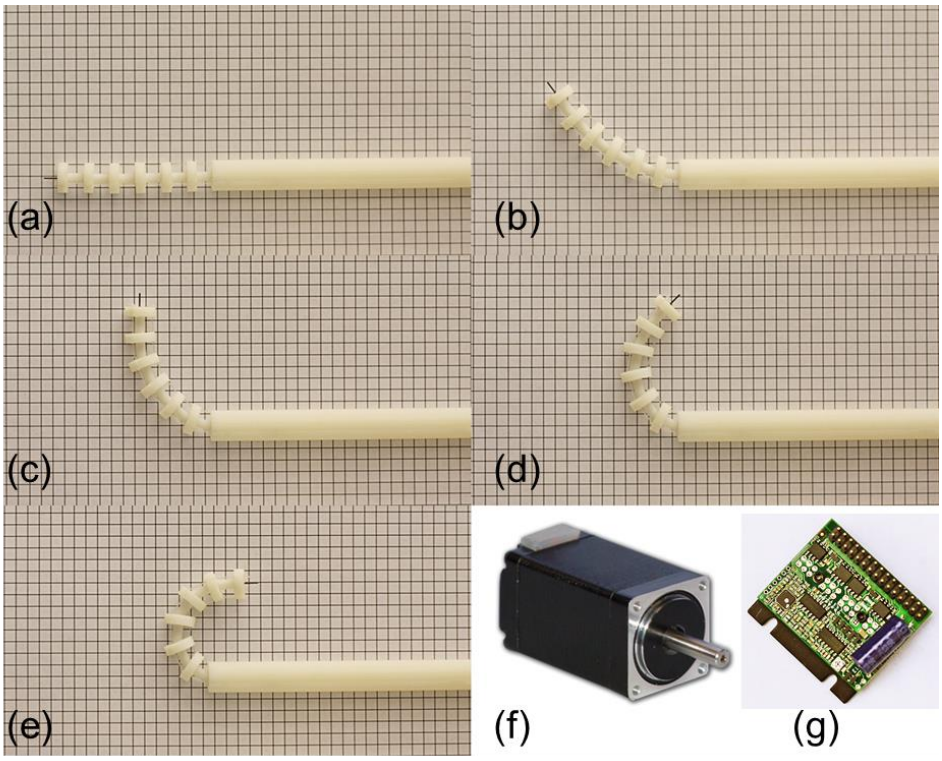

Figure 4.20 Photograph of MR compatible dexterous manipulator (a-e), stepper motor (f), and motor driver (g).

4.4 Sensors and System Integration

Each sensor and system used herein provides advantages individually. If they are integrated together, it will be a key technique for the MRI-guided and robot-assisted interventions. In this work, I have designed to integrate optically detunable MR-visible markers, the manipulator and marker control system, the dual MRS/LIF biosensor and the MR compatible dexterous manipulator.

Figure 4.21 and 4.22 show the 3D model of a single distal piece of integrated sensors and system for the MRI-guided and robot-assisted interventions. Its OD is 9 mm and the length of single universal joint is 18 mm. The 95% water-based gel (Skin Moist Burn Pad, Spenco Medical Corporation, Waco, Texas) serves as the MR signal source and is wrapped around the concentric part of the universal joint. A small solenoid coil (3.8 mm OD and 3.5 mm length) with seven turns of 26 AWG copper magnet wire (Belden Inc., Richmond, IN) is overlapped around that water-based gel and a variable non-magnetic capacitor (8PF - 50PF, Johanson Manufacturing Co., Boonton, NJ) is connected to it for tuning of the resonant circuit. For the actuation, wire-driven mechanism is used and three directional wires (0.45 mm diameter fishing lines) are connected through directional holes. A superelastic NiTi wire is connected through a central hole. For MR compatibility, shielded stepper motors are located 2.5 m away, and transmit actuation with fishing lines. This bendable tip can provide around 3.5 N. Ultrasonic or piezoelectric motors can also be employed to actuate the manipulator.

For dual-modality biosensing, the MRS/LIF probe is inserted into the probe hole. This MRS/LIF probe consists of a 1.25mm OD 7-fiber optical sensor used for the LIF and a microcoil used for the MRS. Six fibers are connected to an LED (filtered at 450nm) for high power light emission and one fiber was used for reception of light connected to an optical spectrometer (USB 2000+, Ocean Optics, Dunedin, FL). The MRS/LIF probe is registered to the MR scanner from images collected with the microcoil as a Tx/Rx fiducial marker.

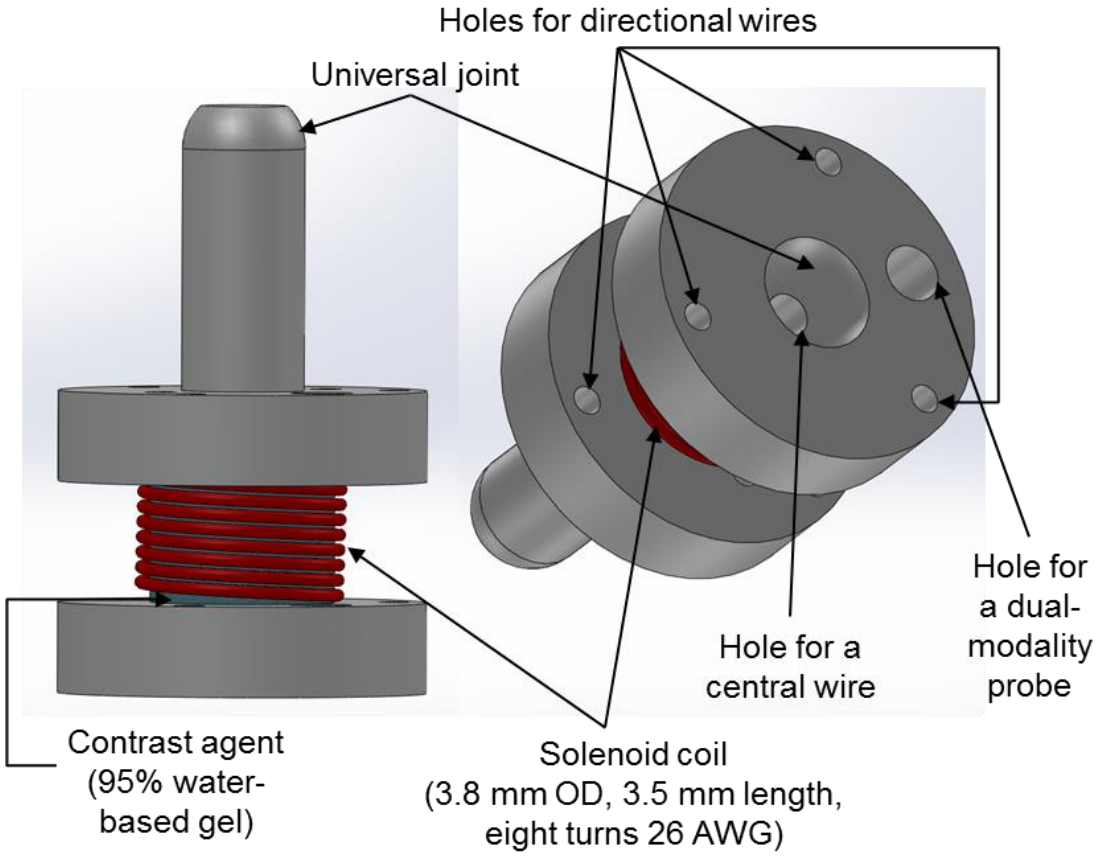

Figure 4.21 Model of a single distal piece of integrated sensors and system for the MRI-guided and robot-assisted interventions.

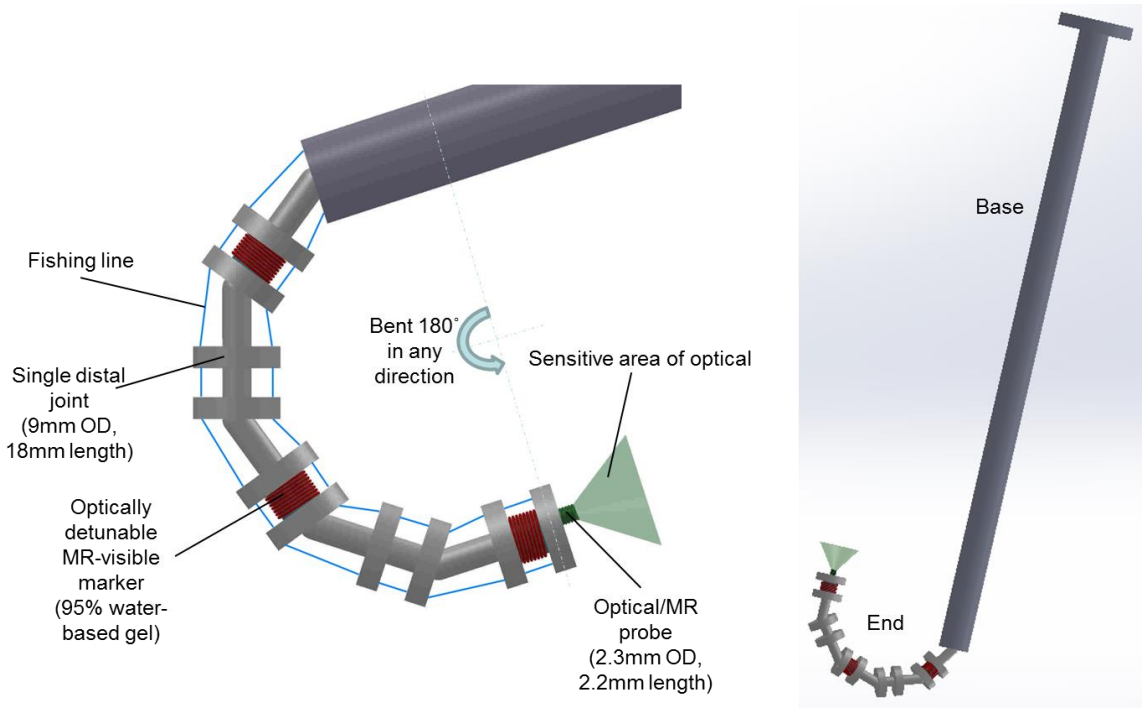

Figure 4.22 3D design of a computer-controlled snake-like dual-modality biosensor.

Chapter 5

5 Conclusion and Future Work

5.1 Conclusion

This dissertation studied challenges and solutions with respect to integration of sensors and manipulators for the MRI-guided and robot-assisted interventions. The details of the developed techniques which are for fast tracking of MR-compatible using optically detunable MR-visible marker, novel segmentation and fast 3D reconstruction of tubular structures from triplanar MR projection images, fully MR-compatible optical encoder, robot-assisted dual-modality biosensor, and system integration were described. The goals and an overview of this study is summarized below.

5.1.1 Optically Detunable MR-visible Marker

Integrated control system of the manipulator control and marker control for fast tracking and accurate localization using the MR-visible marker that can be optically tuned and detuned by the motion of the maneuvering link or joint of the MR-compatible manipulator was developed. This technique not only simplifies MR image post-processing (e.g., automatic marker detection, automatic calculation of marker position, etc.), but also accelerates the MR data acquisition and the unambiguous identification of individual markers for fast tracking and accurate localization of the markers on the articulated MR-compatible manipulator and bendable tools during MRI-guided and robot-assisted surgeries and interventions.

5.1.2 3D Reconstruction of Tubular Structures

An MR acquisition scheme for 3D volumetric imaging of contrast enhanced tubular structures was implemented and a static vessel-mimicking phantom filled with Gd-based T1-shortening contrast agent was developed. Three orthogonal MR projection images were collected along the sagittal, transverse and coronal planes with a simultaneously collecting method - triplanar projection imaging (TPI). A novel method for segmentation of tubular structure from the TPI set was developed and 3D reconstruction of the tubular structure from a TPI set using the match driven backprojections algorithm. The 3D accuracy analysis

of the 3D reconstruction method was investigated by the comparison of the centerlines of the 3D reconstructed tubular structure created from the TPI set and 128 coronal multislice set. This 3D reconstruction technique could be used to visualize contrast enhanced catheters and vessels for MRI-guided interventions.

5.1.3 Sensors and System Integration

The general-purpose MR-compatible optical encoder was designed for the feedback motion control of robotic manipulators. The robot-assisted dual-modality was developed for providing complementary medical information to identify materials with simultaneous MRS and LIF data. The design of the integration system was proposed to integrate optically detunable MR-visible markers for tracking of MR-visible manipulators, the dual MRS/LIF biosensor for monitoring simultaneous metabolic changes and structure of molecules, the MR compatible dexterous manipulator for overcoming limitation of patient accessibility, and the robot and marker control system for controlling an MR-compatible robotic manipulator and monitoring real-time MR images.

5.2 Future Work

In this dissertation, I have designed to integrate sensors and the system for the MRI-guided and robot-assisted interventions. The above mentioned methodology can provide the technique for accurate localization and fast tracking of MR-compatible manipulators using multiple MR-visible markers which can be optically detunable ICRF coils by the motion of the maneuvering portion of the manipulator. Also, this technique can bring the dual imaging modalities (MRS and LIF) technique by integrating an optical biosensor for the LIF and a microcoil used for MRS. In addition, the MR-compatible dexterous manipulator provides higher flexibility and accessibility inside the limited workspace of the patient's body and the magnetic bore of the MRI scanner.

Future work includes extending the studies to phantom, animal and patient data sets with the incorporated sensors and system for the MRI-guided and robot-assisted interventions. The current research can be extended as follows:

- Implementation of the prototype of the MR-compatible dexterous manipulator, a dual MRS/LIF probe, and multiple MR-visible markers.
- MRI compatibility testing for the MR-compatible dexterous manipulator, MR-compatible optical encoder, and intergraded MR-compatible snake-like dual-modality biosensor.
- Pulse sequence optimization for MR imaging using multiple MR-visible markers which can be optically tuned or detuned by the motion of the actuated link or joint of the MR-compatible manipulator.
- Pulse sequence optimization for fast imaging of higher resolution multi-planar MR projection images.
- Robot motion and control analysis of the MR-compatible dexterous manipulator.

- Development of realistic modeling of the MR-compatible dexterous manipulator based on real-time MRI for intervention.

Bibliography

1. Kroh, M. and S. Chalikonda, *Essentials of Robotic Surgery*. 2015: Springer.
2. Culjat, M., R. Singh, and H. Lee, *Medical Devices: Surgical and Image-Guided Technologies*. 2012: John Wiley & Sons.
3. Siciliano, B. and O. Khatib, *Springer handbook of robotics*. 2008: Springer Science & Business Media.
4. Reddick, E.J., et al., *Laparoscopic laser cholecystectomy.* Laser Medicine and Surgery News and Advances, 1989. **7**(1): p. 38-40.
5. Soper, N.J., L.M. Brunt, and K. Kerbl, *Laparoscopic general surgery*. New England Journal of Medicine, 1994. **330**(6): p. 409-419.
6. Mühe, E., *Long-term follow-up after laparoscopic cholecystectomy.* Endoscopy, 1992. **24**(9): p. 754-758.
7. Richardson, W.S. and J.C. Bowen, *Minimally invasive esophageal surgery.* Surgical Clinics of North America, 1998. **78**(5): p. 795-803.
8. Richardson, W.S., et al., *Minimally invasive abdominal surgery.* The Ochsner Journal, 2000. **2**(3): p. 153-157.

9. Duncan III, J.L., et al., *Laparoscopic adrenalectomy is superior to an open approach it treat primary hyperaldosteronism.* The American surgeon, 2000. **66**(10): p. 932.

10. Mencaglia, L., et al., *Manual of gynecological laparoscopic surgery*. 2015: Endo-Press.

11. Wang, C.-C., et al., *Ultrasound-guided minimally invasive surgery for achilles tendon rupture: preliminary results.* Foot & ankle international, 2012. **33**(7): p. 582-590.

12. Cabon, Q., et al., *Evaluation of intraoperative fluorescence imaging–guided surgery in cancer-bearing dogs: a prospective proof-of-concept phase II study in 9 cases.* Translational Research, 2015.

13. Peters, T.M., *Image-guided surgery: from X-rays to virtual reality.* Computer methods in biomechanics and biomedical engineering, 2001. **4**(1): p. 27-57.

14. Thomas, D., R. Anderson, and G. Du Boulay, *CT-guided stereotactic neurosurgery: experience in 24 cases with a new stereotactic system.* Journal of Neurology, Neurosurgery & Psychiatry, 1984. **47**(1): p. 9-16.

15. Heilbrun, M., et al., *Brown-Roberts-Wells stereotactic frame modifications to accomplish magnetic resonance imaging guidance in three planes.* Stereotactic and Functional Neurosurgery, 1987. **50**(1-6): p. 143-152.

16. Leksell, L., D. Leksell, and J. Schwebel, *Stereotaxis and nuclear magnetic resonance.* Journal of Neurology, Neurosurgery & Psychiatry, 1985. **48**(1): p. 14-18.

17. Levivier, M., et al., *Use of stereotactic PET images in dosimetry planning of radiosurgery for brain tumors: clinical experience and proposed classification.* Journal of Nuclear Medicine, 2004. **45**(7): p. 1146-1154.

18. Silverman, S.G., et al., *Interactive MR-guided biopsy in an open-configuration MR imaging system.* Radiology, 1995. **197**(1): p. 175-81.

19. Masamune, K., et al., *Development of an MRI-compatible needle insertion manipulator for stereotactic neurosurgery.* J Image Guid Surg, 1995. **1**(4): p. 242-8.

20. Klotz, H.P., et al., *Experimental cryosurgery of the liver under magnetic resonance guidance.* Comput Aided Surg, 1997. **2**(6): p. 340-5.

21. D'Amico, A., et al., *Real-time magnetic resonance image-guided interstitial brachytherapy in the treatment of select patients with clinically localized prostate cancer.* International Journal of Radiation Oncology* Biology* Physics, 1998. **42**(3): p. 507-515.

22. Lu, D., S.G. Silverman, and S.S. Raman, *MR-guided therapy. Applications in the abdomen.* Magnetic resonance imaging clinics of North America, 1999. **7**(2): p. 337-348.

23. Skjeldal, S., et al., *Real time MRI-guided excision and cryo-treatment of osteoid osteoma in os ischii--a case report.* Acta Orthopaedica Scandinavica, 2000. **71**(6): p. 637-638.

24. Hirose, M., et al., *Feasibility of MR imaging-guided breast lumpectomy for malignant tumors in a 0.5-T open-configuration MR imaging system.* Acad Radiol, 2002. **9**(8): p. 933-41.

25. Mortele, K.J., et al., *MRI-guided abdominal intervention.* Abdom Imaging, 2003. **28**(6): p. 756-74.

26. Tuncali, K., et al., *Evaluation of patients referred for percutaneous ablation of renal tumors: importance of a preprocedural diagnosis.* AJR Am J Roentgenol, 2004. **183**(3): p. 575-82.

27. McVeigh, E.R., et al., *Real-time interactive MRI-guided cardiac surgery: aortic valve replacement using a direct apical approach.* Magn Reson Med, 2006. **56**(5): p. 958-64.

28. Yang, X. and E. Atalar, *MRI-guided gene therapy.* FEBS Lett, 2006. **580**(12): p. 2958-61.

29. Ozturk, C., et al., *Magnetic resonance imaging-guided vascular interventions.* Top Magn Reson Imaging, 2005. **16**(5): p. 369-81.

30. Eby, P.R. and C. Lehman, *MRI-guided breast interventions.* Semin Ultrasound CT MR, 2006. **27**(4): p. 339-50.

31. Bhole, S. and E. Neuschler, *MRI-guided breast interventions.* APPLIED RADIOLOGY, 2015. **7**: p. 7.

32. Tsekos, N.V., E. Christoforou, and A. Özcan, *A general-purpose MR-compatible robotic system.* Engineering in Medicine and Biology Magazine, IEEE, 2008. **27**(3): p. 51-58.

33. Krieger, A., et al., *Design of a novel MRI compatible manipulator for image guided prostate interventions.* Biomedical Engineering, IEEE Transactions on, 2005. **52**(2): p. 306-313.

34. Kwoh, Y.S., et al., *A robot with improved absolute positioning accuracy for CT guided stereotactic brain surgery.* IEEE Trans Biomed Eng, 1988. **35**(2): p. 153-60.

35. Tewari, A., et al., *Technique of da Vinci robot-assisted anatomic radical prostatectomy.* Urology, 2002. **60**(4): p. 569-72.

36. Kunisaki, C., et al., *Video-assisted thoracoscopic esophagectomy with a voice-controlled robot: the AESOP system.* Surg Laparosc Endosc Percutan Tech, 2004. **14**(6): p. 323-7.

37. Allaf, M., et al., *Laparoscopic visual field.* Surgical endoscopy, 1998. **12**(12): p. 1415-1418.

38. Anvari, M., *Telesurgery: remote knowledge translation in clinical surgery.* World J Surg, 2007. **31**(8): p. 1545-50.

39. Faust, R.A., et al., *Robotic endoscopic surgery in a porcine model of the infant neck.* Journal of Robotic Surgery, 2007. **1**(1): p. 75-83.

40. Pransky, J., *ROBODOC-surgical robot success story.* Industrial Robot: An International Journal, 1997. **24**(3): p. 231-233.

41. Ghodoussi, M., *Transforming a surgical robot for human telesurgery.* Robotics and Automation, IEEE Transactions on, 2003. **19**(5): p. 818-824.

42. Bauer, J., et al., *Remote percutaneous renal access using a new automated telesurgical robotic system.* Telemedicine Journal and E-Health, 2001. **7**(4): p. 341-346.

43. Grueneis, C., R. Richter, and F. Henning, *Clinical introduction of the CASPAR system: problems and initial results.* Comput Aided Surg, 1999. **4**: p. 160.

44. Jakopec, M., et al., *The hands-on orthopaedic robot" Acrobot": Early clinical trials of total knee replacement surgery.* Robotics and Automation, IEEE Transactions on, 2003. **19**(5): p. 902-911.

45. Burger, C., et al., *Development of robots for rehabilitation therapy: The Palo Alto VA/Stanford experience.* Journal of Rehabilitation Research and Development, 2000. **37**(6): p. 663-673.

46. Standard, A., *F2503. Standard practice for marking medical devices and other items for safety in the magnetic resonance environment.* ASTM International, West Conshohocken, PA, 2013.

47. Holton, A., et al., *Comparative MRI Compatibility of 316L Stainless Steel Alloy and Nickel–Titanium Alloy Stents: Original article Technical.* Journal of Cardiovascular Magnetic Resonance, 2002. **4**(4): p. 423-430.

48. Knott, P.T., et al., *A comparison of magnetic and radiographic imaging artifact after using three types of metal rods: stainless steel, titanium, and vitallium.* The Spine Journal, 2010. **10**(9): p. 789-794.

49. Kangarlu, A. and F.G. Shellock, *Aneurysm clips: evaluation of magnetic field interactions with an 8.0 T MR system.* Journal of Magnetic Resonance Imaging, 2000. **12**(1): p. 107-111.

50. Ahn, C.B. and Z.H. Cho, *Analysis of the eddy-current induced artifacts and the temporal compensation in nuclear magnetic resonance imaging.* IEEE Trans Med Imaging, 1991. **10**(1): p. 47-52.

51. Trakic, A., et al., *Longitudinal gradient coil optimization in the presence of transient eddy currents.* Magn Reson Med, 2007. **57**(6): p. 1119-30.

52. Spees, W.M., et al., *Quantification and compensation of eddy-current-induced magnetic-field gradients.* J Magn Reson, 2011. **212**(1): p. 116-23.

53. Gassert, R., et al., *MRI/fMRI-compatible robotic system with force feedback for interaction with human motion.* IEEE ASME TRANSACTIONS ON MECHATRONICS, 2006. **11**(2): p. 216.

54. Jezzard, P., A.S. Barnett, and C. Pierpaoli, *Characterization of and correction for eddy current artifacts in echo planar diffusion imaging.* Magn Reson Med, 1998. **39**(5): p. 801-12.

55. Chan, R.W., et al., *Characterization and correction of eddy-current artifacts in unipolar and bipolar diffusion sequences using magnetic field monitoring.* J Magn Reson, 2014. **244**: p. 74-84.

56. An, J., et al., *Tracking of MR compatible interventional robots by controlling the MRI visibility of optically detunable MR markers.* Physica Medica: European Journal of Medical Physics, 2014. **30**: p. e51.

57. An, J., et al. *Localization and tracking with RF coils that are optically detuned by the control of an MR compatible manipulator*. in *Joint Annual Meeting ISMRM-ESMRMB, Milan, Italy*. 2014.

58. An, J., et al. *Tracking of a Robotic Device by Controlling the Visibility of Markers from the Robot Control*. in *24th Annual Meeting of ISMRM, Singapore*. 2016.

59. An, J., et al. *Tracking of MRI Interventional Devices with Computer-Controlled Detunable Markers*. in *Mediterranean Conference on Medical and Biological Engineering and Computing, Paphos, Cyprus*. 2016. Springer.

60. Tsekos, N.V., A. Özcan, and E. Christoforou, *A prototype manipulator for magnetic resonance-guided interventions inside standard cylindrical magnetic resonance imaging scanners.* Journal of biomechanical engineering, 2005. **127**(6): p. 972-980.

61. Tsekos, N.V., et al., *Magnetic resonance-compatible robotic and mechatronics systems for image-guided interventions and rehabilitation: a review study.* Annu. Rev. Biomed. Eng., 2007. **9**: p. 351-387.

62. Duerk, J.L., E.Y. Wong, and J.S. Lewin, *A brief review of hardware for catheter tracking in magnetic resonance imaging.* MAGMA, 2002. **13**(3): p. 199-208.

63. Kos, S., et al., *MR-guided endovascular interventions: a comprehensive review on techniques and applications.* Eur Radiol, 2008. **18**(4): p. 645-57.

64. Henk, C.B., C.B. Higgins, and M. Saeed, *Endovascular interventional MRI.* J Magn Reson Imaging, 2005. **22**(4): p. 451-60.

65. Bock, M. and F.K. Wacker, *MR-guided intravascular interventions: techniques and applications.* J Magn Reson Imaging, 2008. **27**(2): p. 326-38.

66. Ratnayaka, K., et al., *Interventional cardiovascular magnetic resonance: still tantalizing.* J Cardiovasc Magn Reson, 2008. **10**: p. 62.

67. Wong, M., et al., *An optical system for wireless detuning of parallel resonant circuits.* Journal of Magnetic Resonance Imaging, 2000. **12**(4): p. 632-638.

68. Eggers, H., et al., *Image-based tracking of optically detunable parallel resonant circuits.* Magnetic resonance in medicine, 2003. **49**(6): p. 1163-1174.

69. Koechli, V., et al., *Vascular interventions guided by ultrafast MR imaging: evaluation of different materials.* Magnetic resonance in medicine, 1994. **31**(3): p. 309-314.

70. DiMaio, S.P., et al., *Dynamic MRI scan plane control for passive tracking of instruments and devices*, in *Medical Image Computing and Computer-Assisted Intervention–MICCAI 2007*. 2007, Springer. p. 50-58.

71. Glowinski, A., et al., *Catheter visualization using locally induced, actively controlled field inhomogeneities.* Magnetic resonance in medicine, 1997. **38**(2): p. 253-258.

72. Dumoulin, C., S. Souza, and R. Darrow, *Real-time position monitoring of invasive devices using magnetic resonance.* Magnetic Resonance in Medicine, 1993. **29**(3): p. 411-415.

73. Atalar, E., et al., *High resolution intravascular MRI and MRS by using a catheter receiver coil.* Magnetic resonance in medicine, 1996. **36**(4): p. 596-605.

74. Ladd, M.E., et al., *Active MR visualization of a vascular guidewire in vivo.* Journal of magnetic resonance imaging, 1998. **8**(1): p. 220-225.

75. Zhang, Q., et al., *A multielement RF coil for MRI guidance of interventional devices.* Journal of Magnetic Resonance Imaging, 2001. **14**(1): p. 56-62.

76. Quick, H.H., et al., *Interventional magnetic resonance angiography with no strings attached: wireless active catheter visualization.* Magnetic resonance in medicine, 2005. **53**(2): p. 446-455.

77. Burl, M., G.A. Coutts, and I.R. Young, *Tuned fiducial markers to identify body locations with minimal perturbation of tissue magnetization.* Magnetic resonance in medicine, 1996. **36**(3): p. 491-493.

78. Wacker, F.K., et al., *The catheter-driven MRI scanner: a new approach to intravascular catheter tracking and imaging-parameter adjustment for interventional MRI.* American Journal of Roentgenology, 2004. **183**(2): p. 391-395.

79. Garnov, N., et al., *Suitability of miniature inductively coupled RF coils as MR-visible markers for clinical purposes.* Medical physics, 2011. **38**(11): p. 6327-6335.

80. Christoforou, E.G., N.V. Tsekos, and A. Özcan, *Design and testing of a robotic system for MR image-guided interventions.* Journal of Intelligent and Robotic Systems, 2006. **47**(2): p. 175-196.

81. von Sternberg, N.C., et al. *A new method for MR compatible actuation: Solid Media Flexible Transmission*. in *Joint Annual Meeting of ISMRM-ESMRMB, Milan, Italy*. 2014.

82. Liu, X., et al. *A New Transmission Mechanism for the Actuation of Manipulators for Magnetic Resonance Imaging (MRI) Guided Interventions*. in *Mediterranean Conference on Medical and Biological Engineering and Computing, Paphos, Cyprus*. 2016. Springer.

83. An, J., et al. *3D Reconstruction of Tubular Structures from Three Orthogonal MRI Projections*. in *Mediterranean Conference on Medical and Biological Engineering and Computing, Paphos, Cyprus*. 2016. Springer.

84. Baert, S.A., et al., *Three-dimensional guide-wire reconstruction from biplane image sequences for integrated display in 3-D vasculature*. Medical Imaging, IEEE Transactions on, 2003. **22**(10): p. 1252-1258.

85. Bender, H.-J., et al. *Reconstruction of 3D catheter paths from 2D X-ray projections*. in *Medical Image Computing and Computer-Assisted Intervention–MICCAI'99*. 1999. Springer.

86. Laurentini, A., *The visual hull concept for silhouette-based image understanding.* Pattern Analysis and Machine Intelligence, IEEE Transactions on, 1994. **16**(2): p. 150-162.

87. Solaiyappan, M., J. Lee, and E. Atalar. *Depth reconstruction from projection images for 3D visualization of intravascular MRI probes*. in *Proceedings of the 7th Annual Meeting of ISMRM, Philadelphia, PA, USA*. 1999.

88. Sathyanarayana, S., et al., *Tracking planar orientations of active MRI needles.* Journal of Magnetic Resonance Imaging, 2007. **26**(2): p. 386-391.

89. George, A.K., et al., *Visualization of active devices and automatic slice repositioning ("SnapTo") for MRI-guided interventions.* Magnetic resonance in medicine, 2010. **63**(4): p. 1070-1079.

90. Schirra, C.O., et al., *Accelerated 3D catheter visualization from triplanar MR projection images.* Magnetic Resonance in Medicine, 2010. **64**(1): p. 167-176.

91. Ristroph, L., et al., *Automated hull reconstruction motion tracking (HRMT) applied to sideways maneuvers of free-flying insects.* Journal of Experimental Biology, 2009. **212**(9): p. 1324-1335.

92. Polesel, A., G. Ramponi, and V.J. Mathews, *Image enhancement via adaptive unsharp masking.* IEEE transactions on image processing, 2000. **9**(3): p. 505-510.

93. Chaudhuri, S., et al., *Detection of blood vessels in retinal images using two-dimensional matched filters.* Medical Imaging, IEEE Transactions on, 1989. **8**(3): p. 263-269.

94. Pratt, W.K., *Digital image processing.* 1978.

95. Mukherjee, S. and S.T. Acton, *Region based segmentation in presence of intensity inhomogeneity using legendre polynomials.* Signal Processing Letters, IEEE, 2015. **22**(3): p. 298-302.

96. Lorensen, W.E. and H.E. Cline. *Marching cubes: A high resolution 3D surface construction algorithm*. in *ACM siggraph computer graphics*. 1987. ACM.

97. Huang, H., et al., *L1-medial skeleton of point cloud.* ACM Trans. Graph., 2013. **32**(4): p. 65:1-65:8.

98. De Boor, C., et al., *A practical guide to splines*. Vol. 27. 1978: Springer-Verlag New York.

99. Lee, E.T., *Choosing nodes in parametric curve interpolation.* Computer-Aided Design, 1989. **21**(6): p. 363-370.

100. Christoforou, E., et al., *Performance of interventions with manipulator-driven real-time MR guidance: implementation and initial in vitro tests.* Magnetic resonance imaging, 2007. **25**(1): p. 69-77.

101. Yamashita, Y., et al., *In vitro and clinical studies of image acquisition in breath-hold MR cholangiopancreatography: single-shot projection technique versus*

multislice technique. AJR. American journal of roentgenology, 1997. **168**(6): p. 1449-1454.

102. Atalar, E., et al., *Catheter-tracking FOV MR fluoroscopy.* Magnetic resonance in medicine, 1998. **40**(6): p. 865-872.

103. Moore, M., *Symmetrical intersections of right circular cylinders.* The Mathematical Gazette, 1974. **58**(405): p. 181-185.

104. Weisstein, E.W., *Steinmetz Solid.* 2005.

105. DiMaio, S., et al. *A system for MRI-guided prostate interventions*. in *Biomedical Robotics and Biomechatronics, 2006. BioRob 2006. The First IEEE/RAS-EMBS International Conference on*. 2006. IEEE.

106. Fischer, G.S., et al., *Robotic assistant for transperineal prostate interventions in 3T closed MRI,* in *Medical Image Computing and Computer-Assisted Intervention–MICCAI 2007*. 2007, Springer. p. 425-433.

107. Krasnow, B., *Fiberoptic joystick with quadrature encoders and arduino.* 2010.

108. Klinke, T., et al., *Artifacts in magnetic resonance imaging and computed tomography caused by dental materials.* PLoS One, 2012. **7**(2): p. e31766.

109. Shellock, F.G. and V.J. Shellock, *Ceramic surgical instruments: ex vivo evaluation of compatibility with MR imaging at 1.5 T.* Journal of Magnetic Resonance Imaging, 1996. **6**(6): p. 954-956.

110. Wallner, A.S. and W.M. Ritchey, *Void distribution and susceptibility differences in ceramic materials using MRI.* Journal of materials research, 1993. **8**(03): p. 655-661.

111. Kotze, D. and C. De Vries, *A quick guide to safety and compatibility of passive implants and devices in an MR environment.* SA Journal of Radiology, 2004. **8**(2).

112. Duttenhoefer, F., et al., *Magnetic resonance imaging in zirconia-based dental implantology*. Clinical oral implants research, 2015. **26**(10): p. 1195-1202.

113. Raphael, B., et al., *MRI comparison of periprosthetic structures around zirconium knee prostheses and cobalt chrome prostheses.* American Journal of Roentgenology, 2006. **186**(6): p. 1771-1777.

114. Sonmez, A.E., et al., *A system for endoscopic mechanically scanned localized proton MR and light-induced fluorescence emission spectroscopies.* Journal of Magnetic Resonance, 2012. **222**: p. 16-25.

115. An, J., et al., *MR compatible endoscope for assessing the spatial distribution of co-registered optical and 1H signals.* Physica Medica: European Journal of Medical Physics, 2014. **30**: p. e39.

116. An, J., et al. *Manipulator-mounted optical NMR dual-modality probe for multimodality scanning in MR guided and robot-assisted interventions*. in *Joint Annual Meeting of ISMRM-ESMRMB, Milan, Italy*. 2014.

117. Zhu, C., et al., *Fluorescence spectroscopy: an adjunct diagnostic tool to image-guided core needle biopsy of the breast.* Biomedical Engineering, IEEE Transactions on, 2009. **56**(10): p. 2518-2528.

118. Sung, K.-B., et al., *Fiber-optic confocal reflectance microscope with miniature objective for in vivo imaging of human tissues.* Biomedical Engineering, IEEE Transactions on, 2002. **49**(10): p. 1168-1172.

119. Dario, P., et al., *A novel mechatronic tool for computer-assisted arthroscopy.* Information Technology in Biomedicine, IEEE Transactions on, 2000. **4**(1): p. 15-29.

120. Faraz, A. and S. Payandeh, *Synthesis and workspace study of endoscopic extenders with flexible stem.* Journal of mechanical design, 1997. **119**(3): p. 412-414.

121. Faraz, A. and S. Payandeh, *Towards approximate models of Coulomb frictional moments in:(I) revolute pin joints and (II) spherical-socket ball joints.* Journal of engineering mathematics, 2001. **40**(3): p. 283-296.

122. Simaan, N., R. Taylor, and P. Flint. *A dexterous system for laryngeal surgery*. in *Robotics and Automation, 2004. Proceedings. ICRA'04. 2004 IEEE International Conference on*. 2004. IEEE.

123. Peirs, J., et al. *A flexible distal tip with two degrees of freedom for enhanced dexterity in endoscopic robot surgery*. in *Proceedings of the 13th micromechanics europe workshop*. 2002.

124. Degani, A., et al. *Highly articulated robotic probe for minimally invasive surgery*. in *Robotics and Automation, 2006. ICRA 2006. Proceedings 2006 IEEE International Conference on*. 2006. IEEE.

125. Ota, T., et al., *Epicardial atrial ablation using a novel articulated robotic medical probe via a percutaneous subxiphoid approach.* Innovations (Philadelphia, Pa.), 2006. **1**(6): p. 335.

126. Ota, T., et al., *A highly articulated robotic surgical system for minimally invasive surgery.* The Annals of thoracic surgery, 2009. **87**(4): p. 1253-1256.

127. Harada, K., et al. *Micro manipulators for intrauterine fetal surgery in an open MRI*. in *Robotics and Automation, 2005. ICRA 2005. Proceedings of the 2005 IEEE International Conference on*. 2005. IEEE.

128. Haraguchi, D., K. Tadano, and K. Kawashima. *A prototype of pneumatically-driven forceps manipulator with force sensing capability using a simple flexible joint*. in *Intelligent Robots and Systems (IROS), 2011 IEEE/RSJ International Conference on*. 2011. IEEE.

129. Seow, C.M., et al., *Articulated manipulator with multiple instruments for natural orifice transluminal endoscopic surgery.* Journal of Medical Devices, 2013. **7**(4): p. 041004.

130. Breedveld, P., J. Sheltes, and E.M. Blom, *A new, easily miniaturized steerable endoscope.* Engineering in Medicine and Biology Magazine, IEEE, 2005. **24**(6): p. 40-47.